Integrated actuation and harvesting system for a bio-inspired underwater robot

Can piezoelectrics be used to both charge and actuate a soft underwater robot?

Isabel van Noesel

Integrated actuation and harvesting system for a bio-inspired underwater robot

Can piezoelectrics be used to both charge and actuate a soft underwater robot?

by

Isabel van Noesel

Supervisor (TUD):	Prof. Dr. Ir. G. D. Weymouth
Supervisor (TUD):	Dr. Ir. J. Jovanova
Supervisor (UU):	Prof. Dr. Ir. K. Philippart
Supervisor (UU):	Prof. Dr. T. Bouma
Project Duration:	October, 2024 - Novemeber, 2025
Faculty:	Mechanical Engineering (TUD) and Earth Sciences (UU)

Thesis for the degree of MSc in Marine Technology in the specialization of *Ship Design and Ship Hydromechanics*

Integrated actuation and harvesting system for a bio-inspired underwater robot

By

Isabel van Noesel

Performed at

-

This thesis (**MT.25/26.014.M**) is classified as confidential in accordance with the general conditions for projects performed by the TUDelft.

28/11/2025

Company supervisors
Responsible supervisor:-
E-mail:-
Daily Supervisor(s): -
E-mail: -

Thesis exam committee
Chair/Responsible Professor: G. Weymouth
Staff Member: J. Jovanova
Staff Member: V. Kortman
Staff Member: P. Pahlavan

Author Details
Studynumber:4711432

Aknowledgements

Completing this research project could not have been done without the help of others. I have been guided, mentored and supported by many people making this a very educative process. Therefore I want to express sincere gratitude.

First of all, I want to thank my supervisors. Prof. Weymouth and Dr. Jovanova, who have guided me through every part of the thesis. Prof. Philippart and Prof. Bouma, for making this integrated project possible and helping me graduate with 2 degrees.

For circuit development and electrical advice, the time and commitment from Jacques Brenkman have been indispensable. Without his dedication to the project, none of the essential measurements would have been performed.

For piezoelectric advice, I want to deeply thank Paul Keijzer and Bradley But. Their in-depth knowledge of not only theory but also practical applications has been very insightful. Together with Jacques Brenkman they have introduced me to the world of electrical engineering.

I want to express gratitude to all the people who have helped me at the testing facilities. Wim Wien, who has kindly supported me at the wind lab, and Sebastian Scheier, who has extensively guided me in developing a testing setup and plan. Especially during the critical assessment of the energy harvesting tests, Sebastian Schreier has contributed largely to the data documentation. An unmissable aspect of the testing phase.

During the flume tank tests, Sedat Tokgöz has supported the entire underwater testing phase. His time and dedication have greatly improved the testing process and reliability of the results.

I want to thank Vittorio Garofano for assisting me in the lab and making me feel at home in this new space of the faculty.

Also, I want to thank Vera and Aaron for their design inspiration and advice. As well as their critical questions and feedback.

Lastly, I want to thank my parents for supporting me in obtaining the necessary piezoelectric materials so I could continue my research journey.

Summary

This report describes a design research project for a bio-inspired soft underwater robot that can both propel itself and harvest energy. The design is inspired by the remora suckerfish, which attaches itself to other species and hitchhikes to conserve energy. The underwater robot design is able to propel itself and harvest current energy when stationary and attached to an object. The design process aims to address operational efficiency for both energy harvesting and propulsion. To reduce operational maintenance and approach fish like swimming, a simple dual system is designed using piezoelectric materials.

A literature review is performed to determine the most important efficiency parameters for both modes (propulsion and harvesting) and the most suitable simple system.

The design process follows the double diamond, which is a design process from the Delft method. The design process includes literature, goal-oriented prototyping, testing and evaluating. The design process was iterative, based on an existing design.

The existing design originates from a propulsion optimised model, which can fully be reproduced. This design has been altered in terms of stiffness in the flexible part of the underwater robot and the actuation and harvesting system. The original electromotor has been replaced by a piezoelectric system for propulsion and harvesting.

The harvesting capabilities have been tested and quantitatively measured. Multiple tests have been performed to determine the underwater robots' characteristics. The harvesting capabilities have been tested and quantitatively measured. The actuation performance has been determined based on predictive calculations.

The harvesting results are similar to a previous design which uses piezoelectric materials to actuate and harvest energy from the same system. However, the current output of piezoelectric materials in general is very low, making it challenging to use the harvested energy to be stored in a battery. Additionally, piezoelectric materials require high voltage sources, making the system complex and unsuitable for series connections.

The results of this design research show the challenges of using piezoelectrics for both actuation and energy harvesting. Many improvements need to be made, both mechanically and electronically, for such a design to be feasible.

Contents

1

Introduction

1.1. Underwater monitoring

The global windfarm industry, and specifically in the North Sea, depicted in figure 1.1, will expand in the coming years. With this expansion comes an increasing demand for underwater monitoring systems for construction and ecological monitoring.

Developing effective and practical monitoring approaches is essential not only for ensuring operational safety and optimising energy production but also for mitigating ecological impacts. Given their critical role in the shift toward renewable energy, understanding the environmental implications of OWFs is vital to ensure that their benefits are not offset by unintended ecological consequences[1, 2].

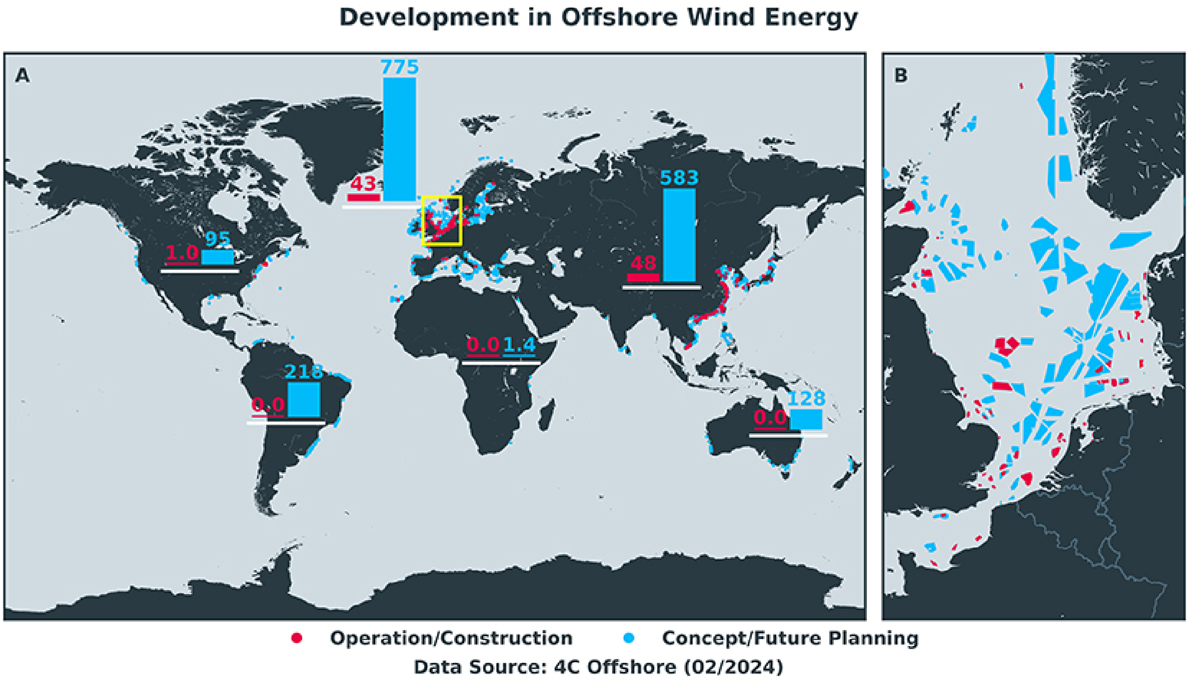

Figure 1.1: Map of offshore wind farm development in gigawatts [3]

Monitoring ecological change has become increasingly important as human activities exert widespread and long-term effects on natural systems [4]. Ecology has developed from an observational discipline into a predictive and data-driven science shaped by the accelerating impacts of global change and biodiversity loss. Modern ecology, therefore, relies on comprehensive datasets to document biodiversity, analyse ecosystem responses, and predict future dynamics under anthropogenic influence [1, 5].

Figure 1.2 describes the potential ecological influences that OWFs may have on the local ecosystem. However, such effects remain largely unknown for most installation sites. A study by S. Watson et al. [1] established that more than 86% of the effects of OWF on the ecosystem remain unknown.

A general overview of the potential effects from figure 1.2 include noise and sediment/bottom disturbance during the construction and operation phase of the wind farm. Including the presence of an electromagnetic field from underwater cables during the operation phase. Due to monopile foundations, sediment movement decreases, and during the operation phase, flow turbulence and nutrient circulation increase. Governmental safety regulations prohibit fishing activities in and around wind farm areas. Ocean currents are suppressed with unclear stratification consequences. The extent and direction of these potential ecological cascade effects remain largely unclear, highlighting the need for continued monitoring and research [3].

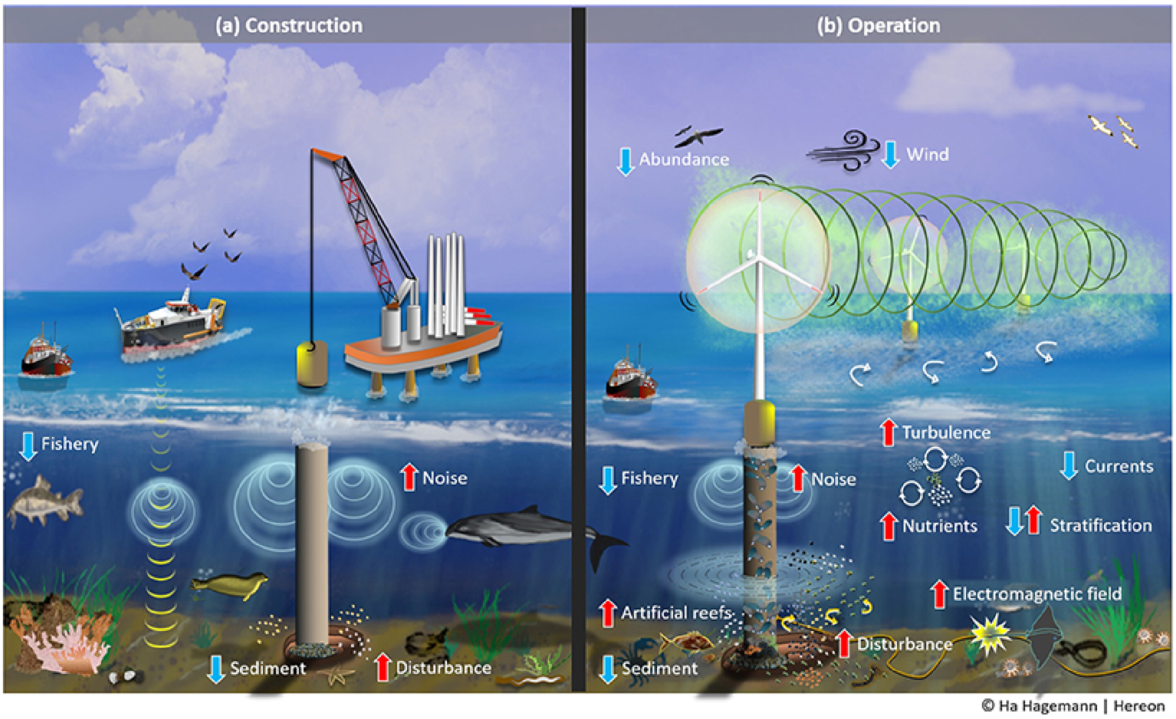

Figure 1.2: Potential environmental offshore wind farm impacts with (red arrow) increasing and (blue arrow) decreasing effects [3]

Marine ecology and ocean dynamics are closely interconnected, and shifts within ecological communities often serve as early indicators of broader oceanographic changes [4]. A recent example in the North Sea is the accidental discovery of a fish species typically found in the Mediterranean Sea (figure 1.3, October 2025). Ruben Vermeule, who encountered this specimen, has a personal mission to document the fish of the North Sea. According to RAVON, the Dutch nature conservation organisation, this unexpected observation is considered indicative of an ecological shift. RAVON suggests that this shift is driven not only by rising sea temperatures but also by the increasing number of wind farms and artificial reefs in the North Sea, which provide additional hard substrates and thus suitable habitats for such species [6].

Figure 1.3: Ringneck blenny (Ringnek slijmvis) in the North Sea captured by Ruben Vermeule [6]

To develop a comprehensive understanding of marine ecosystems, it is essential to distinguish between short-term and long-term datasets, as the relevant temporal scales depend strongly on the processes being studied. The primary purpose of long-term ecological monitoring is to detect gradual biological changes over time [7]. Short-term measurements can be misleading when extrapolated to long-term trends, as they may not capture the underlying variability or cumulative effects driving ecosystem change [4]. Therefore, long-term and continuous underwater monitoring plays a crucial role in understanding the cumulative effects of human activity and climate change on marine systems.

Underwater monitoring methods for structural integrity are underdeveloped [8]. Due to high operating costs and safety considerations, applications for underwater damage detection in OWFs are minimal. Yet structural monitoring is essential to detect early damage and prevent large-scale maintenance.

So, underwater monitoring plays a crucial role in linking ecological understanding with the sustainable development of offshore infrastructure. Reliable, long-term observations are essential to assess ecosystem health, detect subtle environmental changes, and guide informed management decisions. As offshore wind farms continue to expand, the demand for effective, non-invasive, and continuous underwater monitoring will become increasingly urgent. Advancing such monitoring capabilities is therefore essential to ensure that the growth of renewable energy infrastructure aligns with sustainable marine ecosystem management. Strengthening underwater monitoring capacity will therefore be key to achieving both environmental protection and energy sustainability.

1.2. Current underwater monitoring challenges

To understand why there is a lack in long-term underwater monitoring data, the shortcomings of current underwater monitoring systems are analysed. The complex and dynamic behaviour of the oceans under anthropogenic influence can be modelled to improve future climate predictions and to support the development of sustainable management strategies [4]. However, the reliability of such models is inherently dependent on the quality and quantity of available data. With approximately 70% of the Earth's surface covered by ocean, obtaining high-quality, long-term data remains a significant challenge. Limitations in accessibility and monitoring duration have led to a reliance on satellite-based data as the primary source for large-scale measurements, such as sea level and temperature changes [9].

The newest method for underwater monitoring, which does not involve human divers or large research vessels, is remotely operated vehicles (ROVs) and autonomous underwater vehicles (AUVs). Such underwater vehicles are currently a cheaper alternative [5, 10, 11]. An ROV is a tethered underwater robot. There are many different types and sizes depending on the type of monitoring needed to be performed. The operation time and space are dependent on the availability and access of a ship within the distance of the cable. AUVs do not require being connected to a ship, meaning that the operational time is dependent on the battery life. An example of such vehicles is given for both types in figure 1.4.

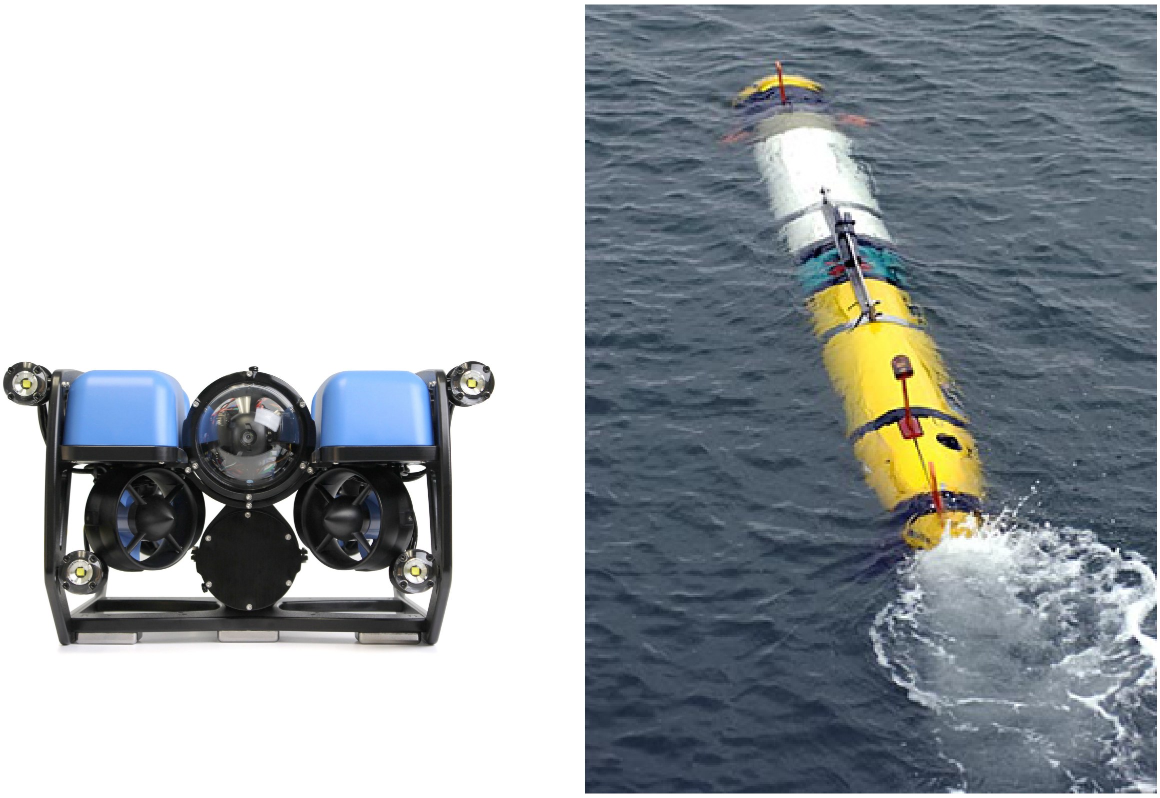

(a) Blue ROV2 [12]

(b) Remus 600 AUV [13]

Figure 1.4: Examples of existing underwater robots: (a) the BlueROV2 and (b) the Remus 600 AUV.

The ROV in figure 1.4a is a small underwater vehicle. The prices of such ROVs depend mostly on the monitoring equipment. Operational and labour costs, including vessel support and deployment, typically dominate the total expense. [12]. Such costs can reach tens of thousands of euros per day, depending on the mission complexity. [14].

The AUV from figure 1.4b is one of the most advanced AUVs, can operate for about 70 hours and may cost hundreds of thousands to a million euros. [13]. Smaller, less advanced AUVs may cost ten times less, but will also have an operational time of ten times less [15].

AUVs are increasingly in demand due to the growing number of offshore wind farms (OWFs) [16]. Compared to remotely operated vehicles (ROVs), AUVs are attractive because they are less labour-intensive and more cost-effective. However, AUVs remain limited by short operational durations, constrained launch and retrieval windows, and the logistical complexity of deployment from ships [16, 17, 18]. On-site charging or docking stations have been proposed to extend mission endurance, yet these systems are still in the early stages of development [17, 18].

Concepts such as those shown in Figure 1.5 highlight the current limitations in the operational efficiency of underwater vehicles, illustrating that current designs are both costly and operationally constrained. These futuristic charging and docking concepts aim to extend mission duration and reduce the need for human intervention in deployment and retrieval. Such developments emphasize the growing need for autonomous, energy-efficient solutions in long-term ocean monitoring.

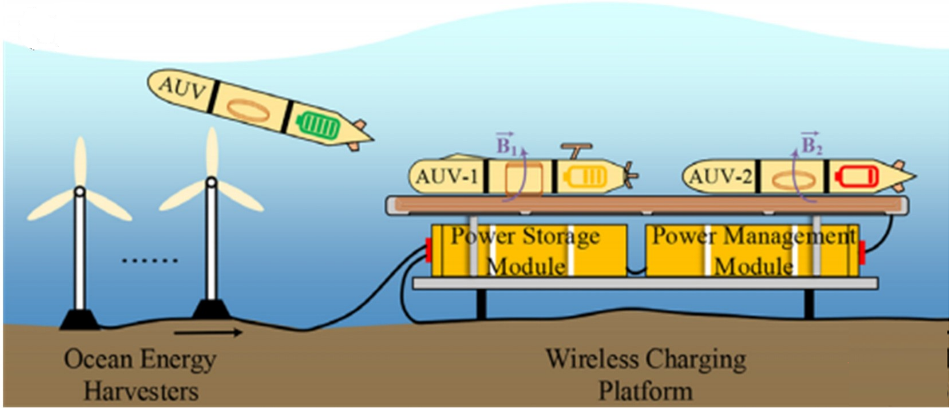

Figure 1.5: Charging station concept by F. Lyu et al. [19]

As depicted in Figure 1.5, ocean currents can serve as a potential energy source. These currents can be harnessed by transducing current-induced motion into electrical energy. The North Sea, characterized by its large tidal range, represents a reliable source of ocean currents. In this shallow sea, current velocities typically range between 0.1 and 1 m/s, depending on the season and tidal phase. The most recent surface current measurements from Windpark Noord, located off the Dutch coast, are presented in Figure 1.6 [20].

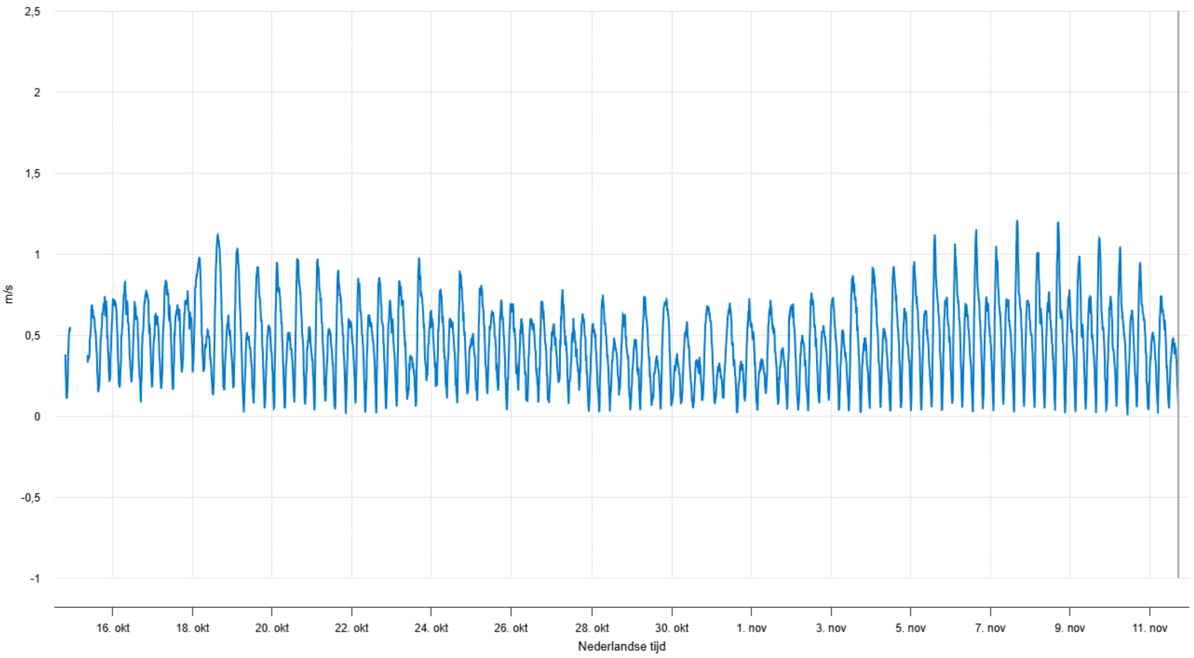

Figure 1.6: Watercurrent speed data taken from offshore windfarm 'Windpark Noord' (October and November 2025) [20]

Harvesting ocean energy during underwater monitoring operations can substantially extend the operational lifetime of autonomous systems. Although the North Sea provides a consistent current resource, current velocities are seldom exceptionally high, and peak conditions are of short duration. These characteristics are suboptimal for conventional turbine-based ocean energy harvesters. Alternative concepts, such as flapping foil systems, have shown comparable energy generation to turbines while performing more efficiently in low-current and shallow-water conditions [21, 22].

In summary, current underwater vehicles face multiple interlinked challenges: high operational and labour costs, limited endurance, complex launch and retrieval logistics, and potential disturbance of sensitive marine habitats. These limitations restrict their practical deployment for ecological monitoring, often resulting in short-term or infrequent data collection. To make underwater monitoring more feasible and widely implementable, advances in vehicle efficiency, energy management, and ocean energy harvesters are urgently needed.

1.3. Bio-inspired design potential

Regardless of their specific application, most underwater robots are pelagic, meaning they navigate primarily within the water column using thrusters. Propeller efficiency has been extensively studied in the last century, yet its efficiency has only been improved to approximately 60% [23, 24]. Additionally, this design imposes inherent limitations on their ability to interact directly with the environment. A common strategy involves hovering at a fixed position while simultaneously executing station-keeping and manipulation tasks. Although effective, this approach is computationally intensive and highly sensitive to environmental disturbances, such as currents, and is subject to numerous modelling and identification uncertainties. To simplify environmental interaction, landing on the seabed is often preferred. However, not all seabed types are suitable for this approach, and the turbulence generated by thrusters can displace sediment or debris, potentially reducing visibility and altering the integrity of collected samples [11].

The comparison by F. Fish et al. [25] demonstrates the efficiency differences between a typical propeller and small marine mammals (cetaceans). This graph highlights the potential of bio-inspired propulsion compared to conventional propeller systems. It shows that marine mammals exhibit higher efficiency across all thrust coefficients; in other words, swimming-based propulsion remains superior for both high and low thrust generation. As conventional propellers already operate near their maximum efficiency, adopting bio-inspired design principles becomes an inevitable step toward improving overall propulsion performance.

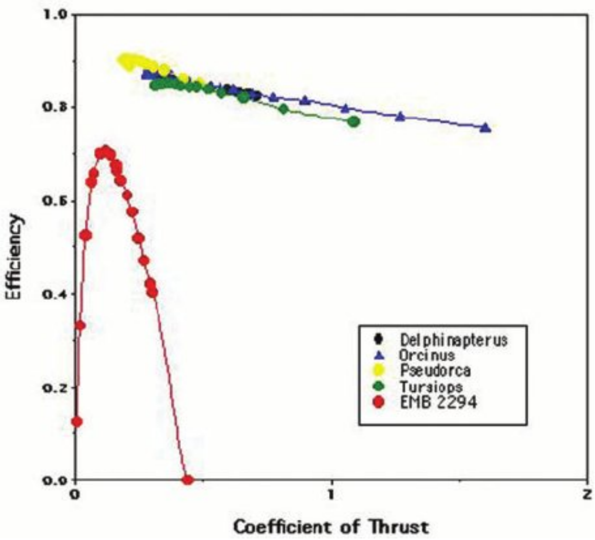

Figure 1.7: Comparison of relationships of propulsive efficiency and thrust coefficient for four species of small cetaceans and a typical marine propeller [25]

Bio-inspired propulsion offers a direct opportunity to integrate alternative current energy harvesting. The motion of fish tails exhibits similar dynamics to flapping foils. Therefore, bio-inspired designs have the potential to serve as both efficient propulsors and effective energy harvesters in the North Sea.

When considering long-term monitoring, an important factor is system maintenance and scalability in production. Complex systems with specialised components generally require more maintenance due to a higher likelihood of mechanical failure. Moreover, scaling up the production of such systems can be challenging and costly. A relevant analogy can be found in the automotive industry: electric motors, which contain far fewer separately moving parts than combustion engines, require significantly less maintenance and offer longer operational lifetimes due to regenerative braking [26]

Similarly, the propulsion system of an AUV consists of many specialised moving parts. In contrast, the propulsion mechanism of a fish relies on a soft, continuous body motion without separately moving components, making it inherently simple. This contrast is shown in Figure 1.8. Consequently, bio-inspired propulsion designs could require significantly less maintenance, which is highly advantageous for long-term underwater monitoring.

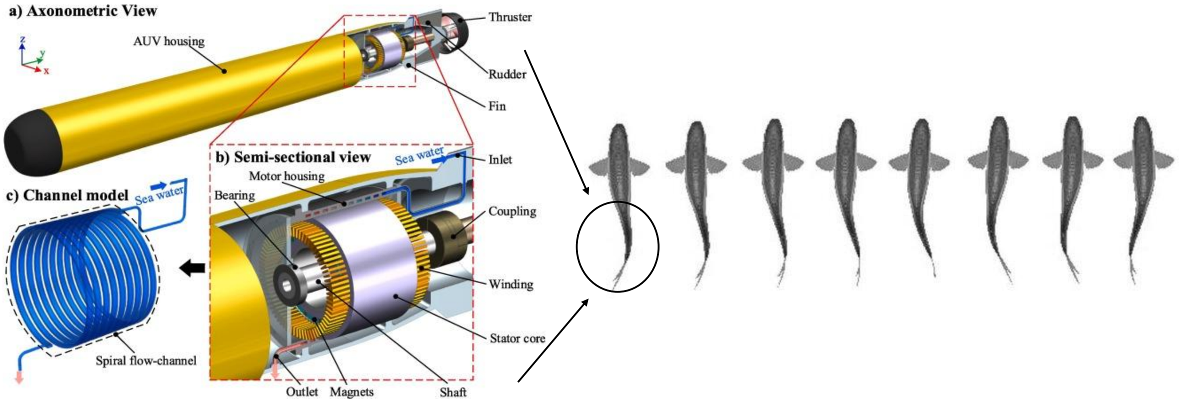

Figure 1.8: AUV propeller mechanism parts complexity [27] versus soft fish simplicity [28]

One of the most efficient fish is the Remora suckerfish. The Remora suckerfish uses the suction disc on its head to attach itself to other animals such as sharks, cetaceans, sea turtles or rays. This gives them protection from predators and the opportunity to feed off of hosts' parasites or leftovers. The biggest advantage is the reduced energy consumption of the suckerfish when hitchhiking with other animals. These suckerfish can be transported over large distances with minimal effort [29].

Suction-based attachment systems have been employed in climbing robots for offshore wind farm (OWF) maintenance above the water surface. These include magnetic, suction/friction, and bio-inspired mechanisms [16]. For instance, a climbing robot developed by M. Hernando et al. [30] uses a turbine-driven motor to generate a vacuum for adhesion. Underwater application of suction devices remains largely unexplored, though their integration could improve station-keeping, reduce energy consumption, and simplify vehicle design. Integrating such a mechanism could address station-keeping challenges, thereby conserving energy and reducing system complexity—particularly in OWF environments where suitable suction surfaces are widely available.

Research on the sucker disc of the Remora sucker fish has been performed in detail by Y. Wang et al. [29], S. Wang et al. [31], and P. Zhang et al. [32]. They focus on the attachment and detachment mechanism, aiming to mimic the sucking technique that the real suckerfish uses. This is outside of the scope of this research, and therefore, the attachment method will not be discussed in this research.

Offshore wind farms provide a favourable environment for remora-like monitoring robots. These robots can attach to monopile structures for station-keeping and current energy harvesting. While swimming, they exhibit minimal environmental interference and higher propulsion efficiency compared to conventional underwater robots. Furthermore, since offshore wind farms require frequent maintenance, these robots could take advantage of maintenance vessels to hitchhike between wind farm sites and the coast [33].

Bio-inspired design provides a compelling approach to combine efficient propulsion with in-situ energy harvesting for underwater monitoring systems. By emulating the swimming mechanisms of marine organisms, such as the swimming motion of fish and cetaceans, robots can generate thrust more efficiently and also efficiently harvest energy from ambient currents. This dual functionality not only reduces overall energy consumption but also simplifies mechanical complexity, enhancing system reliability for long-term deployment. Such integrated bio-inspired solutions are particularly advantageous in offshore wind farm environments, where continuous operation, minimal maintenance, and energy autonomy are critical for sustained monitoring.

1.4. Research question

Based on the challenges identified in current underwater monitoring systems—including limited operational endurance, high costs, and complex deployment—this research focuses on developing a bio-inspired underwater robot that combines efficient propulsion with energy harvesting capabilities. The aim is to design a system that can swim efficiently like a fish, while also converting current-induced motion into usable electrical energy when stationary. By integrating these functionalities, the robot can operate for extended periods with minimal maintenance, making it suitable for long-term ecological monitoring and offshore wind farm applications.

The central research question is defined as:

> *What underwater mechanical structure can efficiently function as a propulsion system and as an energy harvester from ocean currents when stationary, while maintaining a simple system?*

To address this question, the design is guided by several key considerations:

- **Efficient propulsion:** The robot should use bio-inspired swimming mechanisms to maximise thrust while minimising energy consumption.
- **Energy harvesting:** The system should effectively convert ocean currents into electrical energy during stationary operation.
- **Mechanical simplicity:** The design should minimise the number of moving parts to reduce maintenance requirements and increase reliability.
- **Environmental compatibility:** The robot should operate safely in marine environments without negatively impacting local ecosystems.
- **Practical feasibility:** The design should be realistic to produce, deploy, and operate under real-world offshore conditions.

By meeting these objectives, this research aims to develop a practical, integrated underwater robot that bridges the gap between conventional AUV/ROV limitations and the potential of bio-inspired, energy-autonomous underwater monitoring systems.

The report is structured as follows: The literature review (Chapter 2) gives an overview of the important parameters concerning efficient bio-inspired propulsion and harvesting, and determines the fundamental components of the internal system. The design methodology (Chapter 3) describes the methods that have been followed to structurally and goal-oriented develop a new design. The experimental testing (Chapter 4) gives an overview of the tests that have been performed from a methodological perspective. Additionally, this chapter discusses the results from each test and how this is used for further iterations or conclusions. Lastly, the discussion and conclusion (Chapter 5) discuss the findings of this research, what this means for the feasibility of the final design and how future research can improve the design concept.

2

Literature review

The literature review forms the foundation for establishing the design requirements and methodological choices of this project. It examines the current state of underwater propulsion and energy harvesting technologies, with a particular focus on bio-inspired approaches that integrate both functions. By analysing how propulsion efficiency and energy extraction performance are quantified, this chapter outlines the key parameters that determine whether a design is suitable for operation in low-current marine environments such as the North Sea.

In addition, existing actuation and harvesting concepts—ranging from conventional propellers to flapping foils and soft-body mechanisms—are reviewed to identify their strengths, limitations, and relevance for long-duration autonomous monitoring. Together, these insights provide a framework for defining the design requirements of a combined propulsion and energy harvesting system, and they help guide the selection of an internal actuation strategy for the final concept.

Finally, this chapter evaluates a range of propulsion and harvesting systems using data reported in the literature, allowing for a systematic comparison of their performance, feasibility, and integration potential. Based on this assessment, the most suitable system architecture is identified to support the design choices made in the following chapters.

2.1. Setting efficient propulsion requirements

Understanding and defining the requirements for efficient fish-inspired propulsion is essential for developing a propulsion system that performs reliably in low-current marine environments. This section introduces the fundamental principles underlying fish-like locomotion, focusing on the hydrodynamic mechanisms that enable efficient thrust generation through oscillating or flapping motions.

To establish clear efficiency requirements, the first subsection 2.1.1) identifies the key parameters that determine propulsion efficiency in fish-like swimming, providing a quantitative basis for evaluating and comparing design options. The second subsection (2.1.2) reviews existing bio-inspired underwater propulsion systems, assessing their performance, limitations, and relevance for the present design. Together, these components form a framework for defining the propulsion criteria used throughout the remainder of this work.

2.1.1. Fish-like propulsion efficiency parameters

Borelli was the first, in 1680, to suggest that fish generate forward motion primarily through tail movements rather than by rowing with paired fins. It took another two centuries before a deeper understanding of how physiology influences thrust and drag emerged, largely enabled by photographic advancements in the late 1800s [34]. Although the understanding of swimming fluid dynamics has since matured, key aspects of the swimming behaviour of fish, marine mammals, and sharks remain insufficiently understood [35]. A landmark example is Gray's paradox (1936), which questioned how dolphins could produce enough thrust to overcome the drag predicted at their high swimming speeds [36, 37]. While the paradox has since been resolved, the various explanations proposed—ranging from boundary-layer flow characteristics [37] and enhanced thrust generation through tail motion [38] to revised definitions of thrust and drag [39]—highlight the complexity of swimming hydrodynamics and our incomplete understanding of its governing mechanisms.

Despite these gaps, substantial evidence links specific parameters to thrust production, drag reduction, and overall swimming efficiency [40]. Swimming behaviour is often studied through oscillating-foil models; however, accurately reproducing natural swimming motions remains challenging [41, 42].

The most important parameter mentioned in swimming analysis is the Strouhal number [36, 40, 43, 36, 44, 45, 46]. This dimensionless number is defined as the ratio of flapping to forward speed [47], and can be written as shown in Equation 2.1.

$$St = \frac{fA}{U} \tag{2.1}$$

The Strouhal number (St) describes the relationship between the flapping frequency (f) and flapping amplitude (A) relative to the incoming flow speed (U). A schematic illustration is provided in Figure 2.1. The amplitude (A) can be determined from the angle of attack (α) and the body length (L).

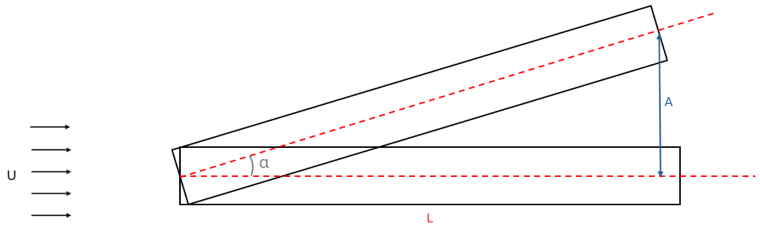

Figure 2.1: Schematic to determine the St number for the underwater robot

For swimming or flying animals, the ideal Strouhal number lies in the range 0.2 $< St <$ 0.4 [43]. An important question is whether this range is coincidental or related to swimming efficiency. According to Taylor et al. [43], this range applies to a wide variety of species, including bony fish, dolphins, sharks, birds, bats, and insects. They argue that such convergence is unlikely to be coincidental. Given the broad range of morphological and physiological traits across these species, one would expect the Strouhal number to scale accordingly.

As frequency, speed, and amplitude scale with body mass, the residual variation in the optimal Strouhal number would also need to scale to maintain a consistent value. However, this is not observed at cruising speed, which represents the preferred swimming or flying speed for each species. This suggests that a common factor is constraining the Strouhal number—namely, aerodynamic or hydrodynamic principles. A survey of Strouhal numbers across species is shown in Figure 2.2.

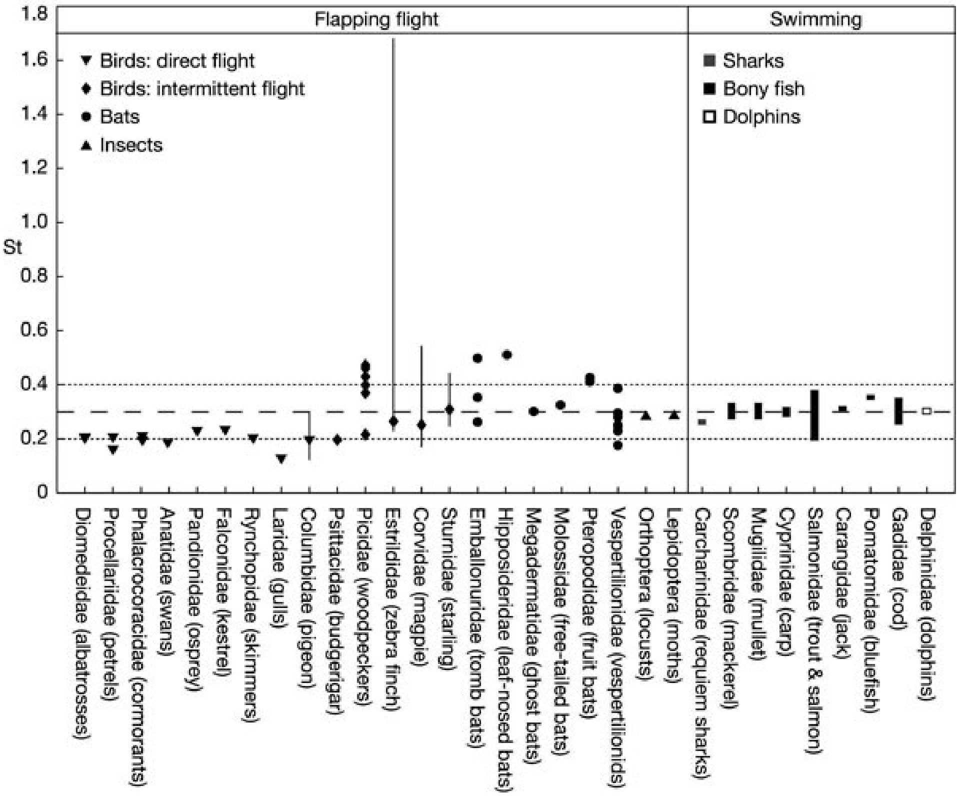

Figure 2.2: Strouhal number for a range of species from Taylor et al. [43]

These results are remarkable given that the species surveyed operate in different media, possess distinct body shapes and surface characteristics, and use various flapping modes. Yet their Strouhal numbers converge within the same narrow range. Because evolution tends to optimise for efficient propulsion, this convergence strongly suggests that the observed range represents a biological optimum. Therefore, the Strouhal number will be considered a key efficiency parameter, and an efficient bio-inspired underwater robot should operate within this range.

The Reynolds number appears not to influence the St number. The dimensionless Reynolds number (Re) is defined as the ratio of inertial to viscous forces acting on a body moving through a fluid of given kinematic viscosity [36]. It is expressed in equation 2.2:

$$Re = \frac{\rho U L}{\mu} \tag{2.2}$$

Here, U is the swimming speed, L the characteristic body length, and ρ and μ are the fluid density and kinematic viscosity, respectively. The Re number of most fish lies within the range of 10^3–10^6 [36], with the variation primarily reflecting differences in body size across species. As illustrated in Figure 2.2, species size does not strongly affect the St number.

G. S. Triantafyllou et al. [46] plotted species against their Strouhal numbers in Figure 2.25a, and additionally plotted the Reynolds number versus the Strouhal number in Figure 2.25b. Across a moderate range of Re values, research consistently shows that the Strouhal number converges to the same optimal range [36, 44, 45, 46]. Therefore, regardless of the size or Reynolds number of the underwater robot, the propulsion mechanism should be designed such that the operating Strouhal number lies within this optimal biological range.

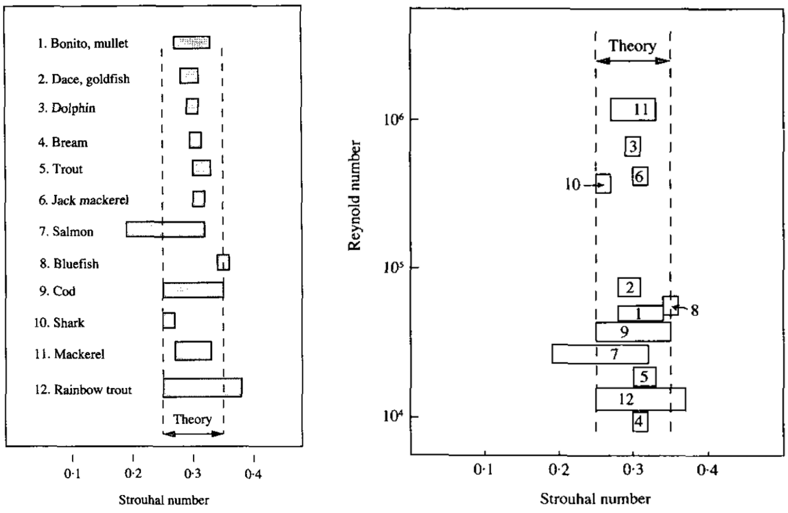

(a) (b)

Figure 2.3: The Strouhal number plotted for various species (a) with different Reynolds number (b) from G. S. Triantafyllou et al. [46]

The size and shape of the fin can be characterised by the aspect ratio (AR), defined in equation 2.3:

$$AR = \frac{h^2}{s} \tag{2.3}$$

Here, h is the vertical span of the fin and s is the fin area. The lift-to-drag ratio is generally argued to be influenced by the aspect ratio, with higher aspect ratios resulting in higher lift-to-drag ratios. This implies that fish with high–aspect ratio fins should be capable of swimming faster than those with lower aspect ratios [48]. Although a high aspect ratio is therefore more efficient, it may also introduce physical disadvantages depending on the species' ecological niche. As a result, many fish operate with relatively low aspect ratios. The sweep angle of the fin has been found not to significantly influence propulsion efficiency [49].

The previous results from Figures 2.2 and 2.3 have been obtained under steady swimming conditions. However, the underwater robot will also need to accelerate from rest. It is therefore necessary to understand how body kinematics enable acceleration while accounting not only for the acceleration of the body's own mass but also the added mass. When a body accelerates underwater, it displaces surrounding fluid, which contributes to the so-called added mass [40, 50].

The acceleration patterns of fish and eel species have been studied, and it is important to note that most species use a distinct motion strategy when accelerating [50]. Nevertheless, the dominant parameters influencing acceleration can be identified. Speed is strongly affected by the Strouhal number (St) because it is constrained by the flapping amplitude (A) and frequency (f) [43]. During acceleration, changes in these parameters relative to steady swimming are particularly significant [50, 51]. Results from anguilliform (eel-like) swimming are shown in Figure 2.4. The relative contribution of changes in amplitude (A) and frequency (f) varies among species [50]. Oscillating or flapping foils have been used extensively to study and replicate swimming behaviour [36, 40, 45, 46, 52, 53, 54, 55, 56]. Distinguishing between static and oscillating foils is essential for understanding swimming mechanics. This line of research is valuable because it enables controlled investigation of swimming fluid dynamics without involving live animals. Moreover, oscillating foil experiments can operate outside the natural kinematic range of swimming species, potentially revealing why animals select specific movement patterns rather than others. To further refine the replication of biological swimming, flexible oscillating foils have also been examined [36, 52]. The relevant findings that contribute to understanding which structural characteristics enable efficient propulsion will be discussed in this section.

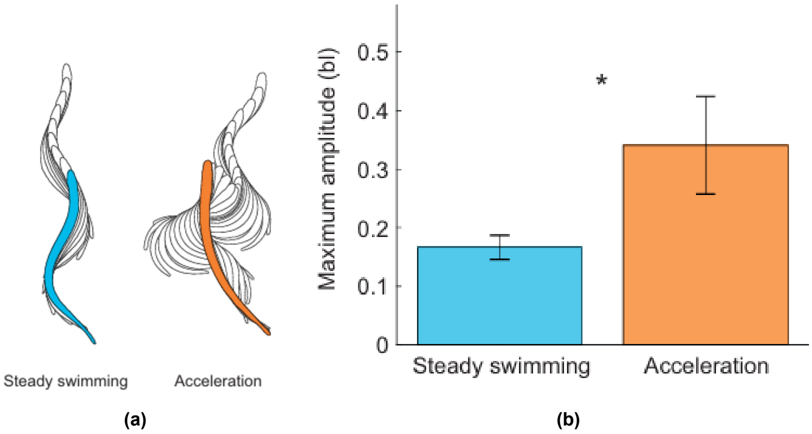

Figure 2.4: The top view shape of steady swimming and acceleration (a) and the maximum amplitude in body length (bl) during steady swimming and acceleration (b) from K. T. Du Clos et al. [51]

Oscillating foils have been tested to determine the most efficient operating range, and these results align with the Strouhal number range of 0.2 $< St <$ 0.4 [35, 42, 46, 53, 54, 56]. The explanation commonly provided is that propulsion efficiency is maximised when the foil's oscillation frequency aligns with the frequency that produces the strongest amplification of wake disturbances, as predicted by linear stability analysis. Under these conditions, the foil generates more coherent and energetic vortices, thereby enhancing thrust production. Furthermore, the controlled and predictable nature of this vortex shedding—dependent on the precise oscillation phase—allows the foil not only to achieve efficient propulsion but also to exhibit improved manoeuvrability, increased lift, and enhanced stealth performance [35, 45, 46].

The angle of attack can be directly related to the lift coefficient [40] and is therefore an important parameter to consider in propulsion design. For animals, the optimal angle of attack (α) typically ranges between 10° and 20° [40, 57, 58]. The definition of α is illustrated in Figure 2.5.

Figure 2.5: Definition angle of attack α [59]

L. Schouveiler et al. [57] compared the efficiency of oscillating foils at angles of attack ranging from 10° to 35°. The most efficient angle of attack was found to be 15°. An increase in the angle of attack appears to correspond to higher efficiencies at elevated Strouhal numbers. The results are presented in Figure 2.6. For the underwater robot, the angle of attack should remain within this range $(\alpha = 10–20°)$ to optimise performance. At higher angles of attack, maximum efficiency is achieved only at higher St numbers.

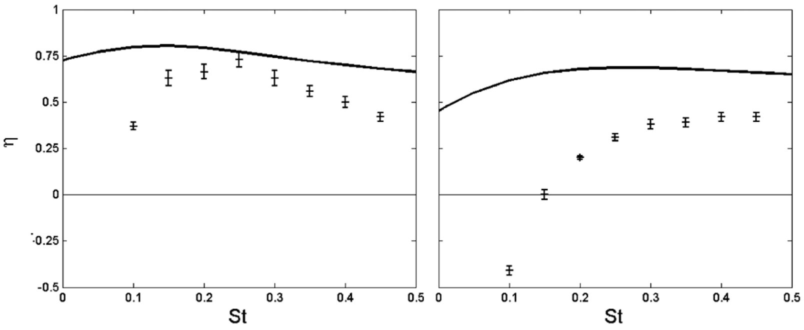

Figure 2.6: Efficiency for different St number with measured (+) and theoretical (—) results for (left) α=15° and (right) α=30° from L. Schouveiler et al. [57]

The study by Q. Zhong and D. B. Quinn [53] investigates the acceleration mechanisms of fish by examining an isolated hydrofoil in a water channel. The research focuses on streamwise manoeuvres, primarily analysing increases in flapping amplitude (L) and frequency (f). The effects of increasing amplitude and frequency are compared and presented in Figure 2.7. The results indicate that acceleration is greater when frequency is increased rather than amplitude. Displacement is normalised by the chord length (c).

These findings are not entirely consistent with the results reported by K. T. Du Clos et al. [51], where amplitude appears to have a larger influence on acceleration. This suggests that the parameters governing acceleration efficiency may be strongly constrained by species-specific physiology and therefore cannot be directly determined for the design of the underwater robot [50].

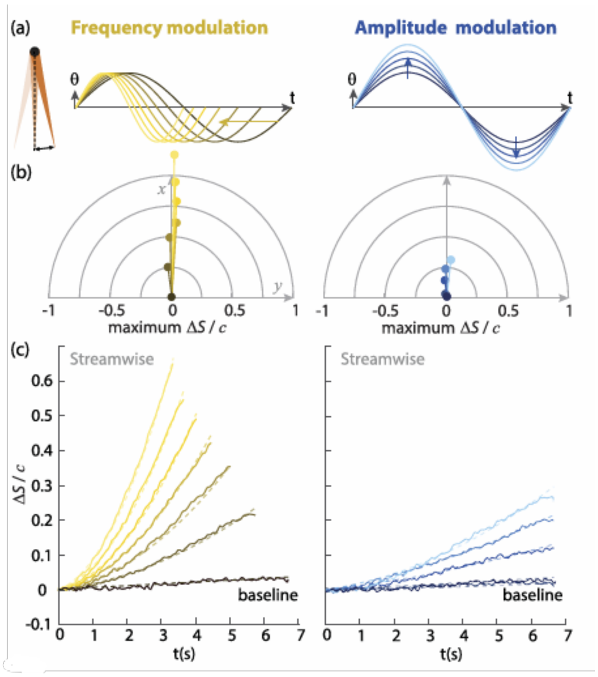

Figure 2.7: Streamwise displacement as a result of increased frequency (f) and amplitude (L) of an oscillating hydrofoil. a) pitching angle profiles, b) maximum displacement in streamwise (x) and lateral (y) direction, c) streamwise displacement over time from Q. Zhong and D. B Quinn [53].

Despite extensive research on oscillating foils, fish still significantly outperform swimming robots [42]. Most studies focus on rigid oscillating foils, but flexible oscillating foils—capable of more closely mimicking natural fish swimming—have recently become a focus of interest [42, 52, 60]. Flexible propulsors have been shown to be particularly advantageous in ground effect [52], which is relevant given that the operational profile of the underwater robot will primarily involve motion near a wall or surface. In the studied cases, the foil is parallel to the ground, differing from the robot configuration. Since these studies demonstrate a positive ground effect, it is assumed that, for the underwater robot, a flexible body will not significantly reduce propulsion efficiency.

More recently, a review by D. B. Quinn and G. Lauder [42] highlighted the potential advantages of tunable stiffness in foils. This advanced approach could leverage the benefits of flexibility while mitigating its drawbacks. However, these findings have only been demonstrated in biological examples. One proposed mechanism for stiffness adaptation is through altering fin shape: for instance, sunfish may modify their response to fluid loading by adjusting their total surface area and the distribution of added area along the body [42]. Because these observations are limited to biological systems, there is currently no clear relationship between specific stiffness patterns and efficiency improvement, and it remains undefined how stiffness should be tuned to enhance propulsion efficiency [42].

In conclusion, the Strouhal number (St) is a key parameter governing propulsion efficiency in both swimming and flying animals, with an optimal range of $0.2 < St < 0.4$. This range will serve as a target for the design of the underwater robot, independent of its Reynolds number. Flapping frequency (f) and amplitude (A) strongly influence acceleration efficiency, though their precise relationship with performance remains incompletely understood. Oscillating foils replicate these dynamics, and flexible foils may further enhance efficiency by better mimicking natural swimming motions.

2.1.2. Bio-inspired underwater propulsion systems

The development of bio-inspired underwater robots began with early prototypes such as the TwiddleFish and RoboTuna at Duke University and MIT, respectively [10]. These designs aimed to replicate fish propulsion and improve understanding of swimming dynamics. Although they did not approach the efficiency and movement capabilities of real fish [61], they laid the foundation for ongoing bio-inspired robotic research and development [10].

Multiple reviews on bio-inspired underwater robots provide an overview of different swimming modes and their overall efficiency. For example, the review by C. H. White et al. [62] classifies designs by their cost of transport (COT) in J/kgm, showing a wide range from 3 to over 5000 J/kgm, despite typical maximum speeds below 1.5 body lengths per second (BL/s). This large variation reflects the absence of a standardized design methodology for bio-inspired underwater robotics. An overview of design possibilities for robots that swim using primarily their body or caudal fin (BCF) is presented in Figure 2.8. Highlighted in red in Figure 2.8 is the swimming mode most suitable for the design of this underwater robot. This mode provides the highest propulsion efficiency, although it sacrifices manoeuvrability. Since manoeuvrability is of lesser importance in this design, which prioritises efficient propulsion and energy harvesting, the (sub)carangiform swimming form is considered the most appropriate choice.

Silicone is primarily used to replicate the soft and flexible parts of a fish's body [63, 64, 65]. However, each design is unique, employing different actuation methods, which results in varying swimming efficiencies. For example, the design by R. K. Katzschmann [63] features a silicone body that can be hydraulically filled on either side to produce motion. While effective, this actuation approach may be difficult to integrate with energy harvesting. Additionally, the authors note that swimming efficiency requires improvement, with the robot achieving only 0.51 body lengths per second and limited operational duration.

Other designs employ actuation via smart materials. The soft robotic fish developed by M. R. T. Fokou et al. [64] uses shape memory alloy (SMA) wires to generate body motion. This design demonstrates an improved swimming efficiency, with Strouhal numbers in the range $0.38 < St < 0.61$. While this approach shows significant potential for energy harvesting, the electrical configuration is complex, requiring multiple wires across separate channels.

Although robotic fish development has improved significantly, fish still outperform fish-inspired underwater robot designs. Accurately mimicking fish swimming has proven challenging, and no standardised framework exists for designing such vehicles. Many prototype tests have been conducted at subopti-

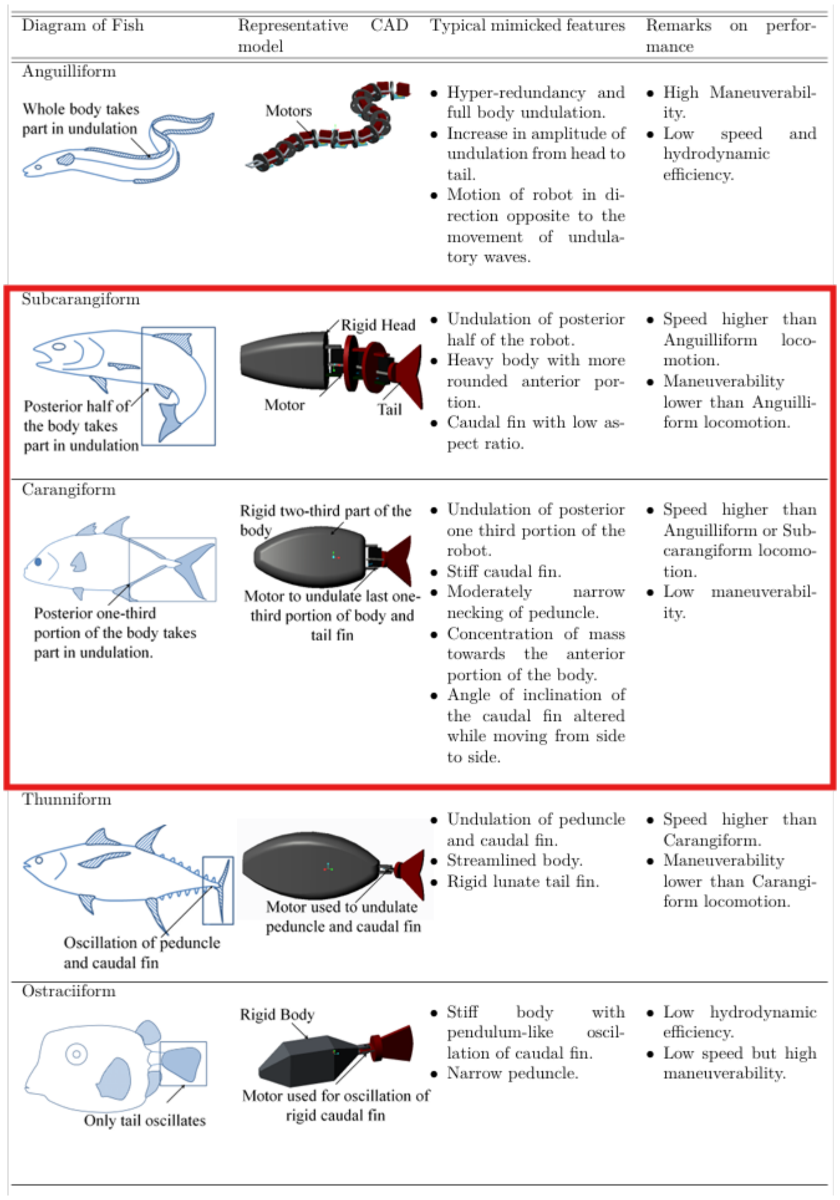

Diagram of Fish	Representative CAD model	Typical mimicked features	Remarks on performance
Anguilliform Whole body takes part in undulation	Motors	• Hyper-redundancy and full body undulation. • Increase in amplitude of undulation from head to tail. • Motion of robot in direction opposite to the movement of undulatory waves.	• High Maneuverability. • Low speed and hydrodynamic efficiency.
Subcarangiform Posterior half of the body takes part in undulation	Rigid Head Motor Tail	• Undulation of posterior half of the robot. • Heavy body with more rounded anterior portion. • Caudal fin with low aspect ratio.	• Speed higher than Anguilliform locomotion. • Maneuverability lower than Anguilliform locomotion.
Carangiform Posterior one-third portion of the body takes part in undulation.	Rigid two-third part of the body Motor to undulate last one-third portion of body and tail fin	• Undulation of posterior one third portion of the robot. • Stiff caudal fin. • Moderately narrow necking of peduncle. • Concentration of mass towards the anterior portion of the body. • Angle of inclination of the caudal fin altered while moving from side to side.	• Speed higher than Anguilliform or Subcarangiform locomotion. • Low maneuverability.
Thunniform Oscillation of peduncle and caudal fin	Motor used to undulate peduncle and caudal fin	• Undulation of peduncle and caudal fin. • Streamlined body. • Rigid lunate tail fin.	• Speed higher than Carangiform. • Maneuverability lower than Carangiform locomotion.
Ostraciiform Only tail oscillates	Rigid Body Motor used for oscillation of rigid caudal fin	• Stiff body with pendulum-like oscillation of caudal fin. • Narrow peduncle.	• Low hydrodynamic efficiency. • Low speed but high maneuverability.

Figure 2.8: Overview of BCF locomotion from A. Raja and A. Thakur [10]

mal Strouhal numbers, resulting in inefficient propulsion. Additionally, numerous designs incorporate joints at the tail, which complicates the system and is unfavourable for achieving a simple, robust design.

It is estimated that there are approximately 33,000 species of fish on Earth [66], each optimised for specific survival strategies through millions of years of evolution. Bio-inspired design typically focuses on mimicking a single species for a particular objective, rather than establishing a general framework for fish-like underwater propulsion that could be adapted for various goals. As a result, many robotic fish designs remain in early prototype stages, are difficult to reproduce, and often fail to achieve practical efficiency. This fragmented and inefficient development process makes it challenging to compete with the reliability and scalability of current underwater monitoring systems.

Therefore, applicable and reproducible designs will be used as the starting point for this research, allowing us to build upon established working principles rather than reinventing them individually. One example is the soft robotic fish developed by S. C. van den Berg et al. [65], which is an open-source design. Their robot uses a DC motor to pull a cable on each side of the body, inducing a tail-flapping motion. Regarding swimming performance, they report that the soft robotic fish achieves a top speed of 0.85 m/s, equivalent to 2.02 body lengths per second (BL/s), at a tailbeat frequency of 5.46 Hz. For tailbeat frequencies above 2.33 Hz, the Strouhal number falls within the range 0.31–0.4. The entire design is available online, making it highly accessible. Because it achieves a desirable Strouhal number, this design is an attractive starting point for the project. However, the actuation method is less suitable for integration with energy harvesting. The design of this robot is shown in Figure 2.9.

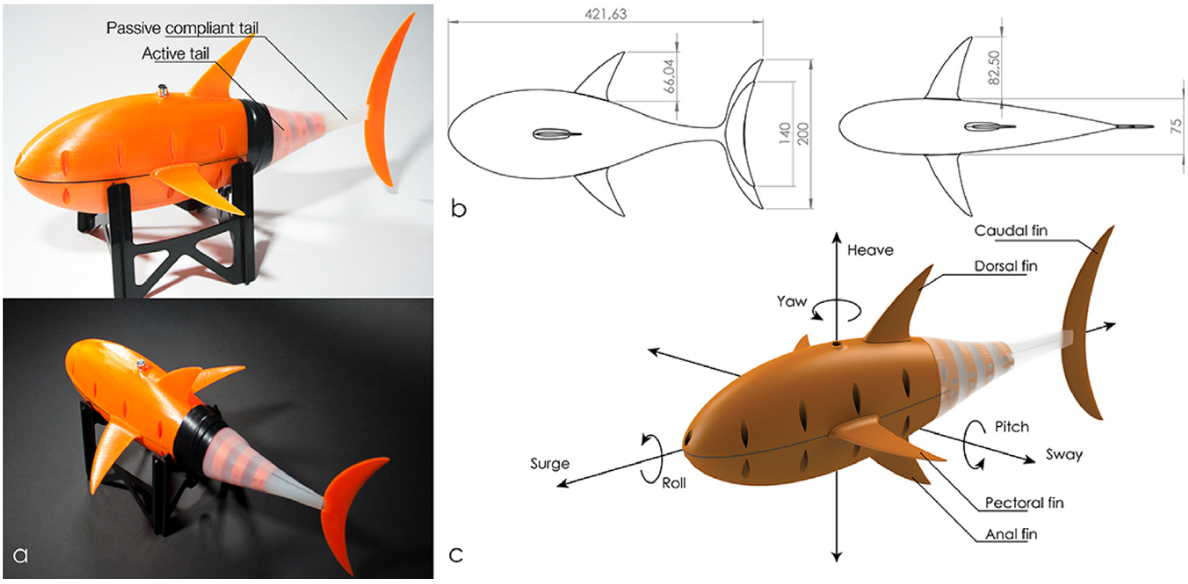

Figure 2.9: Soft robot design of the open source fish (a), top and side view with main dimensions [mm] (b) and terminology used (c) from S. C. van den Berg et al. [65]

The primary concern for this research is that very few bio-inspired underwater robots are capable of switching between propulsion and energy harvesting modes. Previous studies have explored different swimming modes, such as alternating between fish-like and octopus-like motion [67], as well as amphibious robots adapted for both land and underwater operation [68, 69]. However, these examples indicate that advancing the understanding of energy-harvesting vehicles may require approaches beyond conventional bio-inspired designs.

The trout-like robotic fish developed by D. Tan et al. [70] follows a concept similar to that of this project. It is also designed to propel itself or alternatively, harvest current energy. In this report, the trout-like robotic fish is compared to tuna fish and other robotic designs, as its structure is almost entirely rigid except for the short silicone connection between the body and tail. Consequently, its swimming characteristics more closely resemble tuna-like swimming than trout-like swimming. The swimming performance appears to experience similar issues to the TunaBot [62], particularly regarding flapping oscillation and swimming speed. While the Strouhal number (St) is not provided for the trout-like robot in swimming mode, it can be estimated from the reported swimming speed (0.55 body lengths), tailbeat frequency (5.6 Hz), and body length (30.5 cm), assuming an angle of attack between 10° and 20°. This estimation places the St number between 0.9 and 2.3, which is far from the optimal range of 0.2 $< St$ $<$ 0.4, indicating inefficient propulsion.

This estimation is based on the results presented by D. Tan et al. [70]. To further evaluate swimming performance, their water tunnel results are compared with those of real tuna fish. Figure 2.10a shows the test setup and results for the robot, with velocity scaled to a 30.5 cm body length. Figure 2.10b presents results for three different tuna species of varying sizes. Comparing the untethered tailbeat frequency to the speed per body length of the robot and the 32 cm tuna shows that the robot exhibits a much higher tailbeat frequency for the same speed, confirming its lower efficiency. Consistent with this, D. Tan et al. conclude that further research is needed to improve the swimming efficiency of the trout-like robot. A direct comparison between the swimming performance of the trout-like robot and real tuna fish is provided in Figure 2.10.

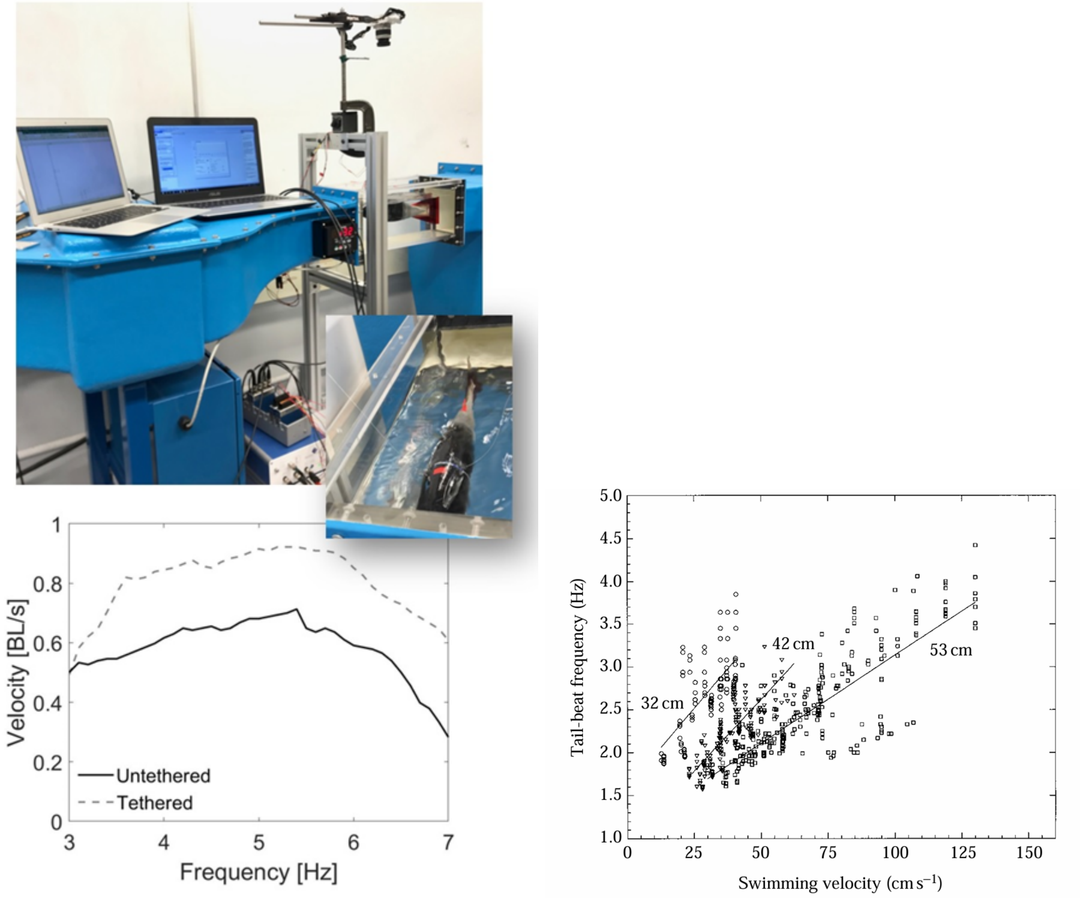

(a) Trout-like robot swimming test setup and performance results from D. Tan et al. [70]

(b) Water tunnel swimming test results of 3 types of tuna fish categorised on length from H. Dewar and J. B. Graham [71]

Figure 2.10: Comparison of the tailbeat frequency [Hz] of the trout-like robot fish (fig 2.10a) and 3 tuna species with different length (fig 2.10b)

Nonetheless, the paper by D. Tan et al. [70] is insightful because they prove that it is possible to develop a bio-inspired underwater robot fish that can both propel and harvest energy. Additionally, their propulsion and harvesting method uses the same principle of piezoelectric materials. This means that the actuation material is the same as the energy harvesting material. This simplification is desirable because it requires few materials, minimizes structural complexity and can easily be applied to other designs.

For the harvesting mode, the trout-like robot is mounted to a rod, and the direction of the current compared to the tail is reversed. This setup creates a greater opportunity to harvest energy due to the unstable and large amplitude oscillation of the tail. However, intuitively, this would require high stiffness in the tail. This may also be the reason for the inefficient swimming performance. So, it seems like a tradeoff has been made between swimming and harvesting efficiency. Here, the harvesting performance has been prioritised.

In summary, the literature highlights the challenges and opportunities in developing bio-inspired underwater robots that combine efficient propulsion with energy harvesting. While early prototypes and recent designs demonstrate various approaches—ranging from silicone-based flexible bodies to smart material actuators—few systems successfully integrate both swimming and harvesting functionalities. Key performance parameters, such as the Strouhal number, flapping frequency, and amplitude, remain critical for achieving efficient propulsion, yet many existing designs operate outside the optimal range. Designs like the open-source soft robotic fish [65] provide a reproducible foundation for efficient swimming, whereas trout-like robots [70] illustrate potential approaches for integrating energy harvesting. Combining these principles offers a pathway to develop robots that perform efficiently in both modes. The following section will explore potential actuation and energy harvesting methods in greater detail, informed by the insights gained from the reviewed systems.

2.2. Setting efficient harvesting requirements

This section focuses on the efficiency parameters of flapping foil energy harvesters, a relatively recent development in marine renewable energy [72, 21, 73, 22, 74]. While conventional energy extraction has relied primarily on turbines, oscillating foil generators offer the potential to achieve comparable power output with lower noise and reduced environmental impact on marine life. Moreover, oscillating foils can operate effectively at lower flow speeds and in shallow waters, significantly expanding their potential deployment areas [21, 22]. The aim of this section is to identify the key structural and operational parameters that maximise energy extraction efficiency for oscillating foil systems. Additionally, this section will consider and compare different energy harvesting methods, including strain-based and rotational mechanisms, to evaluate their feasibility and potential integration into bio-inspired underwater robots.

2.2.1. Flapping foil energy harvesting efficiency parameters

According to W. Liu et al. [75], an oscillating foil can switch between propulsion and energy extraction by pitching the wing at an angle of attack greater than the current-induced angle of attack. This implies that the angle of attack during propulsion is smaller than that used for energy harvesting. The authors also argue that, similar to swimming motion, flexible foils are more efficient than rigid foils for extracting energy. They distinguish between flexibility at the leading edge and the trailing edge. The results of their model are presented in Figure 2.11. It is important to note that these tests were performed using a two-dimensional model, which effectively corresponds to an infinitely large aspect ratio, at a high Reynolds number $(Re = 10^6)$. The results indicate that flexibility at the trailing edge increases energy harvesting efficiency.

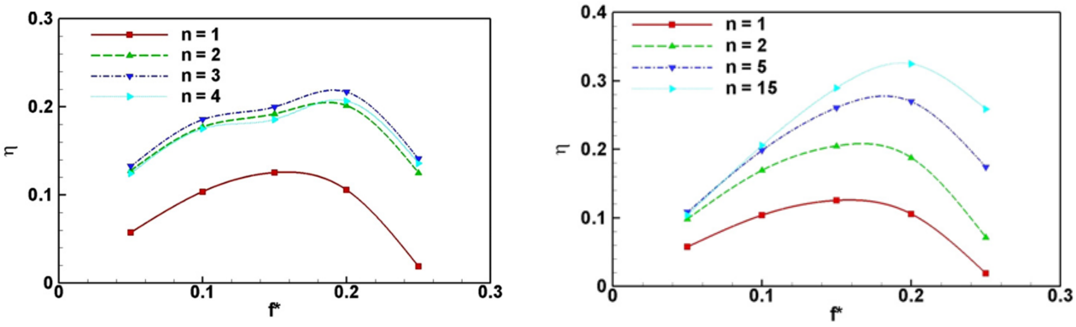

(a) (b)

Figure 2.11: Efficiency of foils with flexible coefficient n with $n = 1$ is a rigid foil for a) the leading edge and b) the trailing edge from W. Liu et al. [75]

The paper by B. J. Simpson et al. [74] researches the most efficient sinusoidal oscillation movement for energy extraction with a foil. Their results show that efficiency is largely dependent on the St number, the angle of attack and the aspect ratio of the foil. The results for 5 different efficiencies are shown in figure 2.12. The purple zone shows the parameters for the highest efficiency. Their most efficient results occurred at an aspect ratio of 7.9, St number of 0.4 and a maximum angle of attack of -34.37°. In this case, the hydrodynamic efficiency may go up to 43 ± 3%. This value is significantly larger than the results of the flexible foil shown in figure 2.11. This means that either the efficiencies obtained by the rigid foil from W.liu et al [75] are not optimal or not operating in the correct window. So the conclusion that flexible foils are more efficient than rigid foils is not assumed in this research. Even more relevant for energy harvesting than for propulsion is that the robot will typically operate near a wall or

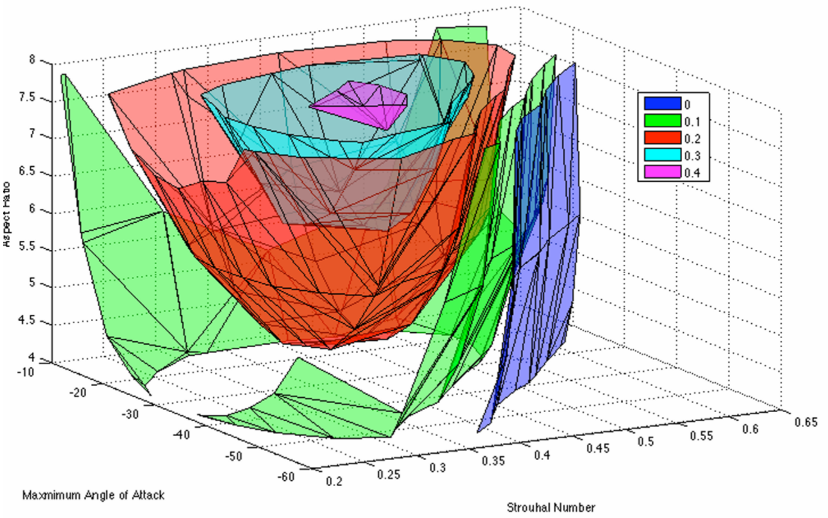

Figure 2.12: Efficiency profile for varying aspect ratio, maximum angle of attack and St number from B. J. Simpson et al. [74]

the seabed. This proximity may influence harvesting efficiency, although it has only been studied by B. Zhu et al. [76] and G. He et al. [77]. Their findings regarding the optimal angle of attack are consistent with those of B. J. Simpson et al. Notably, they report that being near the ground can improve efficiency, although their numerical model predicts lower efficiency values than those observed by Simpson et al. While the reasons for this discrepancy are unclear, it will not be assumed that near-ground harvesting is inherently more efficient.

Conversely, since the observed changes in efficiency are relatively small, it will also not be assumed that proximity to the ground significantly reduces efficiency. The results of Zhu et al. [76] are presented in Figure 2.13. Their study considers a foil parallel to the ground, whereas the underwater robot will operate with a perpendicular orientation. Ground clearance is normalised by chord length. Maximum efficiency is achieved at angles of attack between 30°–40° and a normalised frequency of 0.15. These results indicate that energy harvesting efficiency is higher at larger angles of attack compared to propulsion. According to their study, efficiency is also dependent on Reynolds number, unlike propulsion, with maximum efficiency obtained by decreasing frequency while increasing Re.

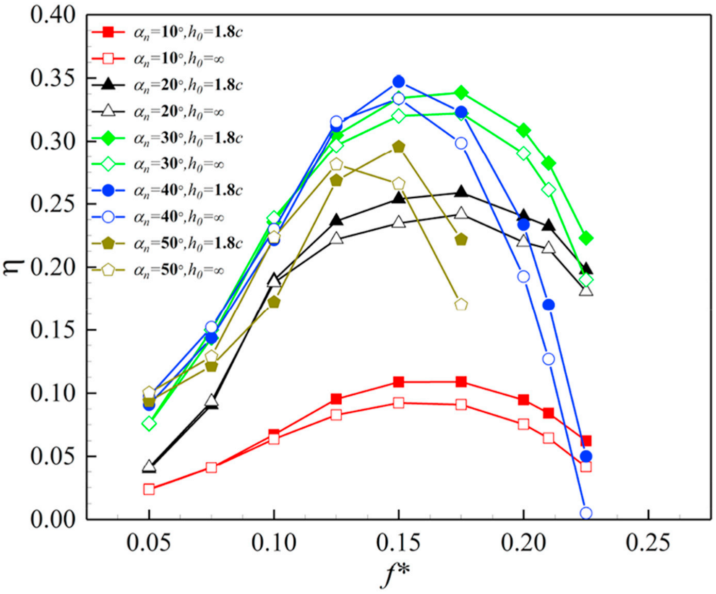

Figure 2.13: Harvesting efficiency per dimensionless frequency for varying angle of attack α and normalised ground clearance h_0/C from Zhu et al. [76]

The angle of attack is not the only factor distinguishing propulsion from harvesting modes. A key component influencing the foil's mode is the relationship between the angle of attack and the pitching moment $M(t)$. This relationship determines whether the foil transfers energy into the fluid (propulsion) or into the structure (harvesting) when the foil is pinned in a stationary position. A visualisation of this is shown in Figure 2.14. The relationship between M and α traces a closed loop over a single oscillation period, with the direction of the loop indicating the foil's mode. In Figure 2.14, the loop progresses in a counter-clockwise direction over time, indicating that energy is transferred from the current U_∞ to the foil (harvesting). Conversely, if the loop moves clockwise, energy is transferred from the foil to the fluid (propulsion).

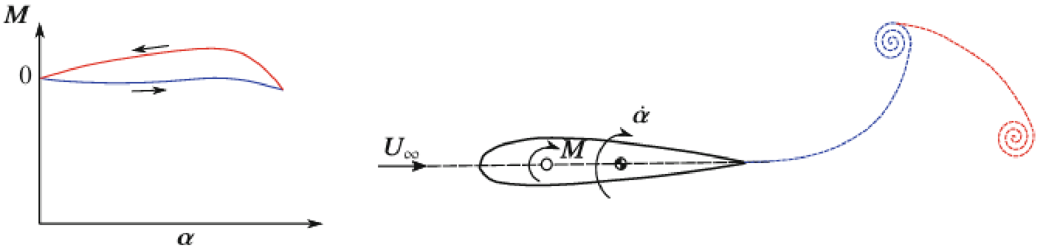

Figure 2.14: Relation between the pivot moment M and dynamic angle of attack $\dot{\alpha}$ [40]

To understand the energy balance of this system, the principle of conservation of energy is applied. This principle is equally valid for energy harvesting, but under reversed conditions. Conservation of energy requires that the power input (P) equals the sum of the work done by the thrust (TU) and the rate of increase in kinetic energy lost to the fluid per unit time [36, 55], as expressed in equation 2.4. Note that this formulation does not account for viscous effects

$$P = TU + E \tag{2.4}$$

Bio-inspired energy harvesting techniques have been less studied than propulsion methods. This may be caused by the fact that animals are not inherently energy harvesters through current-induced motion. Therefore, it is more challenging to present clear parameters that influence the efficiency. From the results presented in this section, it is possible to state some similarities and differences between the propulsion and harvesting modes. These are presented in table 2.1.

Table 2.1: Propulsion and harvesting modes parameter comparison

	Propulsion	**Harvesting**
St number	0.2 $<$ St $<$ 0.4	0.2 $<$ St $<$ 0.4
Re number influence	No	Yes
Angle of attack (degrees)	10-20	30-40
Flexible foil	Yes	No
Pivot point	Forward (clockwise relation)	Back (counter-clockwise relation)
Aspect ratio	Higher	Higher

So, the efficiency of flapping foil energy harvesting is influenced by several key parameters that partly overlap with propulsion requirements but also present distinct differences. Both propulsion and harvesting modes benefit from maintaining a Strouhal number within the optimal range of 0.2–0.4 and a relatively high aspect ratio. However, unlike propulsion, harvesting efficiency is sensitive to the Reynolds number and achieves maximum performance at larger angles of attack (30°–40°). Furthermore, while flexible foils improve propulsion efficiency, rigid or less flexible foils are preferred for energy harvesting. The location of the pivot point and the resulting phase relationship between the pitching moment and angle of attack also differentiates the two modes: a forward (clockwise) pivot relation favours propulsion, whereas a rearward (counter-clockwise) pivot relation enables effective energy extraction. These parameters collectively define the design window for efficient bio-inspired energy harvesting and will guide the development of an integrated propulsion-harvesting system for the underwater robot.

2.2.2. Energy harvesting method

There are various methods to convert mechanical energy into electricity. This subsection summarises existing power take-off (PTO) devices and generators, evaluating which approaches are best suited for this design. Energy harvesting methods are employed across a range of applications, including regenerative braking, vibration energy recovery, and wind or wave energy conversion. The specific devices used for each application vary widely. When selecting a suitable conversion method, it is crucial to consider the work input as well as the motion and frequency of the driving mechanism. For the underwater robot, these parameters are effectively fixed, which eliminates many conventional energy harvesting options. Therefore, this section focuses only on methods relevant to oscillatory motion at low frequencies. The choice of energy conversion can influence the design of the robot's body movement, and conversely, the body motion may be adapted to suit the most efficient conversion approach. A schematic of the two possible energy harvesting modes is shown in Figure 2.15.

The primary distinction between the two energy harvesting configurations lies in the oscillation frequency and amplitude. In the pinned configuration, the body exhibits larger amplitudes at lower frequencies, whereas the clamped configuration typically results in smaller amplitudes at higher frequencies. Research on flapping foil energy harvesting generally employs the pinned configuration [72, 21, 73, 22, 74]. However, these studies do not explicitly specify the energy conversion method used. Therefore, further investigation is necessary to identify the most suitable energy harvesting mechanism for the underwater robot. Based on the results from Section 2.1, the estimated oscillation frequency of the body ranges between $0.0\overline{3}$ and 1.41 rad/s, corresponding to 0.21–8.9 Hz.

The key difference between the propulsion and harvesting modes lies in the freedom of the body's front end. During propulsion, the front end is free, whereas in harvesting mode, it is attached to a rigid structure, restricting its motion. Two primary attachment options exist: pinned or clamped. Each configuration allows for different energy conversion methods. When pinned, the body undergoes rotational oscillatory motion around the pivot point, enabling multiple rotational energy harvesting options. When clamped, energy can be harvested through the strain generated by the bending of the body.

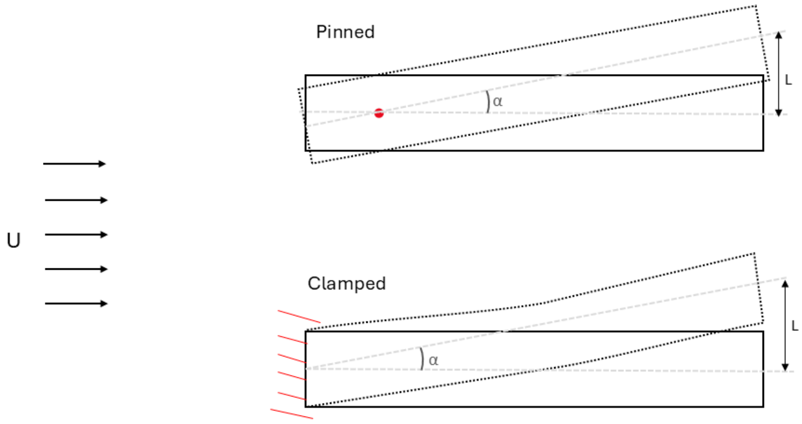

Figure 2.15: Schematic of the pinned and clamped stationary position of the underwater robot.

Commercially applied methods for energy harvesting around a rotating shaft include regenerative braking, wave energy turbines, and pendulum-based electricity generation using an electric motor [78, 79]. In regenerative braking, the electric motor can switch between propulsive and energy harvesting modes. This dual-mode capability is particularly advantageous, as the direction of the motor's rotation determines the mode of operation. However, in this design, a single generator may not be sufficient for both propulsion and harvesting, since the body's motion differs between the two modes. If a configuration enabling a single motor is feasible, using an electric motor would be beneficial.

The regenerative braking principle can be implemented with various types of electric motors, whose efficiency varies with operating conditions [80]. Maximum efficiency is typically achieved at higher rotational speeds, meaning that the motor's performance as a generator improves at higher oscillation frequencies [79]. This must be considered because the pinned-body design of the robot will oscillate at very low frequencies, potentially limiting the output efficiency of the energy harvesting mode.

The body's motion will not involve a full rotation, as in cars or turbines, but will instead be oscillatory. To generate electricity, this bidirectional oscillation must be converted into unidirectional rotation. Several mechanisms can achieve this. One example is the pendulum system shown in Figure 2.16. Here, the shaft is connected to a torsional spring, which stores kinetic energy as it is wound by the pendulum. When the spring's tension exceeds the stall torque of the motor-gear combination, it drives the DC motor and gearhead to rotate, converting the stored mechanical energy into electrical energy.

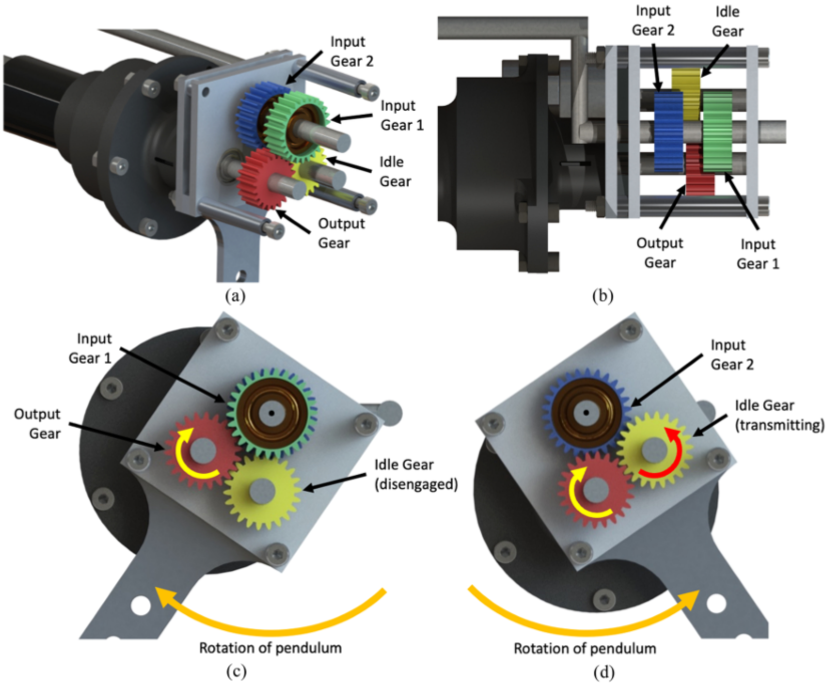

Figure 2.16: Motion translation during pendulum motion to unidirectional motion: (a) Gear assembly, (b) Top-down view of gear assembly, (c) Power transmission during clockwise rotation of the pendulum, (d) Power transmission during anti-clockwise rotation of the pendulum. [81]

The output of the pendulum system depends on the spring stiffness, with a stiffer spring producing a higher electrical voltage. However, the pendulum's mass of 1.55 kg is expected to yield a greater energy output than the body movement of the underwater robot. Consequently, the power output of the pendulum-based energy harvester is higher for this specific system. Nevertheless, it remains relevant to compare power outputs of rotational low-frequency energy harvesters. The voltage and power output per oscillation frequency for both the pendulum and a low-frequency electrical motor are presented in Figures 2.17 and 2.18. The electric motor results in Figure 2.18 provide a more realistic estimate of the power and voltage output for the underwater robot, as the pendulum's work input is likely higher than what the robot can achieve. Additionally, the trends differ: the spring-based system reaches peak power at around 1.25 Hz, while the electromagnetic harvester's peak output occurs at higher frequencies, as demonstrated by X. Yang et al. [82], who observed peak voltage outputs between 2–10 Hz depending on acceleration.

Most wave and current energy harvesters employ rotational devices such as springs or electric motors. For instance, wave gliders and similar converters use ball screws to transform tension into rotational motion [83, 84], while wave foils employ spring-damper systems to convert oscillatory motion induced by ship pitching into energy [85]. These methods are well-studied and widely applied. However, converting bidirectional oscillatory motion into unidirectional rotation typically requires intricate mechanical structures. While these mechanisms are generally reliable, they present structural challenges and may require significant maintenance [86].

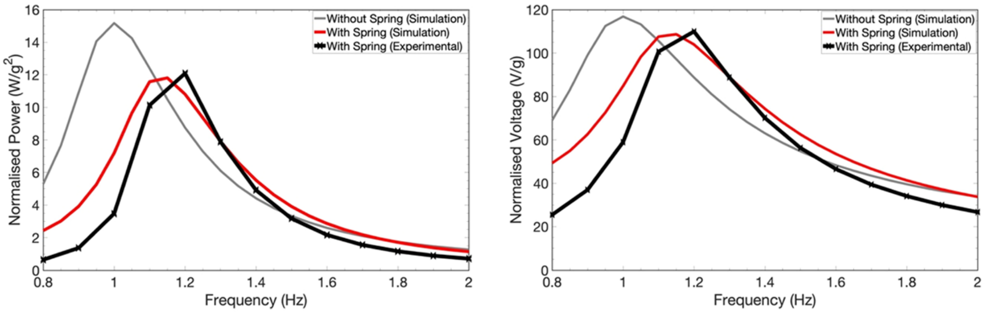

(a) (b)

Figure 2.17: Normalised power (a) and voltage (b) output of the pendulum torsional spring per frequency (g=0.192) from J. Graves et al. [81]

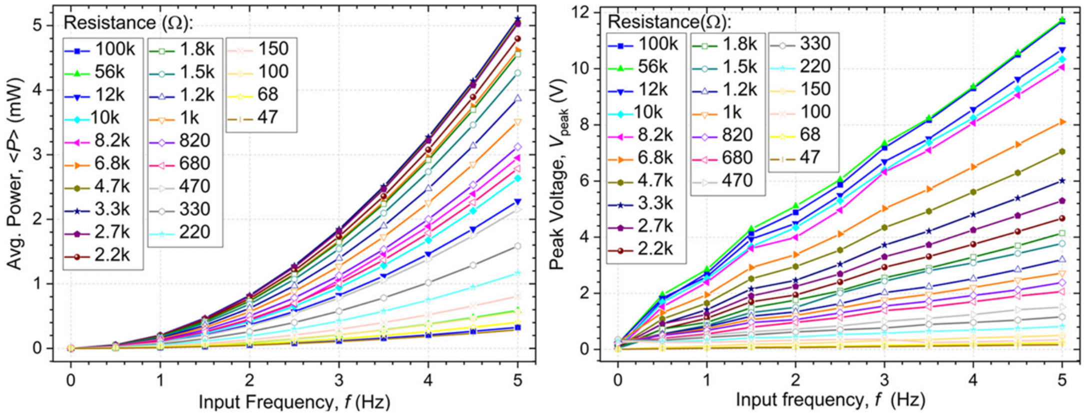

(a) **(b)**

Figure 2.18: Average power (a) and peak voltage (b) per frequency of an electric motor energy harvester for different internal resistance of the coils from P. Rolo et al. [87]

In contrast to energy generation via rotational motion, strain energy can be directly converted into electricity using piezoelectric devices [88, 89]. Strain within the robot's body can be induced by clamping the front of the robot in the harvesting mode. In this configuration, the robot's body behaves like a cantilever beam with a mass at the end—in this case, the tail. A schematic of such a structure is shown in Figure 2.19. For the underwater robot, the end of the beam will oscillate in response to environmental forces such as tides or currents, generating strain that can be converted into electrical energy.

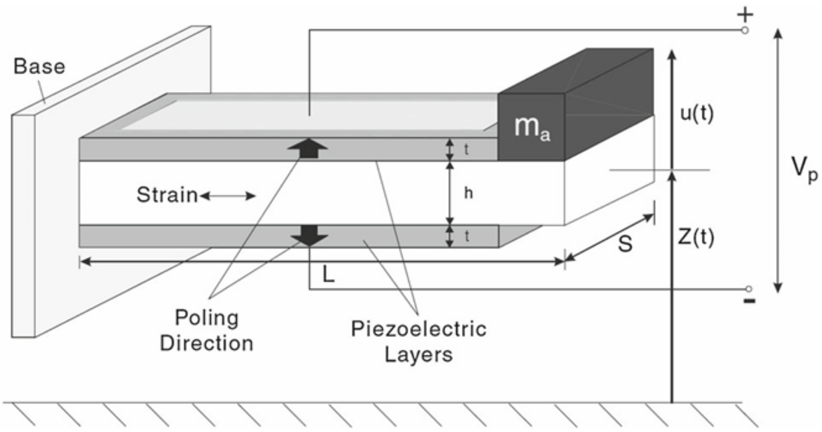

Figure 2.19: Piezoelectric device schematic with tip mass from S. Priya and D. Inman [90]

The design by D. Tan et al. [70] is an example of a strain-energy harvester that uses the piezoelectric material MFC [91]. The robotic fish design and the corresponding harvesting results are presented in Figure 2.20. The energy-harvesting results are based on a current flowing in the opposite direction of the swimming direction to enhance the flapping amplitude and frequency. MFC is a piezoelectric composite and is relatively stiff compared to other piezoelectric materials. It is chosen because it can generate a high voltage and current output per deflection. However, this stiffness is assumed to limit the tail motion of the robot in propulsion mode, making the robot less efficient compared to, for example, the fish developed by S. C. van den Berg et al. [65].

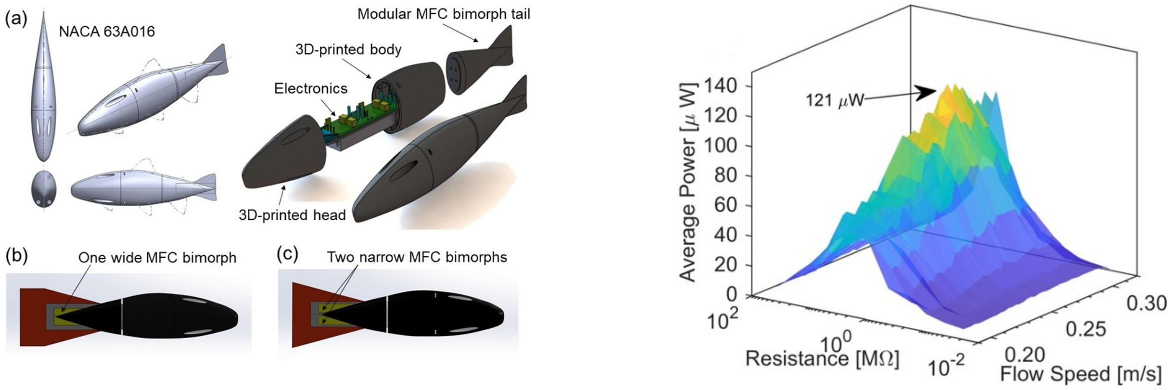

(a) Self-propelling and current energy harvesting trout-like robot fish design [70]

(b) Trout robot harvesting results [70]

Figure 2.20: Trout-like robotic fish: (a) design overview, (b) harvesting performance.

Based on the comparison in Table 2.2, strain-based energy harvesting is the most attractive option for the bio-inspired underwater robot. It offers lower structural complexity, higher potential efficiency, and better compatibility with the flexible body design.. While rotational methods are well-established and can provide high energy output, their complexity and stiffness requirements make them less practical for this specific application. Within strain-based approaches, piezoelectric polymers such as PVDF are preferred due to their mechanical flexibility and commercial availability, allowing for a practical implementation without extensive custom development. Ultimately, the exact material and device selection will depend on what is readily available on the commercial market, ensuring that the chosen system can be feasibly integrated into the underwater robot while meeting the operational frequency and energy requirements.

Table 2.2: Rotational and strain energy harvesting method comparison

	Rotational	**Strain**
Resonate frequency (Hz)	0-10	20-30
Output (V)	0-20	0-30
Structural complexity	High	Low
Efficiency improvement potential	Lower	Higher
Stiffness	High	Low

2.3. Integrated system

There are many actuation options for the bio-inspired underwater robot. Ideally, the actuation method is the same as the harvesting method, in order to minimise the complexity of the electrical circuit. This reduces the number of components, simplifies assembly, and lowers the risk of system failure. Smart materials have the greatest potential to achieve both modes within a single system.

Smart materials are materials that can change their characteristics in response to external stimuli—for example, changing shape, stiffness, or phase due to variations in temperature or electric fields. Although there is no strict definition, smart materials are often described as materials capable of returning to their original shape when exposed to specific stimuli, or as advanced materials that can intelligently adapt to environmental changes [92]. They can be categorised as active or passive. Passive materials do not change their intrinsic properties but can transfer or dissipate certain forms of energy. Active materials, by contrast, can change their characteristics or convert one form of energy into another [92, 93].

The second category—active smart materials—is the most relevant for this project. Ideally, the bio-inspired underwater robot is actuated by a smart material that can convert electrical energy into mechanical energy during propulsion and convert mechanical energy back into electrical energy during harvesting.

2.3.1. Electromechanical coupling

Electromechanical couplers include shape memory alloys (SMA), piezoelectric materials, magnetostrictive materials, electrorheological materials, and magnetorheological fluids [94]. Magnetostrictive materials and magnetorheological fluids are commonly used for vibration control, shock absorption, and sensing mechanical deformation [94, 95], while electrorheological materials are applied in valves, clutches, brakes, dampers, and mounts [94].

Shape memory alloys (SMA) are temperature-sensitive alloys that return to their original shape when heated, recovering from deformations that occur at lower temperatures [96]. In Figure 2.21, austenite refers to the stiff, heated state of the alloy in its original shape, while martensite refers to the softer, cooled state.

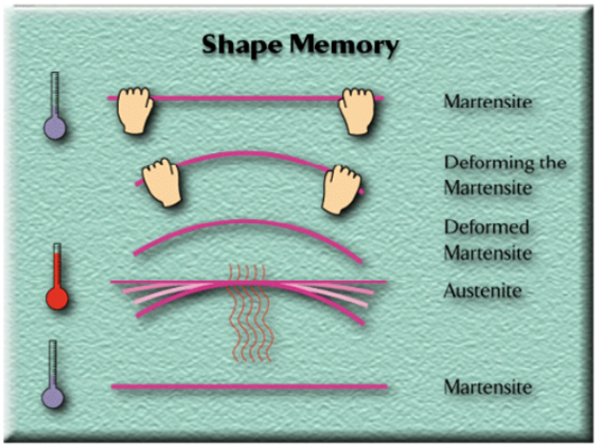

Figure 2.21: Working principle of SMA [94]

SMA has been widely used as an actuator in soft robotics due to its large driving strain, high work density, quiet operation, and low driving voltage. In recent years, researchers have embedded SMA wires into soft silicone materials to create flexible actuators that have been successfully applied to underwater robots [94, 96]. An example discussed earlier in the literature review is an underwater swimmer actuated by eight independent SMA wires on each side—sixteen in total [64]. The actuation strength of these wires is sufficient to achieve swimming at a Strouhal number of 0.61.

SMA wires also have the potential to function as energy harvesters, although this aspect has been studied much less extensively than their use for actuation. Since conventional SMAs respond to temperature, the type of energy they can harvest is primarily thermal energy [97].

A key limitation of conventional shape memory alloys (SMA) as actuators is their slow recovery time. Although SMA wires contract almost instantly when heated, returning to the martensitic (flexible) state requires cooling below a threshold temperature, which can take several seconds to minutes depending on ambient conditions [64]. To maintain continuous motion, the SMA-based robot fish in [64] employs a large number of independently actuated wires. For applications such as soft grippers, this slow recovery is not critical. However, for a bio-inspired underwater robot requiring actuation at 1–5 Hz, conventional SMA recovery is too slow. While adding more independent SMA wires could partially compensate, it also increases system complexity [64].

Magnetic shape memory alloys (MSMA) offer a promising alternative [98]. MSMA responds to a magnetic field rather than temperature, enabling near-instantaneous actuation and recovery [98, 99]. This allows operation at higher frequencies while maintaining similar actuation properties, making MSMA particularly suitable for integrated actuation and energy harvesting systems.

Due to the project's time constraints and scope, the actuation and energy harvesting methods are limited to commercially available devices, meaning only those products that can be readily purchased from suppliers without the need for custom fabrication or extensive development will be considered.

Magnetostrictive materials can function as both actuators and harvesters through electromechanical coupling [94]. However, most commercially available devices are optimized for either actuation or energy harvesting, making dual-purpose application inefficient [100, 101]. Furthermore, commercial magnetostrictive devices are typically stiff and non-flexible, which is unsuitable for the underwater robot design. Their operational frequency is generally much higher than the 1–5 Hz range relevant for this project [94, 100, 101]. While it is possible to purchase the raw material Terfenol-D and an electromagnet [94, 102, 103], significant development effort would still be required to produce a functional device.

Similarly, magnetorheological fluids can theoretically serve as both actuators and sensors, but commercial implementations are specialized for a single function [104, 105]. Like magnetostrictive devices, they are not yet suitable for flexible, soft robotic applications. Emerging designs, such as the self-powered flexible magnetorheological sensor by J. Xu et al. [106], demonstrate the potential of these materials in soft robotics, but they currently lack efficient electromechanical coupling.

Triboelectric nanogenerators (TENG) are primarily used for energy harvesting [107]. Their mechanical output force is weaker than that of piezoelectrics, and their electrical characteristics differ, typically producing higher voltages [108]. TENGs are mostly research-stage devices and are not commercially available, though they show strong potential for future energy harvesting applications [109].

Based on the comparison of energy output density and actuation frequency, piezoelectric materials and SMA wires operate well within the required range for the bio-inspired underwater robot, as shown in Figure 2.22. Both material types exploit electromechanical coupling, enabling the conversion of mechanical energy into electrical power and vice versa. Among the commercially available smart materials, piezoelectric films stand out as the most practical solution. They are readily accessible, require minimal additional development, and offer a simpler and more reliable implementation compared to other electromechanical couplers such as magnetostrictive devices, magnetorheological fluids, or triboelectric nanogenerators. Consequently, piezoelectric materials provide a feasible and efficient approach for integrating both actuation and energy harvesting within the design constraints of this project.

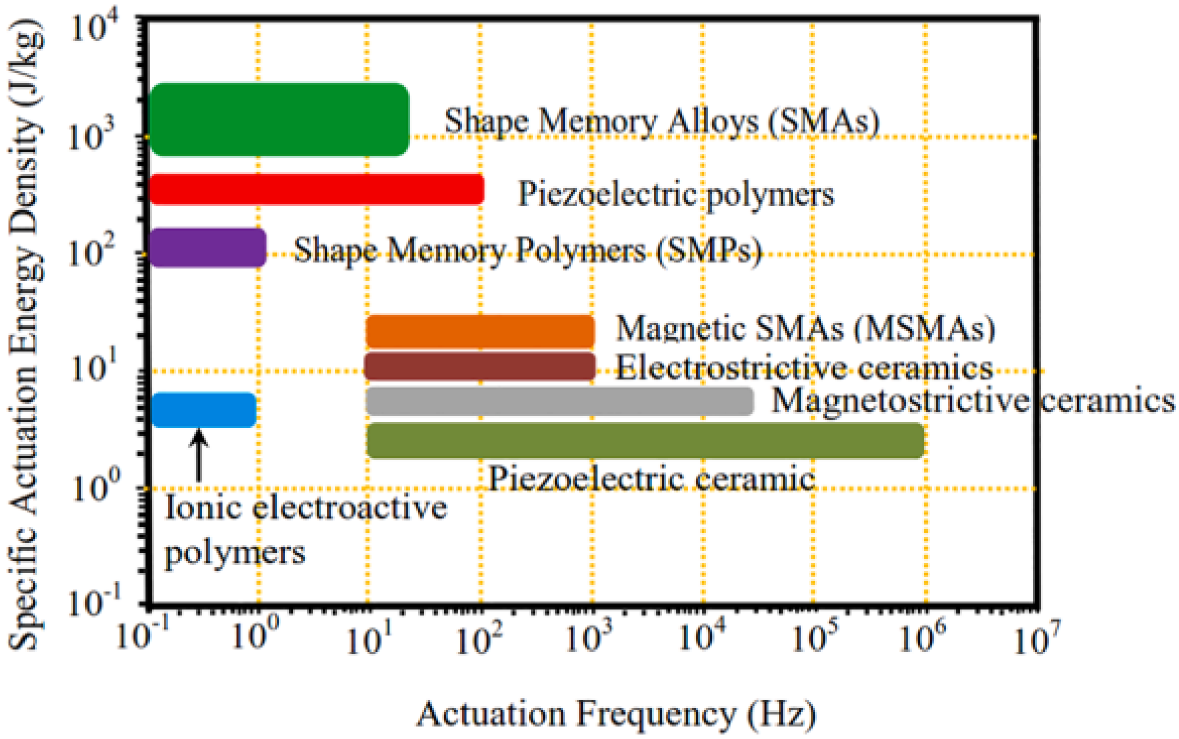

Figure 2.22: Energy density of smart materials per frequency [110]

2.3.2. Piezoelectric materials

Piezoelectric devices have been researched as power take-off mechanisms since the 1970s and continue to develop. These devices are capable of harvesting vibration energy, which includes vibrations generated by machinery, human motion, environmental sources such as wind or sound, or repeated mechanical oscillations. Among the various ambient energy sources, vibrational energy is particularly attractive due to its abundance and accessibility. This kinetic energy can be converted into electrical energy through piezoelectric, electromagnetic, or electrostatic mechanisms. Piezoelectric transducers are often preferred because they are compact and lightweight [88, 111].

When a piezoelectric material is mechanically stressed, its atomic structure deforms, creating a dipole moment that results in a voltage difference across the material. The choice of piezoelectric material strongly influences harvesting performance [88]. Therefore, selecting a suitable material is essential for meeting the operational requirements of the underwater robot. The most commonly used—and most energy-dense—piezoelectric materials for marine applications are Lead Zirconate Titanate (PZT) and Polyvinylidene Fluoride (PVDF) [88, 90]. The key characteristics of these materials are presented in Figure 2.26.

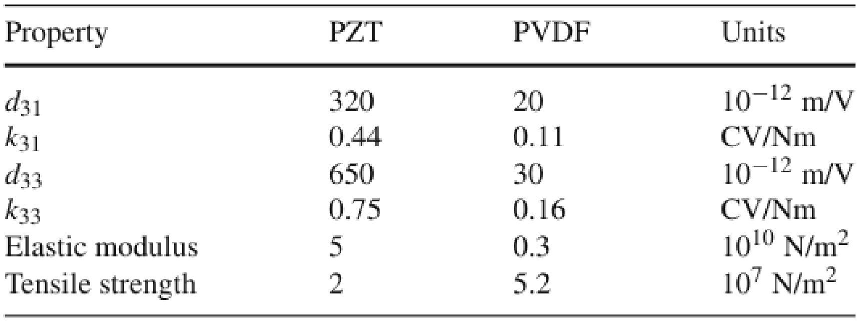

Property	PZT	PVDF	Units
d_{31}	320	20	10^{-12} m/V
k_{31}	0.44	0.11	CV/Nm
d_{33}	650	30	10^{-12} m/V
k_{33}	0.75	0.16	CV/Nm
Elastic modulus	5	0.3	10^{10} N/m^2
Tensile strength	2	5.2	10^7 N/m^2

Figure 2.23: Piezoelectric material properties from A. Jbaily and R. Yeung [88]

Both piezoelectric materials exhibit a common resonance frequency across different experiments, which lies above the expected operating frequency range of the underwater robot. At higher frequencies, selecting a suitable material is relatively straightforward: ceramics such as PZT generate higher energy output at the same strain, making them highly attractive. However, at lower frequencies, operating at resonance becomes more challenging. Consequently, polymers such as PVDF or composite materials (combinations of ceramics and polymers) are preferred for low-frequency applications [112].

H. Li et al. [112] provide an overview of low-frequency piezoelectric applications, with those operating in the frequency range relevant to the underwater robot highlighted in red. This overview demonstrates that low-frequency energy harvesting with piezoelectric materials is feasible. For example, PVDF has been shown to produce a power output of 610 μW.

A bio-inspired underwater application using PVDF is the energy-harvesting eel developed by G. Taylor et al. [113]. Tested in a towing tank, the device demonstrated feasible power generation, with the tail operating at a frequency around 1 Hz. PVDF was chosen for its favourable combination of cost and mechanical strength. Its main limitation is a relatively low energy conversion rate; electrostrictive polymers may offer higher conversion efficiency, but further research is required.

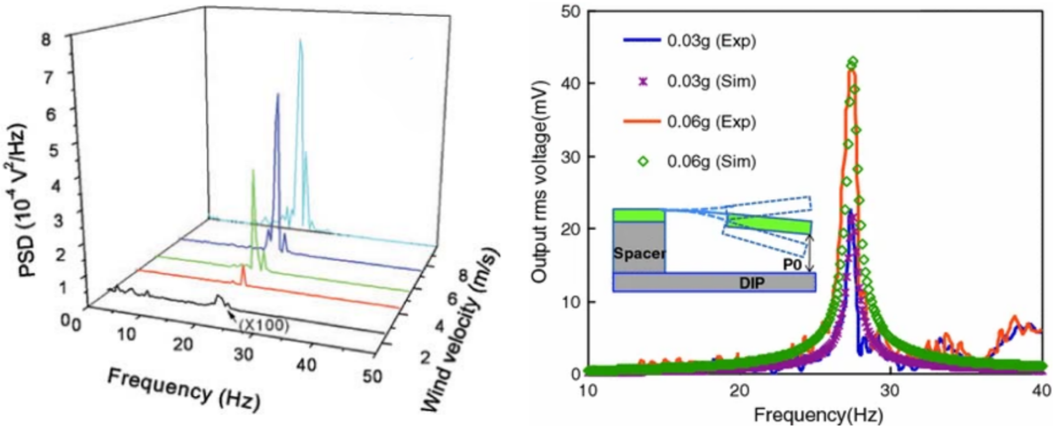

(a) (b)

Figure 2.24: Power spectral density of a PZT piezoelectric device with tip mass from X. Gao et al.[114] (a) and output voltage over frequency for an s-shaped PZT film on a beam with tip mass for varying acceleration speeds from H. Liu et al.[115] (b)

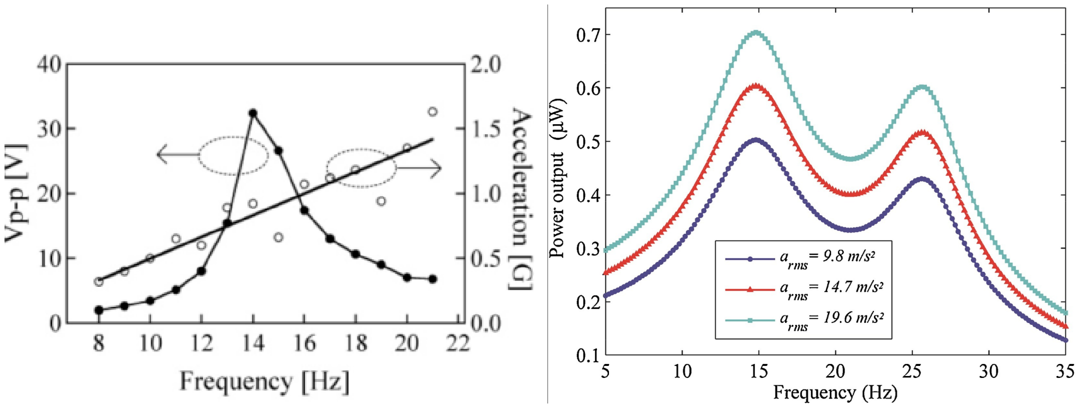

(a) (b)

Figure 2.25: Voltage output per frequency of a PVDF piezoelectric device with tip mass from Y. Jiang et al. [116] (a) and power output of a PVDF piezoelectric device with tip mass from S. Li et al. [117] (b)

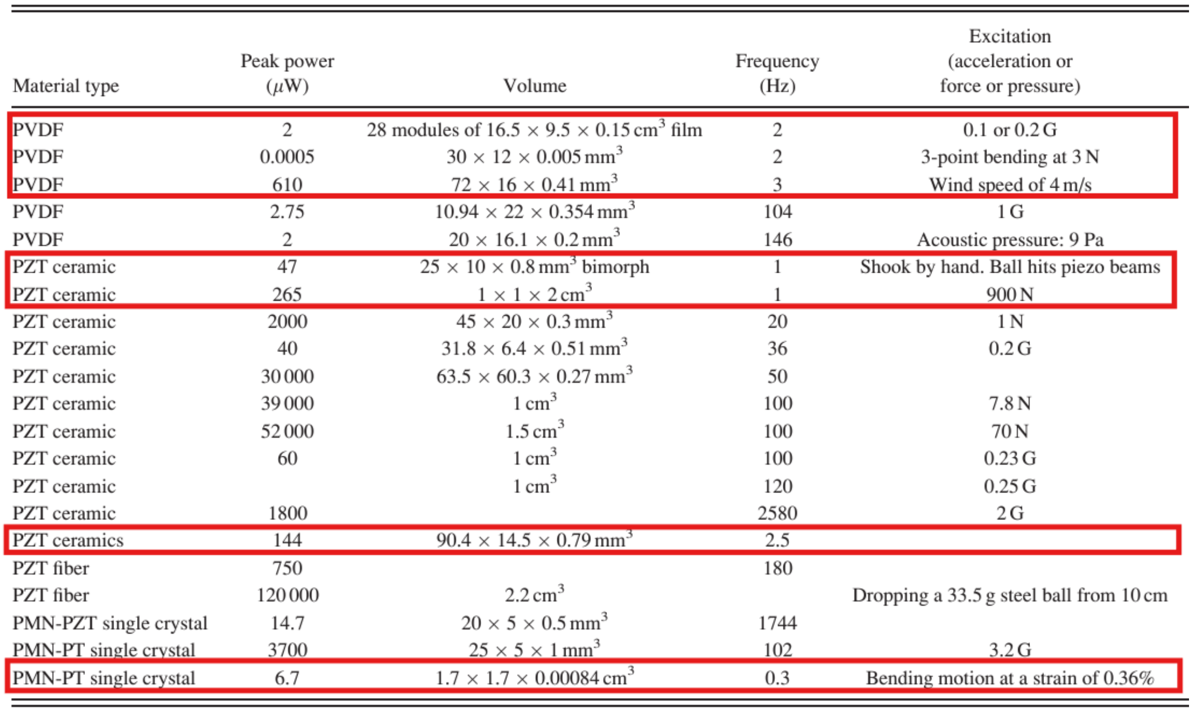

Material type	Peak power (μW)	Volume	Frequency (Hz)	Excitation (acceleration or force or pressure)
PVDF	2	28 modules of 16.5 × 9.5 × 0.15 cm^3 film	2	0.1 or 0.2 G
PVDF	0.0005	30 × 12 × 0.005 mm^3	2	3-point bending at 3 N
PVDF	610	72 × 16 × 0.41 mm^3	3	Wind speed of 4 m/s
PVDF	2.75	10.94 × 22 × 0.354 mm^3	104	1 G
PVDF	2	20 × 16.1 × 0.2 mm^3	146	Acoustic pressure: 9 Pa
PZT ceramic	47	25 × 10 × 0.8 mm^3 bimorph	1	Shook by hand. Ball hits piezo beams
PZT ceramic	265	1 × 1 × 2 cm^3	1	900 N
PZT ceramic	2000	45 × 20 × 0.3 mm^3	20	1 N
PZT ceramic	40	31.8 × 6.4 × 0.51 mm^3	36	0.2 G
PZT ceramic	30 000	63.5 × 60.3 × 0.27 mm^3	50	
PZT ceramic	39 000	1 cm^3	100	7.8 N
PZT ceramic	52 000	1.5 cm^3	100	70 N
PZT ceramic	60	1 cm^3	100	0.23 G
PZT ceramic		1 cm^3	120	0.25 G
PZT ceramic	1800		2580	2 G
PZT ceramics	144	90.4 × 14.5 × 0.79 mm^3	2.5	
PZT fiber	750		180	
PZT fiber	120 000	2.2 cm^3		Dropping a 33.5 g steel ball from 10 cm
PMN-PZT single crystal	14.7	20 × 5 × 0.5 mm^3	1744	
PMN-PT single crystal	3700	25 × 5 × 1 mm^3	102	3.2 G
PMN-PT single crystal	6.7	1.7 × 1.7 × 0.00084 cm^3	0.3	Bending motion at a strain of 0.36%

Figure 2.26: Overview of low-frequency piezoelectric applications and their performance H. Li et al. [112]

Determining the most suitable piezoelectric material is challenging due to the multiple factors involved. A key parameter is the energy output at low frequencies, but practical considerations such as commercial availability and emerging novel materials must also be taken into account. Polymers are particularly attractive due to their combination of high mechanical strength and potential for energy harvesting at low frequencies.

Within this material class, several options remain feasible, including electroactive polymers (EAP), which are relatively accessible for this project. Given sufficient availability and time, magnetoelectric composites may also be of interest, as they can harvest energy both from mechanical motion and magnetic fields. Considering that the underwater robot will operate in the presence of a magnetic field, such composites could offer an integrated advantage. These materials have been demonstrated to perform effectively at low frequencies [90].

Polymers such as PVDF are preferred for this project due to their mechanical flexibility, which suits the design requirement of a flexible underwater robot body. While ceramics like PZT provide higher energy conversion at the same strain, their brittleness makes them less suitable for low-frequency oscillatory applications in soft robotic structures. Importantly, the specific piezoelectric material ultimately selected for implementation will depend on commercial availability at the time of procurement. This ensures that the chosen material is both practically accessible and compatible with the robot's strain-based energy harvesting approach, combining adequate performance with ease of integration.

3

Design methodology

This chapter outlines the methodology used to develop the bio-inspired underwater robot, bridging the gap between the theoretical requirements defined in Chapter 2 and a practical, testable design. It explains how design decisions were systematically approached, considering both operational constraints and practical limitations such as material availability and project scope. By providing a clear framework for exploring alternatives, evaluating trade-offs, and iterating solutions, this chapter establishes the foundation for understanding why the final design takes its current form.

The relevance of this chapter lies in its role as the link between analysis and implementation: it demonstrates how abstract design requirements are translated into concrete design choices, and how these choices are validated through testing. In doing so, it sets the stage for subsequent sections, where the effectiveness of the design is evaluated and discussed. Overall, this chapter ensures that the design process is transparent, reproducible, and grounded in both engineering principles and practical considerations.

3.1. Design process

This chapter outlines the methodical design process followed for the bio-inspired underwater robot. While grounded in the standard frameworks of the Engineering Design Process [**sciencebuddies**] and the Delft Design Method [118], the steps have been adapted and integrated in a practical way to suit the constraints of this project. The chapter details how these approaches guided concept development, decision-making, and the iterative refinement of the final design.

The Engineering Design Process (EDP), as described by Science Buddies, provides a general and widely adopted framework for approaching engineering challenges. It begins with defining the problem and conducting background research to understand existing solutions, constraints, and relevant technologies. These initial steps form the basis for setting design requirements, which in this project were derived from the analysis presented in the previous chapter.

This chapter focuses on the subsequent phases of the process: building a prototype, testing, evaluating the results, and iterating the design as necessary. The methodology described here is based on standard concepts from the EDP and the Delft Design Method, but it has been integrated in a practically achievable way, tailored to the scope, resources, and constraints of this project. By documenting this methodical process, the rationale behind each design decision and adjustment is made transparent.

3.1.1. Design method

The design methodology applied in this project follows the Double Diamond model, a structured design framework consisting of two iterative cycles of divergence and convergence. In the first diamond, the focus lies on understanding and defining the problem, whereas the second diamond concentrates on developing and evaluating potential solutions. Within each diamond, diverging refers to exploring multiple directions without prematurely narrowing down options, while converging involves selecting, structuring, and refining the most promising paths based on explicit criteria [118, 119].

The Double Diamond framework (Figure 3.1 distinguishes four phases—Discover, Define, Develop, and Deliver. The first two phases form the problem-exploration diamond. The Discover phase aims to build a comprehensive understanding of the design context by gathering information, analysing existing solutions, and identifying underlying mechanisms relevant to bio-inspired underwater propulsion and energy harvesting.

The first diamond explores the problem space. By gathering information and expanding understanding (diverging), followed by structuring insights and defining a clear design challenge (converging), this phase ensures that the right problem is addressed. The second diamond focuses on the solution space. Here, potential solution directions are generated (diverging), after which one or several promising concepts are selected and developed further (converging). This iterative process supports the development of a well-founded and validated solution [119].

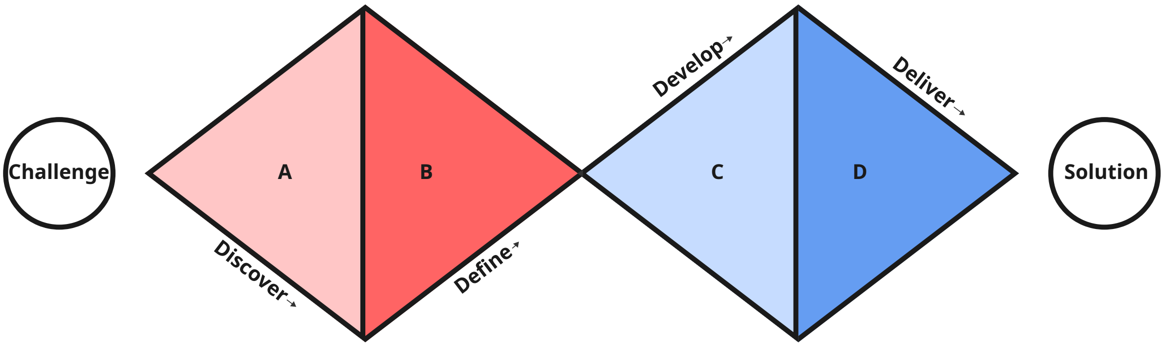

Figure 3.1: Double diamond design method [119]

Figure 3.2 shows how the Double Diamond methodology is applied within this project. The diagram links the main steps of the research to the diverging and converging phases of the model. It clarifies how the project moves from identifying the problem, through the literature-based analysis and requirement definition, to the development and testing of a prototype and the final evaluation of its performance.

The process begins with the Challenge, which identifies the fundamental problem motivating the research: current underwater monitoring vehicles suffer from low propulsive efficiency, high operational costs, and limited endurance. This challenge establishes the strategic motivation for exploring a bio-inspired alternative and functions as the anchor point for all follow-up

In the Discover phase, the project diverges by exploring multiple technological directions that could contribute to a more efficient underwater monitoring system. As shown in the figure, this exploration includes an examination of existing bio-inspired underwater vehicles, propulsion mechanisms, energy-harvesting strategies, and dual-mode operation concepts. The purpose of this stage is not to select a single solution, but to identify recurring principles, performance limitations, and functional relationships.

This broad exploration corresponds directly to the literature analysis, specifically, subsections 2.1.2, 2.2.2, and 2.3.1, survey and critically analyse a wide range of potential solution directions. These sections examine bio-inspired propulsion strategies, alternative energy harvesting mechanisms, and suitable electromechanical coupling principles, respectively. The Discover stage thereby expands the solution space and ensures that potentially viable approaches are not prematurely excluded.

The Define phase represents the converging stage of the first diamond, where the insights gathered during the Discover stage are synthesised into concrete design requirements and constraints. In the figure, this is represented by the block that focuses on specifying the necessary performance goals for a simplified bio-inspired system, including criteria for propulsive efficiency, energy-harvesting effectiveness, and material feasibility.

This phase translates the broad conceptual understanding from the Discover stage into actionable parameters and forms the methodological bridge between literature research and system development. The Define outcomes appear in subsections 2.1.1, 2.2.1, and 2.3.2, where hydrodynamic, energetic, and material constraints are formalised.

The transition to the second diamond begins with the Develop phase, where the project diverges again—this time not conceptually, but through iterative prototyping and practical experimentation. As indicated in the figure, this phase involves integrating a simple dual-mode system into an existing bio-inspired underwater vehicle and testing different configurations to create a functional combination of propulsion and energy harvesting.

This stage is documented in Chapter 4, where the theoretical requirements from the Define phase are translated into real physical prototypes. The Develop phase involves exploring multiple implementation choices, testing their performance, and refining the system based on observed behaviour. This mirrors the diverging–converging logic of the Double Diamond on a technical level: concepts evolve through cycles of trial, adjustment, and evaluation.

The Deliver phase represents the converging end of the second diamond. As shown in the figure, this phase focuses on interpreting test results, evaluating the feasibility of the implemented dual-mode system, and formulating future design requirements to enhance both propulsive and harvesting efficiency.

In this project, the Deliver phase appears in two forms: Its procedural execution—refinement, validation, and assessment—is reported in Chapter 4 and its final analytical output—the synthesis of results into a coherent design conclusion—is presented in Section 3.4.

By linking experimental findings back to the original challenge, the Deliver phase ensures that the project concludes with a grounded understanding of what the current prototype achieves and what future iterations must improve. The project challenge is introduced in Chapter 1. Chapter 2 addresses the Discover and Define stages, while Section 3.2 consolidates the outcomes of these stages into a clear design direction that bridges the initial research problem with the technical requirements identified through the literature.

The Develop phase—corresponding to the initial stage of the second diamond—is presented in Chapter 4. In this phase, the project expands once more into a divergent search for viable design implementations. Conceptual designs are transformed into physical and numerical prototypes, and alternative configurations are explored through iterative modelling, preliminary experiments, and early-stage testing. This phase emphasises idea generation, prototyping, and the exploration of practical feasibility based on the criteria established in the Define phase.

The Deliver phase finalises the development cycle by converging on solutions that demonstrate the highest technical potential. Refinements are made based on experimental results, and prototypes are evaluated against the established performance metrics. Ineffective approaches are discarded, while promising designs are further validated, documented, and prepared for final analysis. The Deliver phase thus ensures that the research culminates in a well-supported and experimentally grounded design solution.

While the Develop and Deliver phases are primarily executed in Chapter 4, the outcomes of these activities are interpreted and consolidated in the present chapter. Chapter 4 details the practical implementation of the Develop phase—where design concepts are transformed into functional prototypes and subjected to controlled testing—and subsequently documents the initial steps of the Deliver phase, including iterative refinement and performance assessment.

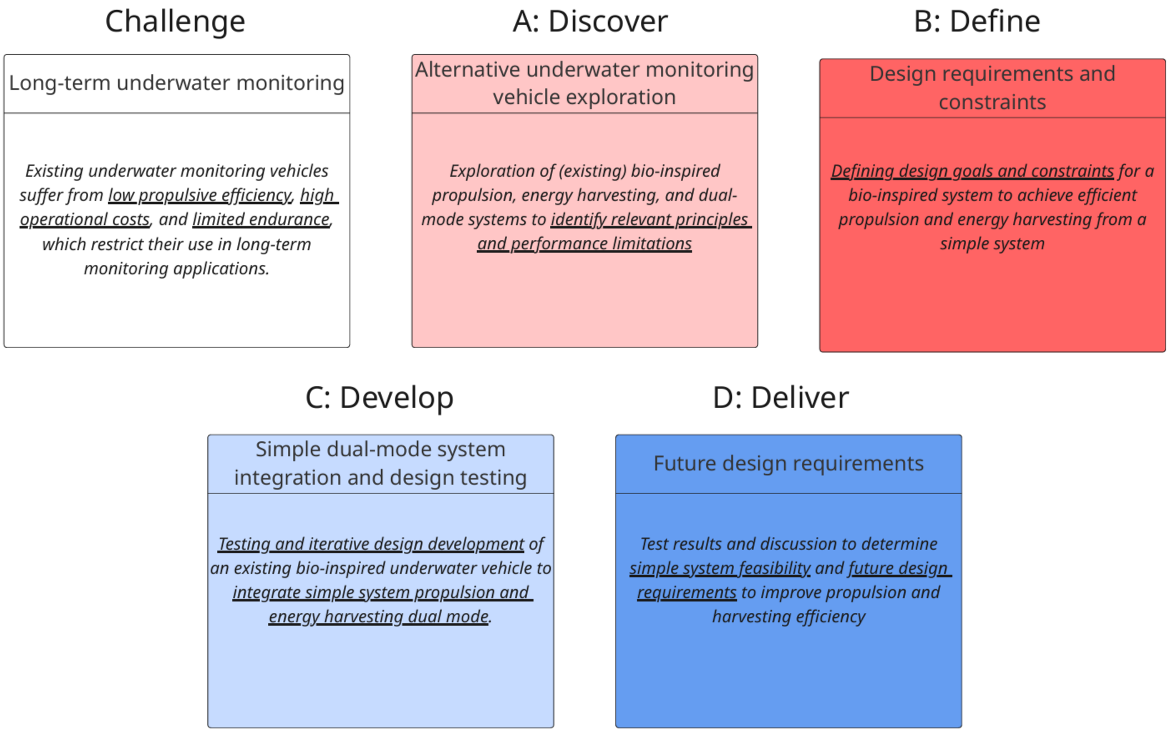

Existing underwater monitoring vehicles suffer from low propulsive efficiency, high operational costs, and limited endurance, which restrict their use in long-term monitoring applications.

Exploration of (existing) bio-inspired propulsion, energy harvesting, and dual-mode systems to identify relevant principles and performance limitations

Defining design goals and constraints for a bio-inspired system to achieve efficient propulsion and energy harvesting from a simple system

Testing and iterative design development of an existing bio-inspired underwater vehicle to integrate simple system propulsion and energy harvesting dual mode.

Test results and discussion to determine simple system feasibility and future design requirements to improve propulsion and harvesting efficiency

Figure 3.2: Double diamond design method details

The current chapter, in contrast, presents the overarching conclusions derived from these experiments. Here, the final evaluation of the prototype, the interpretation of test results, and the implications for the validated solution are synthesised. In this way, the Deliver phase is distributed across chapters: its methodological execution appears in Chapter 4, while the final analytical conclusions and reflection on solution viability are presented in section 3.4.

The Double Diamond framework provides the structural backbone of this project by guiding the transition from conceptual understanding to a validated prototype. The Discover and Define phases systematically map the technological landscape and translate observations into explicit design parameters. The Develop phase uses these parameters to construct and test physical and numerical prototypes, while the Deliver phase evaluates the outcomes and consolidates the final design insights. This structured and iterative approach ensures that the final solution is both technically substantiated and directly aligned with the initial problem statement.

3.1.2. Design decision checkpoints

This subsection provides an explanation of the design decision checkpoints applied throughout the development trajectory, in which the Develop and Deliver phases of the design diamond are systematically elaborated. The constructed flow chart outlines how the design process, the testing process, and their iterative steps interact and structure the overall workflow. It further clarifies at which moments, and based on which criteria, decisions were made to proceed to the next phase or to return to an earlier stage to refine the design or test setup. In doing so, this subsection illustrates how successive iterations contributed to the final design outcome.

The flowchart presented in Figure 3.3 provides a summary of the design, development, and testing phases, culminating in the final design. There are two starting points: firstly, the original design by S. C. van den Berg et al. [65], and secondly, the piezoelectric film. These serve as the initial bases for the structural design and the dual-mode system design, respectively.

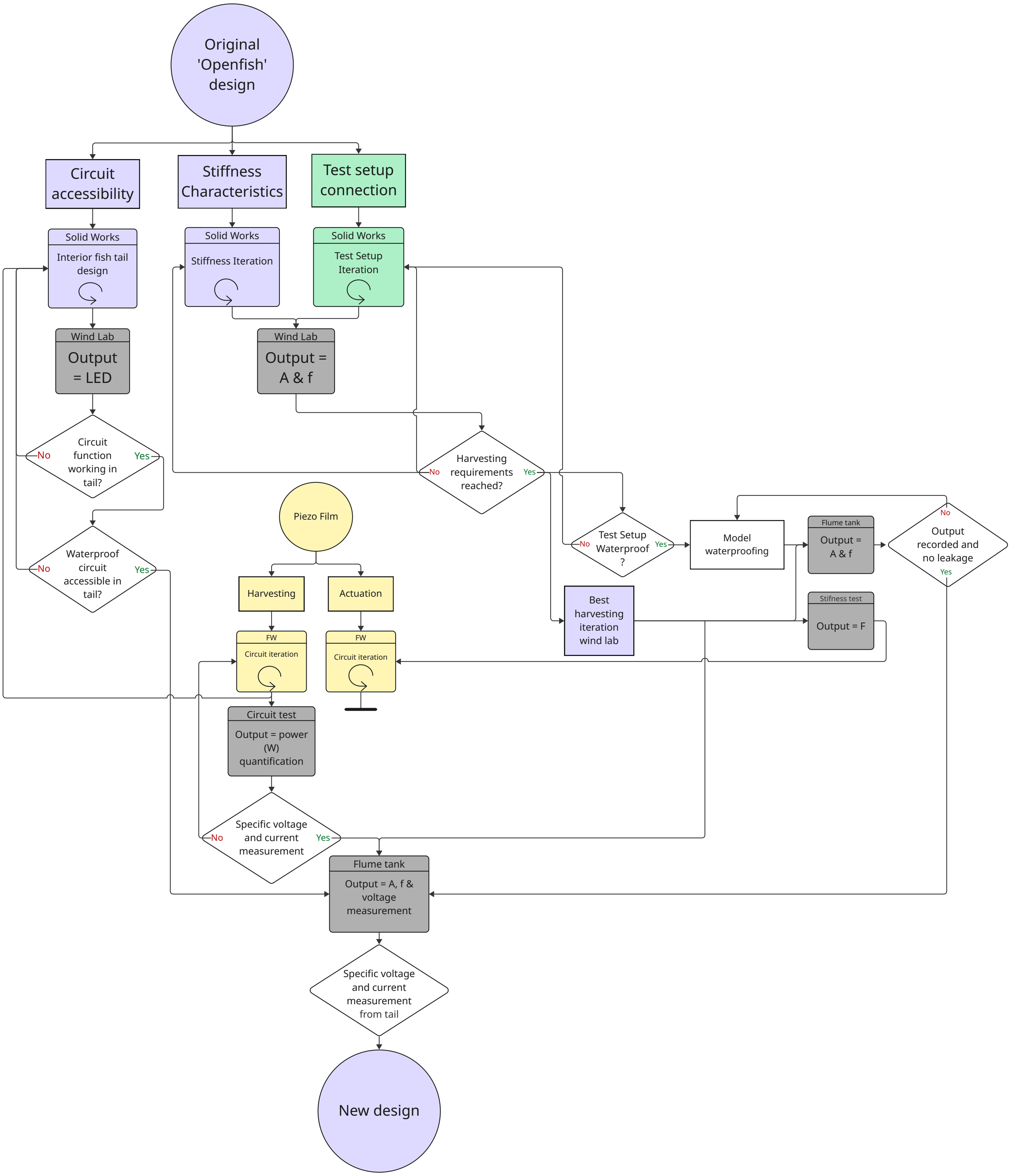

Figure 3.3: Specific design method

The flowchart illustrates two primary design directions and their connection to the test setup. These design directions—circuit accessibility and stiffness characteristics—serve as the main drivers of design modifications throughout the project. Other possible design change directions have been considered outside of the scope of the project due to time constraints. Simultaneously, the development of the test setup plays a critical role, as it directly impacts the reliability and interpretation of experimental results. Together, these elements define the iterative nature of the design and testing process.

Design adjustments were necessary to ensure proper access to the circuit, as the original configuration could not accommodate it. The original electromotor, which pulled a string on either side, was entirely replaced by the piezoelectric circuit, requiring a reconfiguration of the entire system. Because the circuit was developed concurrently, the system layout changed continuously, and the design had to be updated accordingly.

The stiffness characteristics were a primary focus of the design modifications, as they strongly influence piezoelectric bending during energy harvesting, the angle of attack, flapping frequency, and the force required to actuate the underwater robot. Therefore, the stiffness properties were carefully analysed and iteratively adjusted throughout the project to optimise overall performance.

The test setup is essential because it can significantly affect measurement accuracy and result reliability. Accurately measuring the deflection angle without a complex camera or prototype setup, while minimising interference with the tail's flapping behaviour, is challenging. Multiple setups were employed for different types of tests and environments, making the design of the test setup a fundamental component of both the design and evaluation processes.

To address circuit accessibility, the stiffness characteristics of the tail, and the requirements of the test setup, the designs and design modifications were developed in SolidWorks. Since the design files of the original system were provided in SolidWorks format, continuing development in this software was the most practical approach. The designs could only be tested once the test setup was operational, with the first stage of testing conducted in the wind laboratory.

The parameters measured in the wind lab were the flapping characteristics of the tail—specifically amplitude (A) and frequency (f)—as well as the functionality of the piezoelectric circuit. To measure this, an LED is used as a visual indicator of whether the circuit is working. Although these measurements can be performed simultaneously, the development of the circuit and the wind lab experiments occurred in parallel. As a result, the tests were carried out separately.

The purpose of these tests is described in Section 3.3. Once the circuit was shown to function within the tail, the waterproof version of the circuit—which differs slightly from the wind lab version—also needed to be accessible. This requirement led to additional modifications of both the design and the test setup to ensure that the waterproof circuit could be integrated properly. The differences between the two circuit versions are explained in subsection 4.3.1.

The flapping characteristics were tested for multiple stiffness configurations. According to the flapping requirements outlined in subsection 2.2.1, an angle of attack between 30° and 40° yields the highest harvesting efficiency. This range was not achieved after further iterations. However, due to the constraints associated with the flume tank, the stiffnesses that demonstrated the best performance in the wind lab were selected for the next testing phase: the underwater experiments.

The stiffness configurations that performed best in the wind lab were selected for the subsequent tests: the stiffness test and the flume tank experiments. To conduct the flume tank tests, both the model and the test setup must be fully waterproof. The differences between the model and test setups used in the wind lab and those used in the flume tank are discussed in Sections 3.3, 4.1.1, and 4.2.1. The measurements obtained in the flume tank are identical to those collected in the wind lab, namely the flapping amplitude (A) and frequency (f). Maintaining waterproof conditions throughout the tests is essential, as the presence of water inside the tail would alter its stiffness characteristics. Additionally, the setup must prevent water intrusion to ensure that the circuit remains dry during the underwater circuit tests. In this sense, the flume tank tests serve as a practical trial for the subsequent underwater circuit test.

The stiffness test is a relatively straightforward dry test designed to determine the force required to bend the tail by at least 10°. This information is necessary for evaluating and designing the actuation mechanism. This test is performed only with the chosen optimal stiffnesses.

If the waterproof circuit fits in the model and testsetup and all previous tests have been performed the circuit can be tested underwater. This test is the most important test and requires all components to function together. This means that the underwater circuit must give an measureable output in Watts and the testsetup and model are fully waterproof and funcitonal.

The second starting point, the piezoelectric film is the starting point fo the circuit development. This development was parallel with the design and test setup developmetn. The piezoelectric circuit has been divided into two modes for simplicity. The harvesting and the actuation mode. The harvesting mode has been tested more extensively due to available materials.

The iterations of the harvesting circuit are discussed in subsection 4.3.1. The circuit and the output of the power-measuring device were tested prior to integration into the model to verify that they functioned as expected. Once validated, the circuit was incorporated into the test setup and subsequently tested underwater. This underwater test was performed only once, using the stiffness configuration that showed the best performance in the flume tank tests in terms of flapping amplitude (A) and frequency (f). The actuation circuit, discussed in subsection 4.5.1, has not been experimentally tested; however, predictive calculations have been carried out and are presented in subsection 4.5.2.

The circuit development process follows a trajectory from qualitative to quantitative data. Initially, the circuit is tested using empirical signals and low-accuracy inputs, after which testing progresses toward controlled measurements with defined uncertainties. Through this iterative approach, the circuit is gradually improved to ensure predictable output and to achieve a comprehensive understanding of its capabilities and limitations.

The design and development trajectory presented in this subsection illustrates how a structured, iterative methodology enabled the systematic integration of mechanical design changes, circuit development, and experimental validation. By anchoring each design decision to clearly defined checkpoints, the process ensured that only evidence-based modifications advanced to subsequent phases. The parallel progression of circuit and structural development required continuous methodological reflection, reinforcing the importance of iteration as a guiding principle. Ultimately, this approach demonstrates how the applied methodology—characterised by iterative testing, feedback-driven refinement, and phased decision-making—served not only to shape the final prototype, but also to structure and validate the entire development process itself.

3.2. Design approach

In this chapter, the foundational principles guiding the design process are outlined. The design approach is built upon the insights, requirements, and theoretical considerations established in Chapter 2, which collectively define the operational context and performance expectations of the system. These elements serve as the basis for translating conceptual understanding into concrete design objectives.

In addition to these conceptual foundations, practical limitations are incorporated to ensure that the design remains feasible within the constraints of available materials, manufacturing options, testing facilities, and project duration. Together, the operational requirements and practical constraints shape the design goal and determine the boundaries within which the final design must be developed.

3.2.1. Operational design requirements

The operational requirements of the underwater robot are broadly introduced in Chapter 1. These requirements specify that the robot must be capable of functioning in both a propulsion mode and an energy-harvesting mode. The propulsion mode must be bio-inspired and may not involve propellers or similar conventional mechanisms. Bio-inspired propulsion, as defined here, does not include wave-propelled systems—i.e., systems that use ambient wave motion as their primary source of forward movement, such as the glider developed by Y. Zhang et al. [83]. Such systems operate fundamentally differently, as they rely directly on environmental forcing rather than on an internal energy storage and conversion system, and are therefore outside the intended scope of this design.

The harvesting system should employ the same (bio-inspired) mechanism as the propulsion system, and vice versa. Although many different energy-harvesting approaches exist, using a single integrated system for both modes offers the greatest potential for achieving a highly efficient, simple, and environmentally unobtrusive underwater robot. When separate systems are introduced—for example, by attaching a turbine-based harvester—the design becomes inherently more complex, requires additional moving parts, and increases hydrodynamic drag during swimming. Moreover, such additions contradict the intention to minimise environmental influence, as external harvesting devices disturb the flow field and alter the robot's interaction with its surroundings.

By ensuring that propulsion and harvesting rely on the same mechanism, the system can remain lightweight, mechanically simple, and energetically efficient, while maintaining the bio-inspired character of the design. This integrated approach, therefore aligns most strongly with the overarching goal of developing a low-complexity, energy-efficient underwater robot with minimal environmental impact.

The same system refers to the movement underlying both the propulsion and energy-harvesting modes. Specifically, the tail-flapping motion serves as the critical component for generating forward thrust and harvesting energy from the flow. While the internal mechanism responsible for inducing tail motion or converting mechanical movement is not strictly limited to a single configuration, the primary objective is to develop the simplest possible system that effectively combines both functions.

As mentioned in Chapter 1 and subsection 2.2.2, a simple actuation and harvesting system carries a lower risk of maintenance issues, energy losses, and structural or manufacturing complications, making it a more feasible solution overall. Additionally, designing a complex and intricate actuation and harvesting system requires specialised expertise in electrical systems. This level of expertise was not available within the scope of the present project, whereas knowledge in mechanical systems, fluid dynamics, and ecological aspects—rooted in ocean engineering and ocean sciences—was accessible. While design processes often benefit from multidisciplinary integration involving researchers and practitioners from multiple fields, this is not always feasible in practice [120]. This is why a single system for both actuation and energy harvesting is applied in this design.

The harvesting and propulsion modes do not occur simultaneously; they represent distinct operational states. The propulsion mode is active during swimming, while the energy-harvesting mode is engaged when the underwater robot is attached to a fixed structure, eliminating the need for station-keeping, and the tail is driven by the ambient current. Depending on the sensors and monitoring systems integrated within the underwater robot, data collection may be possible in both operational modes.

Both modes are aimed to operate as efficiently as possible. To ensure this, the specific operational design requirements are determined in subsections 2.1.1, 2.2.1, and 2.3.2. These parameters are based on the literature of previous research. The most important parameters in this research are presented in Figure 3.4.

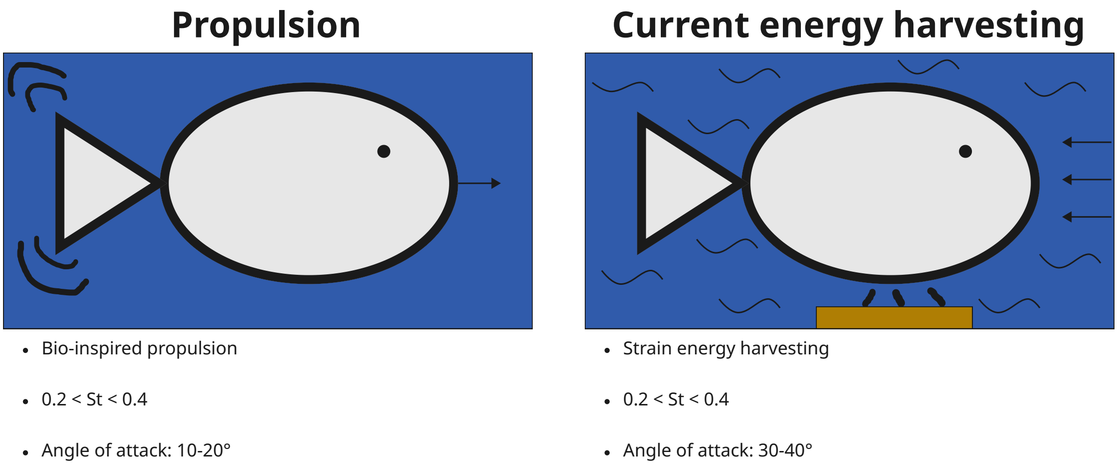

Figure 3.4: Basic design requirements

This figure illustrates the two operational modes. In the propulsion mode, the underwater robot (simplified here as a grey fish) generates forward motion through an undulating tail movement. In the energy-harvesting mode, the robot is attached to a fixed structure, and the tail is driven by the ambient current. The resulting current-induced oscillations enable the system to harvest energy from the flow.

Beneath each mode, three core performance requirements are defined. The top point is a hard requirement, the second two are requirements which may be reached at later stages. For the propulsion mode, the motion must be bio-inspired, and the relationship between tail-flapping frequency and forward velocity should fall within the optimal Strouhal range. Additionally, the angle of attack should remain between 10° and 20°. For the current-energy-harvesting mode, the energy must be extracted through strain-based harvesting, as established in subsection 2.2.2. In this mode, the Strouhal number should again lie within the optimal range, while the angle of attack should fall between 30° and 40°.

These are efficiency-oriented guidelines that frame the design process. They are not strict constraints and may be refined in future research; however, they play an important role in directing design iterations and determining which parameters should be prioritised during experimental validation. By providing an early indication of whether a design is likely to operate efficiently, these requirements help reduce unnecessary testing and analysis, thereby focusing the research effort on configurations with the highest potential for effective propulsion and energy harvesting.

Taken together, the operational design requirements establish the foundational goals upon which the underwater robot must be developed: the propulsion must be bio-inspired, the same tail-flapping mechanism must serve both propulsion and energy harvesting, and all subsystems must support this integrated approach. These core objectives ensure that the robot remains mechanically simple, efficient, and environmentally unobtrusive, while maintaining fidelity to biologically inspired motion principles. The associated performance parameters—such as the optimal Strouhal range and angle-of-attack limits serve as practical design guidelines that shape each stage of the development process.

3.2.2. Practical design limitations

In addition to the operational requirements that define what the underwater robot must achieve, the design process is inherently shaped by several practical limitations that influence how these requirements can be realised. These limitations arise both from the physical and material constraints associated with constructing a functional prototype and from the boundary conditions imposed by the intended operational environment. Factors such as material availability, manufacturability, laboratory capabilities/availability, and the overall development timeframe restrict the range of feasible design choices. Similarly, the environmental conditions in which the underwater robot must operate further narrow the design space. Recognising these practical limitations is essential, as they directly affect the complexity, reliability, and scalability of the final design.

The size of the underwater robot is not intended to increase significantly. Therefore, an important constraint to consider is the size of the circuit. The available space in the body of the underwater robot is sufficient to house a small electromotor. Additionally, the weight of the circuit also cannot exceed the original weight of the electromotor significantly. A piezoelectric circuit is not complex; however, to actuate such an element, a voltage amplifier is necessary. Voltage amplifiers come in a large range of weights, sizes and prices. Small voltage amplifiers typically reach 900 Volts, whereas large amplifiers can go up to 10K Volts. This is a big difference in output as well as application. The underwater robot cannot house large voltage amplifiers and therefore, the voltage requirement of the piezoelectric film is limited.

During the energy harvesting mode, the underwater robot will be near a wall. This limits the size of the caudal fin. From the literature, it has been evident that a high aspect ratio may improve swimming speed (eq: 2.3). However, similar to fish species which graze from the bottom for example, this would not fit. Therefore, the height of the caudal fin is limited at least to one side. For harvesting purposes, it would be possible to have an asymmetrical fin, but the propulsion characteristics of such a fin are not well known. From the original design, it has already been proven that a larger caudal fin has a higher propulsive efficiency than a lower fin [65]. Therefore, the original caudal fin configuration remains unchanged.

3.3. Testing rationale

To systematically evaluate the performance of the underwater robot and verify whether the design meets the defined operational requirements, experimental testing is essential. Testing provides insight into the hydrodynamic, structural, and electromechanical behaviour of the system, allowing key efficiency characteristics to be quantified under controlled conditions. Moreover, well-structured experiments enable goal-oriented design refinement by revealing how specific design choices influence propulsion and energy-harvesting performance.

This section outlines the rationale behind the selected test procedures, explaining why each experiment was carried out and what specific design questions it addresses. By linking each test to a clearly defined objective, the testing strategy ensures that experimental efforts directly support the iterative development of a robust and efficient underwater robot before exposure to real environmental conditions.

3.3.1. Testing objectives

Testing requires time, laboratory access, and dedicated experimental setups; therefore, clearly defined testing objectives are essential. These objectives guide the overall testing process by specifying what must be evaluated, under which conditions, and with what level of accuracy. Establishing explicit objectives ensures that each test is purposeful, methodologically sound, and aligned with the broader design goals.

In this subsection, the testing process is first outlined from a methodological perspective, followed by a specification of the key questions and requirements that the tests are intended to address. The subsequent subsection then discusses the final selection of testing methods applied in this research.

Testing is initiated whenever a design question arises that cannot be answered through analysis alone. Such questions must be addressed to determine the operational performance of the design and are directly linked to the overarching research question. In this project, the design questions primarily focus on practical actuation parameters, energy-harvesting performance, and efficiency metrics.

Each design question corresponds to specific parameters that must be measured. The main parameters evaluated in this study are tail-flapping amplitude and frequency, generated power, and the force required for tail actuation. Appropriate materials and measurement equipment are employed to accurately capture these parameters. After testing, both the performance of the experimental setup and measuring instruments, as well as the functionality of the prototype, are evaluated to determine whether any design modifications are required.

This process is illustrated in Figure 3.5. The stiffness test does not necessitate design modifications and has no subsequent test, and is therefore positioned on the right. In contrast, the dry wind-lab and circuit tests do require design changes. Due to time constraints, the flume tank test serves as the final evaluation, determining the energy-harvesting performance based on both the tail's flapping behaviour and the power output of the piezoelectric film when the model is exposed to flow.

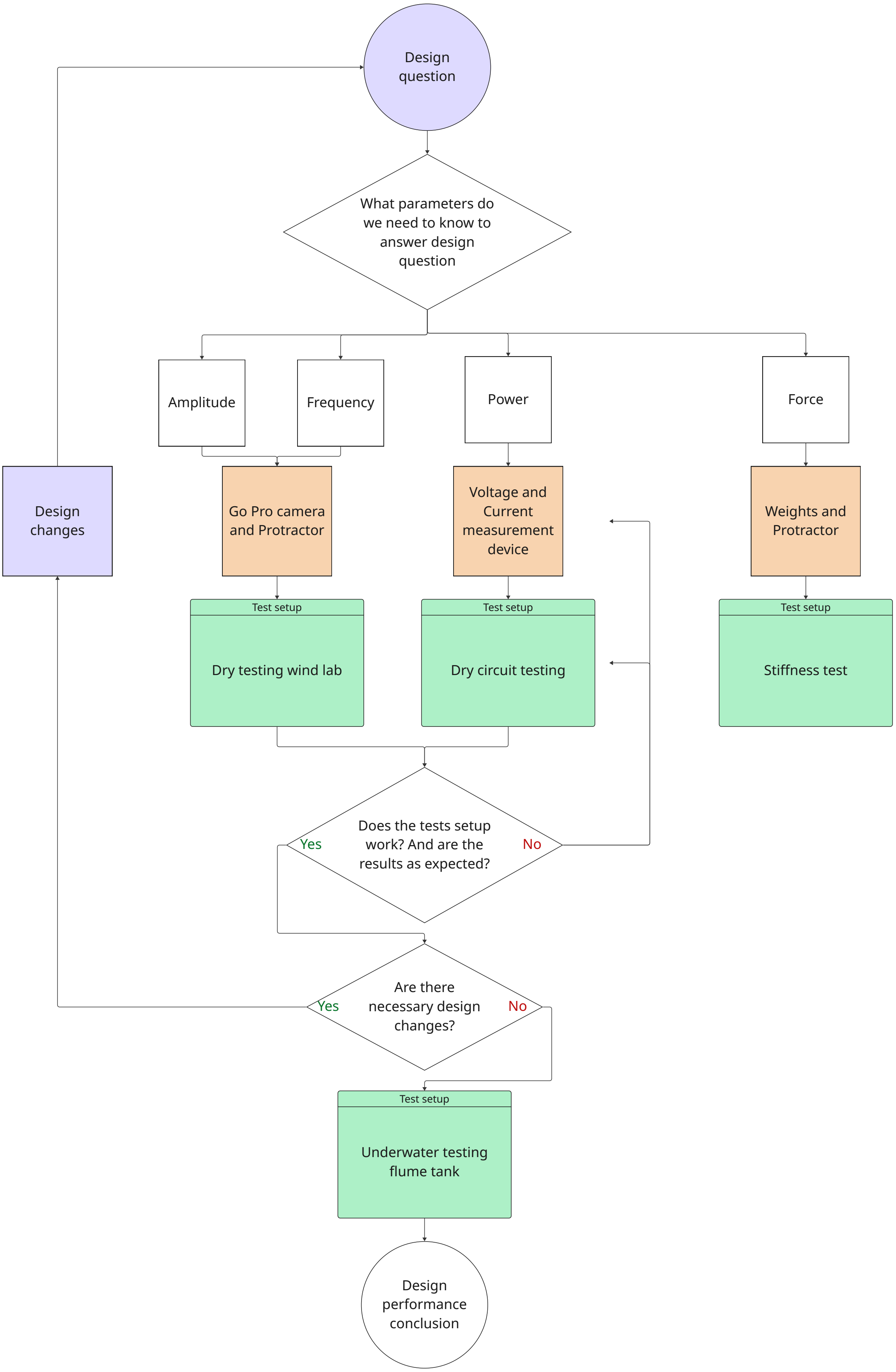

Figure 3.5: Specific testing process

During this project, 5 different tests have been performed. Each test has a specific design question that it needs to answer. These design questions are:

- What backbone stiffness has the highest energy harvesting efficiency when subjected to flow?
- How strong should the piezoelectric film be to flap the tail at least 10°?
- How much power (W) does the flapping motion of the tail harvest when subjected to flow?

These questions have been split up in sub-questions which directly relate to the specific parameters that need to be measured or determined (Figure 3.6). The answer to the design questions can be directly concluded from the results.

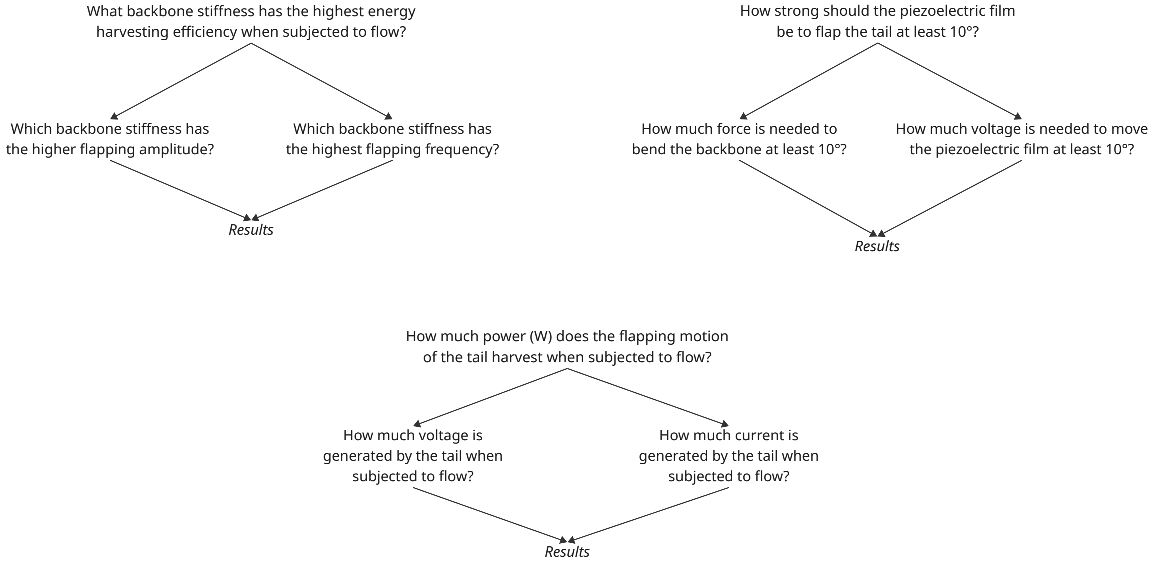

Figure 3.6: Specific design questions

The testing objectives establish a structured framework that links each experimental activity to a clearly defined design question, the corresponding measurable parameters, and the methodological requirements necessary to obtain reliable results. By explicitly formulating these objectives, the testing process becomes both systematic and traceable, ensuring that every experiment contributes directly to the evaluation and improvement of the underwater robot's performance.

3.3.2. Selection of testing methods

Multiple approaches exist for conducting each test and measuring the relevant parameters. This subsection outlines the rationale behind the selection of the specific testing methods used in this project. The choices are motivated not only by methodological considerations—such as measurement reliability and experimental validity—but also by practical factors including laboratory accessibility, available materials, and time constraints. Together, these considerations justify why particular methods were selected over alternative options.

Any design question that involves a system being “subjected to flow” requires testing under flowing conditions. Ultimately, the relevant medium for this underwater robot is seawater. To generate flow around an object, two approaches are possible: either the object can be moved through the medium at a specified velocity, or the medium itself can be driven past the stationary object. The available facilities support both approaches, and comparable results would be expected from either method [121].

For practical reasons, the flapping characteristics were first tested in air before introducing water. Directly initiating experiments in water carries a higher risk of damaging the model or the facility due to unforeseen issues, and it introduces additional complexity at an early stage of the testing process.

Air, therefore, served as the primary medium during initial testing. However, to approximate underwater conditions, relatively high flow velocities are required. Moving the model through the air at such speeds is both technically challenging and potentially hazardous, making this approach impractical. Consequently, the wind laboratory was selected as the primary testing facility.

The flume tank was chosen over the towing tank, so the concept of the test setup could remain the same as for the wind lab. Additionally, the towing tank may have added turbulence due to the friction of the rails [121]. Having the model stationary is also the easiest and most reliable way to measure the amplitude in degrees.

The stiffness test is performed with the fewest possible measurement devices. The use of gravity is a reliable way to measure force, and therefore, this method was not overcomplicated.

3.4. Final design

This section focuses on the key design changes implemented throughout the project, explaining why they were necessary and how they emerged. It traces the evolution of the system from the initial concept to the final configuration, highlighting the iterative process through which each modification was identified, tested, and refined. By examining these changes, this section illustrates the decisions and trade-offs that shaped the final design, as well as the factors that influenced its development. The final design thus not only represents the project outcome but also provides insight into the rationale and process behind each adaptation.

3.4.1. Design changes

The design changes presented in this subsection illustrate the iterative process and the rationale behind each decision, as well as any specific design constraints that were maintained. These changes are guided by the requirements outlined in Section 3.2. Since the design is specifically tailored for efficient propulsion [65], parameters influencing the propulsion motion were kept to a minimum. Nevertheless, modifications to some of these parameters were unavoidable in pursuit of the energy harvesting objectives. This subsection addresses changes related to circuit accessibility, stiffness, and overall practical considerations.

Figure 3.7 illustrates the first and most fundamental changes made to the original design. It presents both the external view of the original design and the original cross-sectional layout (Figure 3.7a), as well as the components that were removed or retained (Figure 3.7b).

The external structure of the design (hull) has remained unchanged. No modifications were made to this part. It should be noted, however, that during testing, the fins on the rigid section (orange) of the robot were not installed to simplify adjustments to the test setup.

In contrast, the interior design underwent several modifications. The backbone in the soft section of the tail was replaced with silicone, reducing stiffness in the distal part of the tail. This adjustment ensures that the backbone does not interfere with the stiffness of the so-called active part, which is the portion of the tail that moves through actuation between the ribs. In the original design, the backbone influenced actuation primarily at the last rib. With the alternative actuation system, movement is distributed across all ribs, reducing the pivot effect at the final rib. Furthermore, retaining the backbone would have required multiple tail cover configurations, increasing testing complexity, construction time, and material use. It should be emphasised that the removal of the backbone is not considered a permanent change.

The removal of the gearbox assembly is the most important one. This is the driving part of the original actuation system. However, in subsection 2.2.2 it is decided not to apply rotational actuation or energy harvesting systems, including electromotors. Therefore, this part of the design is removed. The design of the replacement system is discussed in sections 4.3.1 and 4.5.1.

So the changes made in Figure 3.7b are the removal of the original backbone. Now the backbone only consists of the component holding the ribs together, which, in essence, extends half as far as the original design, namely, not beyond the last rib. Placed on the backbone is the piezoelectric film. More information of piezoelectric film placement is given in section **??**. The location and function of the ribs does not change; however, the design of the ribs itself has changed. This will be discussed later in this subsection. Lastly, the gearbox assembly is removed and replaced by the piezoelectric circuit including batteries, and voltage amplifier.

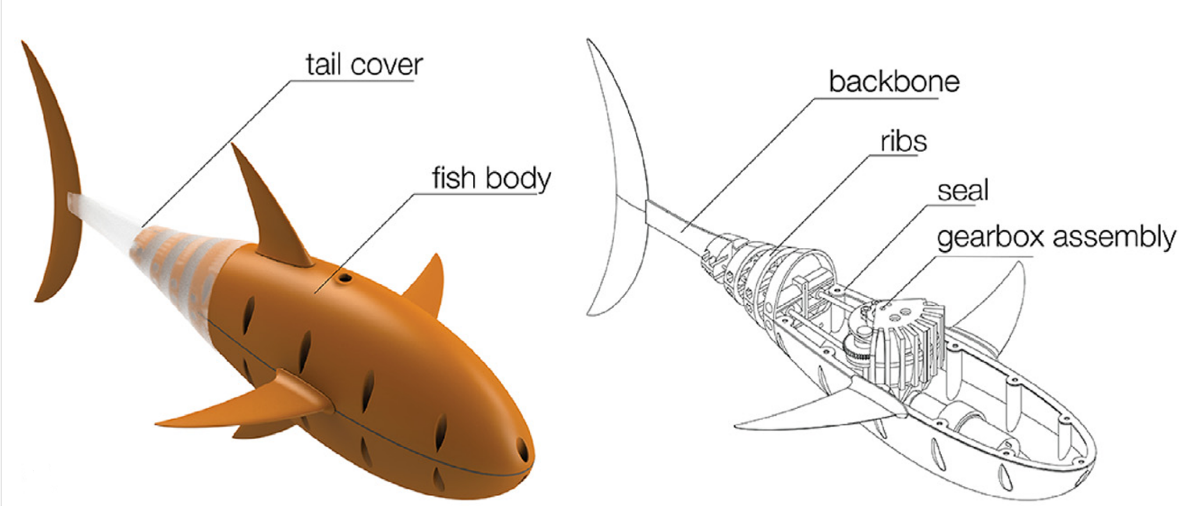

(a) Original design by S. C. van den Berg et al.[65]

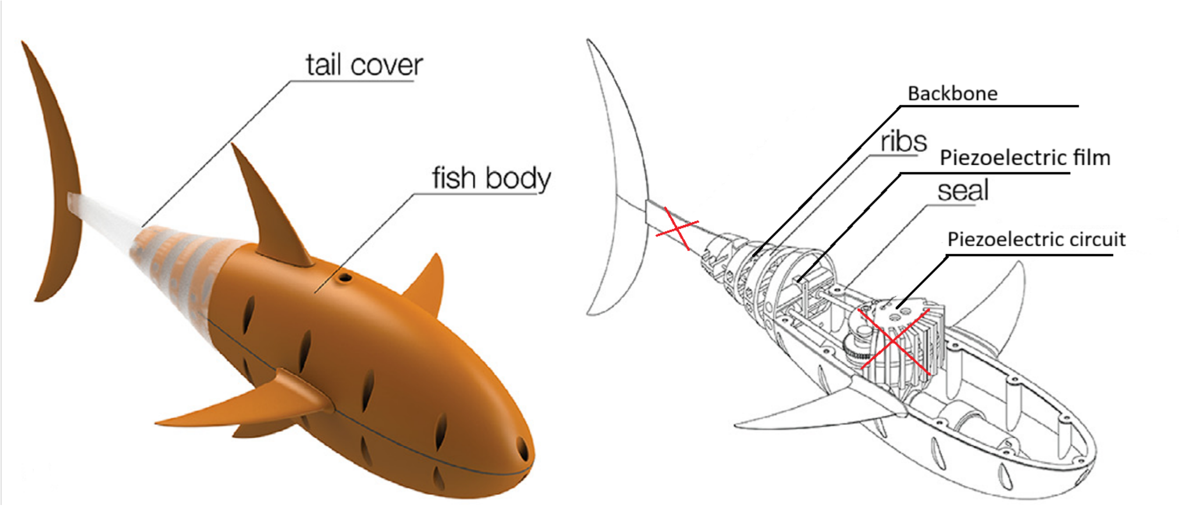

(b) General design changes

Figure 3.7: Overview of the general design changes

The base corresponds to the first rib, which connects the tail of the underwater robot to the body and, in this project, also to the test setup. To accommodate the piezoelectric film and circuit within the tail, the slit in the base was widened. This modification allows the wires, connector, and backbone to fit properly without obstruction. As a consequence of the widened slit, the connection between the backbone and the base was altered. In this configuration, the backbone performs best when clamped, as this prevents unintended movement. Although this affects the stiffness characteristics of the tail, it avoids the risk of the backbone oscillating within the slit, which could damage the wires, connector, or surrounding components.

This modification to the base was necessary to ensure circuit accessibility. Alternative solutions—such as creating additional openings for the wires—were considered, but these introduced the risk of the backbone and connector moving independently if not directly secured. Attaching the circuit to moving components could also influence the tail's stiffness or bending behaviour. For these reasons, the clamped configuration was adopted during testing, as it required minimal changes to the original design, the test setup, and the circuit.

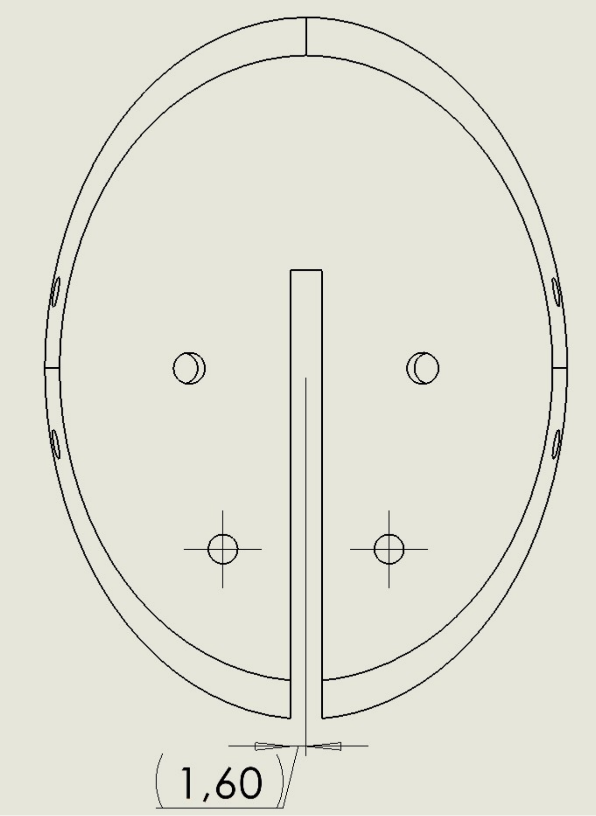

Figure 3.8: Thickness change in the first rib of 0.8 to allow for piezoelectric circuit

The specific changes to the backbone are presented in Figure 3.9. The left part of the backbone, which would normally be incorporated into the passive section of the silicone tail cover, has been removed. The right side is made structurally stable through the shape provided by S. C. van den Berg et al. [65]. Although this part was not used in their prototype, it is included in the design files. The screw holes have been removed to accommodate the piezoelectric film. While these holes were useful in the original design, the clamped configuration no longer requires connection points at the base. Similarly, the modifications in the middle rib do not require connection holes, and the holes in the final rib have been removed to make space for the piezoelectric film. The film is sufficiently thin to fit between the slit of the last rib and the backbone. During bending, the piezoelectric film may move deeper into the slit than the backbone. To prevent interference between the hole positions and the bending motion of both the film and the backbone, these holes were removed and replaced by a clamped configuration. The length and width of the backbone have been kept unchanged.

The stiffness of the tail's flapping motion depends on both the stiffness of the backbone and that of the silicone tail cover. The backbone is 3D-printed from PETG, a relatively flexible material, and therefore plays an important role in determining the overall stiffness. Consequently, the most relevant stiffness variable in this study is the backbone thickness. Adjusting the thickness directly changes the stiffness of the backbone and, therefore, the overall stiffness of the tail. The original thickness is 1 mm, and the thicknesses tested are 0.3, 0.5, 0.6, 0.8, 1.0, and 1.2 mm.

These backbone thicknesses were selected for two main reasons. First, the clamped configuration is expected to slightly increase the stiffness. Second, an increased stiffness requires a higher actuation force from the piezoelectric film. For this reason, thicknesses lower than the original were selected, with only one configuration thicker than the original. The thicker backbone was included because, as described in subsection 2.2.1, stiffer flapping foils exhibit higher energy harvesting efficiency. Therefore, the testing primarily focused on lower stiffness values, with one slightly higher value included.

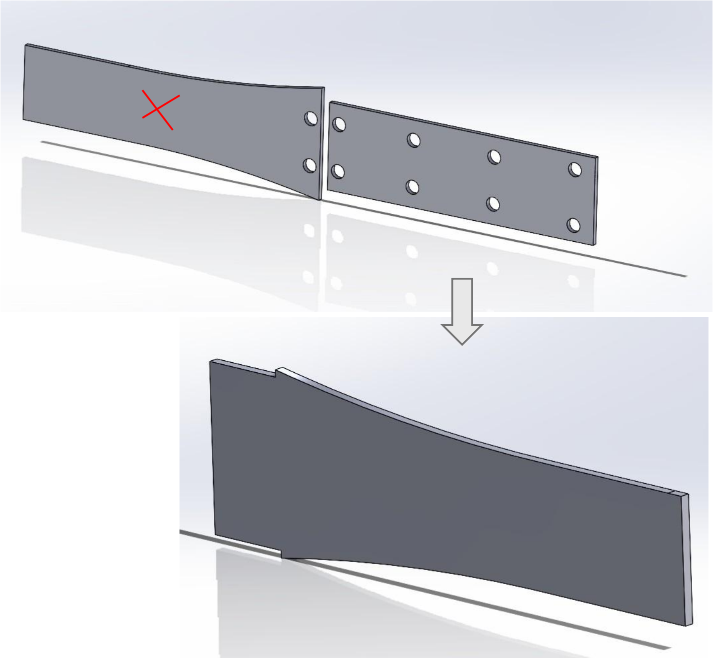

Figure 3.9: Backbone changes

The original middle ribs are directly connected to the backbone in the initial design, where they served to support the string on each side. With the removal of the string–electromotor configuration, this direct connection is no longer required. However, the middle ribs cannot be omitted from the design, as they are essential for maintaining the shape of the soft part of the tail.

The original slit may have been wide enough to accommodate both the backbone and the piezoelectric film, but it could obstruct the bending of the film and does not allow for increased thickness of the piezoelectric components. Therefore, the structurally necessary outer geometry of the ribs has been retained, while the internal material has been removed to create sufficient space for the piezoelectric film. The changes have been presented in Figures 3.10a and 3.10b.

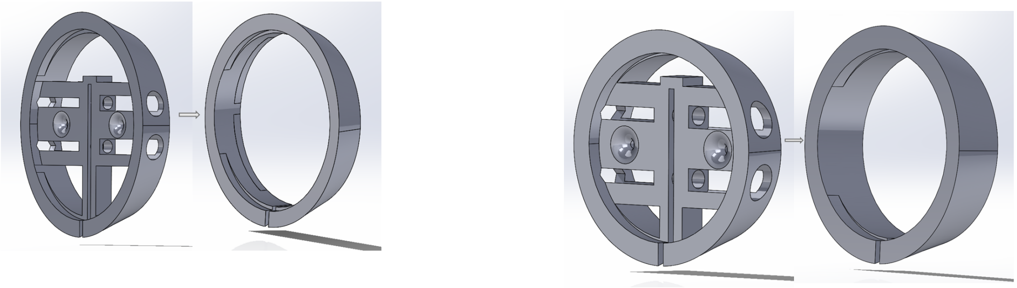

(a) Design changes made to part 7 from S. C. van den Berg et al.[65] **(b)** Design changes made to part 8 from S. C. van den Berg et al.[65]

Figure 3.10: Design changes made to parts 7 and 8 from S. C. van den Berg et al.[65]

The materials and printing techniques have been kept the same as the original design. However, some practical changes have been made. The iterative development of the prototype has led to several design observations relevant for both the original and the modified robot designs. These observations pertain to functional performance as well as operational considerations.

Firstly, all components are assembled using screws that are fastened directly into the 3D-printed parts. While this approach facilitates rapid assembly and modification, it presents limitations in terms of reliability. The screw holes require high dimensional accuracy, with deviations exceeding 0.15 mm potentially resulting in loose fittings. To address this, design modifications included increasing the thickness of screw holes. This adjustment increases the threaded engagement length, thereby improving the mechanical stability of the connections.

The use of 3D-printed parts as the structural base offers advantages in terms of reproducibility and rapid prototyping. However, 3D-printed materials are generally not inherently waterproof, which introduces complications during testing. In particular, the front section of the robot exhibits varying degrees of water tightness depending on print quality. Having many loose parts to assemble may have been valuable during the design development phase, but it slows down the experimental workflow due to the time required for assembly and disassembly of multiple parts.

According to the construction details in the paper by S. C. van den Berg et al. [65] the silicone tail should be made with shore 15 silicone. In this construction, Ecoflex 30 has been used. These are different types of silicone, and the numbers are not always comparable. Ecoflex has been used because it was readily available silicone. Multiple hardnesses have been explored, but due to the thin design and difficult moulding, Ecoflex 30 was the best silicone hardness. Therefore, the overall stiffness of the tail may be different from the original design.

3.4.2. Design results

The contribution of the piezoelectric material forms the core of this research. The choice for PVDF, contrary to other piezoelectric materials, is discussed in subsections 2.2.2 and 2.3.2. This section describes the rationale behind selecting the specific piezoelectric film and its placement on the robotic fish model.

Commercially available, ready-to-use piezoelectric transducers are generally difficult to source due to their highly application-specific nature. Consequently, the demand for such films is relatively low. PZT elements are more widely available than PVDF, primarily because PZT exhibits a higher energy output at smaller mechanical deflections, making it a preferred choice for sensing applications. However, its maximum allowable deflection is significantly lower, which limits its flexibility and applicability in systems requiring larger deformations.

Piezoelectric materials can be manufactured in various configurations, including stacks, strips, discs, and benders/films [122, 123, 124]. For this study, a piezoelectric *film* configuration was selected, as it is the only geometry capable of achieving bending motion in two directions. Other configurations primarily rely on expansion, contraction, or shape alteration, whereas thin films enable direct bending. These films are typically very thin and rectangular, which makes them lightweight and easily adaptable for integration into different mechanical systems.

Piezoelectric devices are generally designed for one of two primary purposes: as actuators or as sensors. Conceptually, sensors can be interpreted as energy harvesters, as both convert mechanical motion into an electrical signal. Conversely, actuators respond to an electrical input through deformation, producing mechanical work.

Because most commercial piezoelectric films are optimised for one of these functions, a film designed primarily as an actuator tends to perform less efficiently as a harvester, and vice versa. Specifically, a film optimised for actuation will yield a lower electrical output under the same mechanical excitation than a film designed for sensing. A film optimised for sensing exhibits a lower mechanical response when actuated under the same electrical excitation compared to an actuator-optimised film.

This presents a design challenge when attempting to employ a single piezoelectric element for both actuation and energy harvesting. The width and length of the chosen film are determined by the dimensions of the robotic tail's backbone, while the film thickness strongly influences efficiency in both sensing and actuation modes. A thicker film generates a higher electrical output when subjected to deformation, but requires a higher driving voltage to achieve the same bending amplitude as a thinner film. Therefore, a film with a relatively small thickness was chosen to enhance harvesting efficiency. However, very thin films produce lower actuation forces due to reduced stiffness. Consequently, a moderate film thickness was selected to achieve a balance between actuation and harvesting performance. The specific film used in this study is presented in Figure 3.11. Specific material characteristics are given in section 4.3.1.

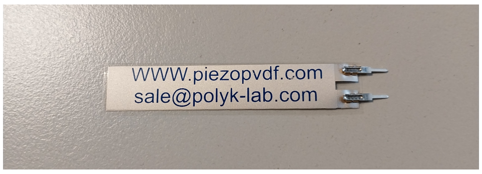

Figure 3.11: Piezoelectric film from PolyK [122]

Determining the optimal placement of the piezoelectric film on the robotic tail is non-trivial, as the ideal locations for actuation and harvesting do not coincide. Maximum actuation efficiency is achieved by inducing bending moments along the backbone, similar to the mechanism used in the original robotic fish design [65]. In contrast, maximum energy harvesting occurs where the tail experiences the greatest deflection, which is typically near the rear silicone section and the caudal fin connection, similar to the placement by D. Tan et al. [70].

For practical reasons, the piezoelectric film is not placed on the external surface of the tail, as this region is in contact with water and poses a high risk of electrical damage to the circuit. Instead, the film is positioned in a region that ensures better water resistance—inside the silicone tail structure. Embedding the entire circuit within the silicone section was not pursued due to time constraints, including reconfiguring the silicone mould, moulding and altering the last rib to allow the electrical circuit through.

The backbone provides a reliable indication of the overall bending motion of the tail, while being less affected by turbulence or flow-induced vibrations compared to the tail surface. Since the original design demonstrated efficient propulsion through backbone actuation, the piezoelectric film was placed along the backbone to serve both as actuator and energy harvester.

An alternative and potentially more efficient approach would involve the use of multiple piezoelectric films placed at different positions along the tail, each optimised for a specific function (i.e., actuation or harvesting). Such a design would allow the use of distinct piezoelectric materials or thicknesses tailored to each role. However, due to limitations in time and material availability, this study focuses on a single integrated film serving both purposes. Future work could explore multi-segment configurations for improved efficiency and performance.

The final optimal backbone thickness for this design is 0.8 mm. This configuration exhibited the most favourable flapping behaviour—both in frequency and amplitude—during harvesting, while avoiding any substantial increase in the actuation force required for propulsion. Higher flapping frequencies and amplitudes are directly associated with greater energy-harvesting potential, and among all tested stiffness configurations, the 0.8 mm backbone demonstrated the best overall performance. Therefore, a thickness of 0.8 mm is adopted in the final design.

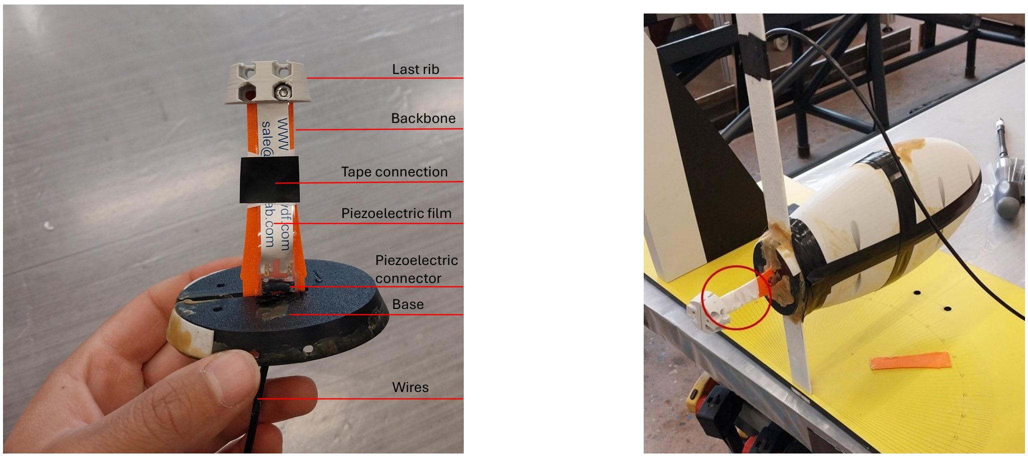

(a) Placement of the piezoelectric film before covering

(b) Location of the piezoelectric film in the robot body

Figure 3.12: Placement of the piezoelectric film in the underwater robot

The placement of the piezoelectric film in the underwater robot is presented in Figure 3.12. This figure includes the 0.8mm thick backbone in orange and the first and last rib. Figure 3.12a shows the close-up of the placement with a label of each part, and Figure 3.12b shows the placement of the piezoelectric film in the entire underwater robot. The only this missing in this figure is the silicone tail cover with the middle ribs and the caudal fin. These have been left out of the figure for clarification. The new SolidWorks construction of the interior of the tail is presented in figure 3.13.

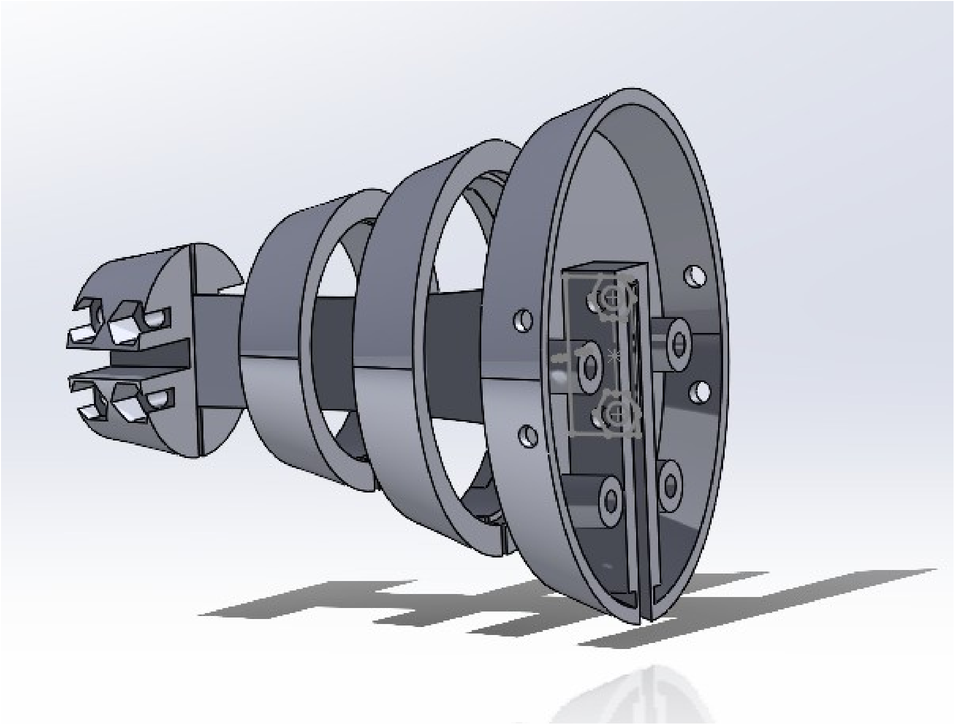

Figure 3.13: Final result of the tail interior design

4

Experimental testing

This chapter presents the experimental validation of the design through five distinct tests. Each test addresses a specific design question and evaluates key performance parameters related to propulsion, energy harvesting, or structural behaviour. For each experiment, the setup, methodology, results, associated uncertainties, and corresponding discussion are systematically described. Together, these tests provide the empirical foundation for assessing the functionality and efficiency of the proposed underwater robot design and for guiding subsequent design iterations. The specifics of the test setup can be found in Appendix A.

4.1. Wind lab tests

The wind lab tests were primarily conducted to qualitatively observe tail motion and test the mechanical integrity of the setup before quantitative measurements in the flume tank. These wind lab experiments provided a straightforward way to identify potential design or assembly issues without exposing the model to water. Additionally, the results were used to identify which backbone stiffness exhibited the most effective flapping behaviour in terms of frequency and amplitude, thereby reducing the number of configurations requiring subsequent flume tank testing.

The wind lab tests include wind coming from the front; no other angles are tested because these are also not tested in the flume tank. Testing additional angles of incoming flow is not within the scope of the project.

4.1.1. Wind lab test setup and testing

The wind lab setup was designed to enable accurate measurements of the tail's flapping amplitude and frequency. An overview of the complete setup is shown in Figure 4.1, and its main components are listed below.

- Solid base from wood/polymethylmethacrylate (PMMA) with printed 180 angles and bolt holes (figure A.1)
- steel 'T-shaped' strut (figure A.2)
- PLA 3D printed angle bracket (figure A.3)
- 3, 6 and 7mm diameter bolts and lock nut
- GoPro (type?)

The top surface of the solid base includes a 180° printed scale, which serves as a visual reference background for measuring tail motion. A GoPro camera mounted on the top of the steel strut records the tail's movement from above. The angular deflection of the tail is then quantified from the recorded footage by comparing its position to the printed angle markings. The calibration procedure used to convert the visual data into angular displacement is described in section 4.1. This method was selected for its simplicity and direct visual interpretability.

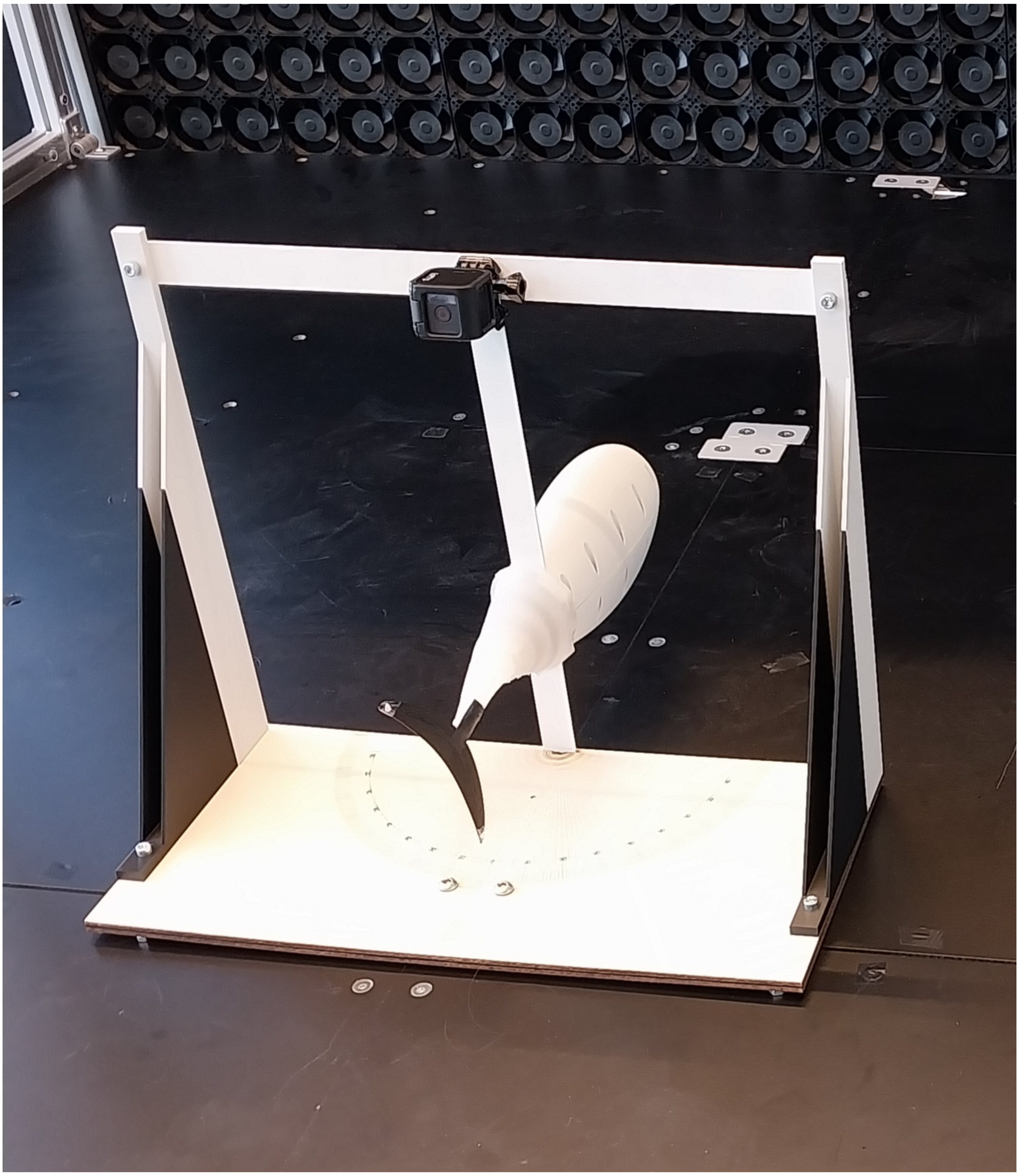

Figure 4.1: Test setup, photo taken in the wind lab

Steel was selected for the strut as it was the stiffest material available at FW. For the underwater experiments, the steel strut was coated with a protective paint layer to prevent corrosion. The strut is mounted to the base via a central slit aligned with the 180° scale. At the T-junctions, the strut is connected to the support brackets using 6 mm bolts and nuts, and the brackets are similarly fastened to the base.

The 7 mm bolts secure the entire setup to the racks in the ME wind laboratory. The brackets support the strut when subjected to air or water flow, ensuring structural stability. The 3 mm bolts are used to assemble the underwater robot components and to attach the robot to the test setup.

The GoPro camera used in the experiments is waterproof and capable of recording at a frame rate sufficient for slow-motion playback at 25% of real time. This temporal resolution allows accurate estimation of the tail's flapping amplitude and frequency under flow conditions. The same camera setup was used for both wind lab and flume tank tests. The camera was mounted centrally on the T-shaped strut using double-sided adhesive tape and reinforced with waterproof tape for underwater operation. The camera's angle relative to the base was fixed by securely tightening the adjustable base mount.

The experiments were carried out in the wind laboratory of the Faculty of Mechanical Engineering at TU Delft. The facility contains multiple axial fans that can be operated simultaneously and controlled through a central panel. All fans were run at the same power setting for each test. The achievable wind speed ranges from 0 to approximately 16 m/s, though for safety reasons the power was limited to 75% of the maximum. Figure 4.2 shows an overview of the facility.

The setup was mounted onto the existing screw holes of the laboratory rack. The rack can move independently but can also be secured to the floor. The distance between the fans and the model was measured as 131 ± 1.5 cm. The model was assumed to be positioned perpendicular to the fans, as the racks themselves are aligned perpendicularly. For safety reasons, the front rack cannot be moved with respect to the fans, and the screw holes are fixed; therefore, the setup angle cannot be adjusted. The uncertainty in the alignment angle was not quantified, as it was assumed to be negligible compared to the expected turbulence in the airflow and the small geometric offset of the setup.

The wind lab does not have a circular flow and is susceptible to turbulence. To verify the actual flow conditions, wind speed measurements were taken using a Testo 410i anemometer with an accuracy of $\pm$0.2 m/s + 2% of the reading and a resolution of 0.1 m/s [125]. Because the local flow may vary due to turbulence and distance from the fans, the anemometer was positioned both directly in front of the model (approximately 2 cm away) and next to it at the same distance from the fan array. The measurement in front of the model was performed once, as the sensor obstructed the flow and prevented simultaneous video recording. Two measurements were performed next to the model to estimate the average air speed during testing. The number of wind measurement tests was limited due to wind meter availability.

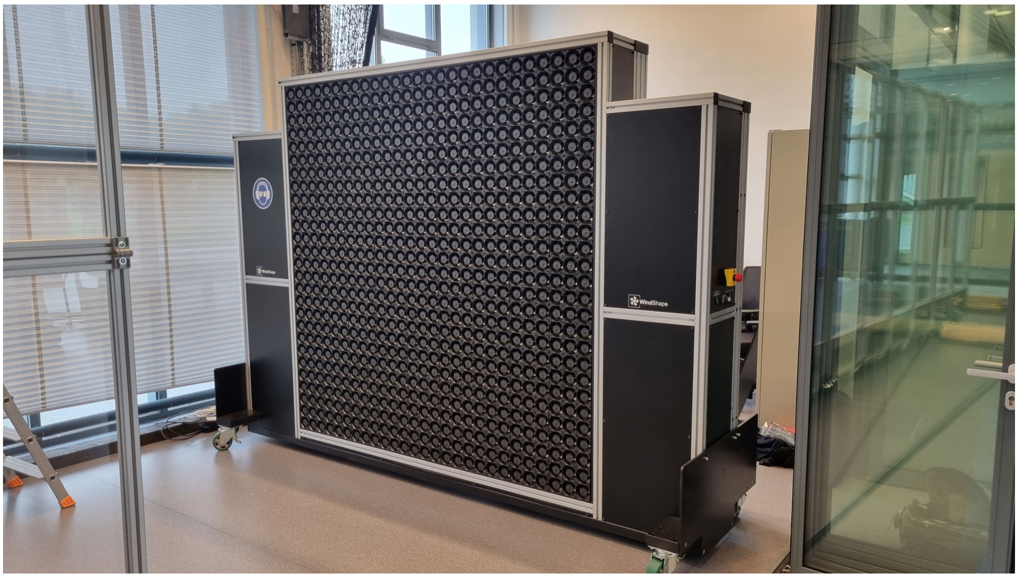

Figure 4.2: Wind lab Technical University Delft [126]

The Cauchy number (Ca) (Eq. 4.1) was used to achieve dynamic similarity between air and water tests, as it relates fluid dynamic pressure to material stiffness. The bulk modulus of elasticity k was assumed constant for all tests.

$$Ca = \frac{\rho \times U^2}{k} \tag{4.1}$$

Here, ρ is the fluid density, U the characteristic flow velocity, and k the bulk modulus of elasticity of the backbone material. The densities were taken as $\rho_w = 998.34\ \mathrm{kg/m^3}$ for water and $\rho_a = 1.20\ \mathrm{kg/m^3}$ for air at 20°C. To match a representative flume tank condition of $U_{w,\max} = 0.4\ \mathrm{m/s}$, the equivalent air speed was calculated as $U_{a,\max} = 11.52\ \mathrm{m/s}$. This wind speed is used as the target speed for the wind lab. This estimate neglects the effects of viscosity and added mass, which differ between the two flow media. Therefore, the wind lab is not a perfect alternative for underwater tests.

For safety, the wind speed was increased stepwise to 20%, 40%, 60% and 75% of the maximum fan power, corresponding approximately to the target range derived from the Cauchy scaling.

To determine the influence of the T-shaped strut on the tail motion, the wake frequency is estimated using the Strouhal number for a flat plate. The wake frequency is calculated as

$$f = \frac{St \times U}{D} \tag{4.2}$$

where St is the Strouhal number, approximated as 0.12 [127, 128], D is the thickness of the plate (2 mm in this case), and U is the wind speed. For each wind speed, the corresponding wake frequency is plotted in subsection 4.1.2.

Tail motion was quantified using the printed 180° reference scale on the base plate (see Section A). Because the GoPro camera observes the tail from above, a geometric offset exists between the printed scale and the actual tail plane. To correct for this, calibration blocks were 3D printed at angles of 2°, 4°, 6°, 8°, 10°, and 20°, each matching the vertical distance between the tail and the base. The lower edge of each block aligned with the 0° mark on the base and the corresponding angle, while the upper edge defined the same angle at the tail height—visible to the camera. By recording each calibration block, the apparent visual offset between the printed and actual angles was determined. A visualisation of the concept is given in figure 4.3.

The calibration is performed multiple times. Twice during the wind tests and twice during the underwater tests. The calibration was only performed when the strut had been moved for assembly purposes.

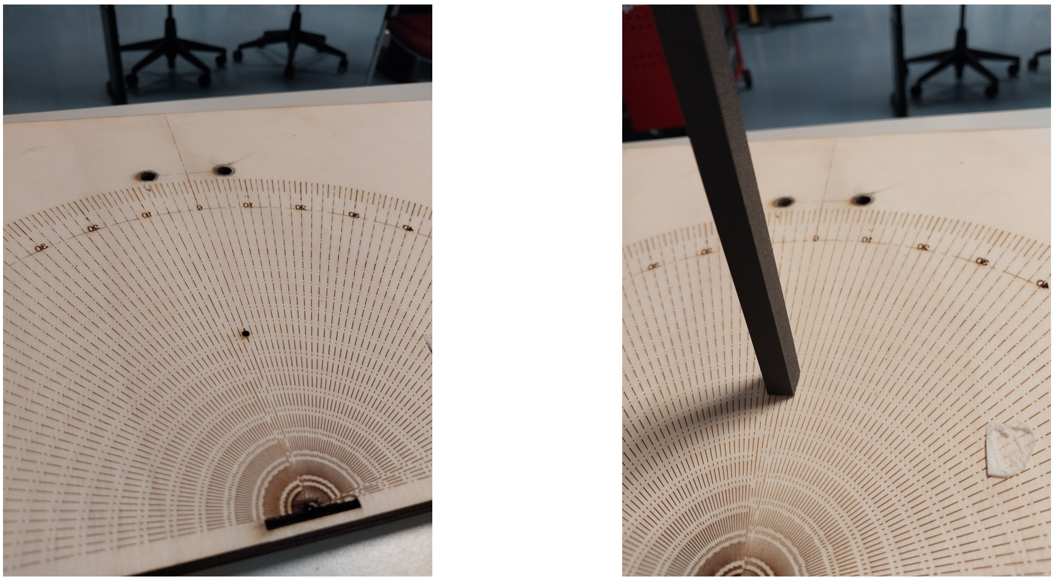
(a) Calibration hole in the base (b) Calibration block in hole

Figure 4.3: Angle calibration system

Otherwise, the calibration has been assumed to be the same. The offset increases with increasing angles. This follows expectations because if there is an offset, the angle at which this offset is observed increases because the distance per angle measured increases.

The calibration results per measurement are similar for smaller angles. Each measurement starts with an offset of $\pm$ 2 degrees at 2 degrees. This does not mean that the observed amplitude is off by 2 degrees. Because the observed amplitude measurement is based on the relative movement of the tail. That is why it is important to understand the increasing offset at certain distances along the base.

The maximum deflection measured at 20 degrees was $\pm$ 6 degrees. The uncertainty in the amplitude measurement is a combination of the relative movement of the tail and the location of the tail along the board. If the tail is oscillating between 5 and 10 degrees, for example, the offset is different from if the tail is oscillating between -2 and 2 degrees. The uncertainty is determined at ±1°, with a maximum of ±2°.

The frequency measurement uncertainty is difficult to determine since the frequency is determined manually. Each test has been counted multiple times, and the counting has been performed at a slower playback speed to ensure no movement was missed. The only uncertainty in this case would be at the start and end of each measurement, determining how far into a movement the tail motion was at the start and how finished it is at the end of the run. Therefore, the uncertainty assumption per measurement is a maximum of 0.5 cycles at the start and at the end of the measurement. Over 10s, 1 uncertainty cycle accounts for an uncertainty of 0.1Hz.

Each backbone stiffness configuration was tested at the four wind speed levels. For each run, the GoPro camera was started first, followed by activation of the fans at the selected power level. After at least 20 s of steady airflow, the fans were switched off and the recording stopped. The camera operated at a sufficient frame rate to allow accurate playback at 25% speed for motion analysis.

The flapping amplitude and frequency were determined manually from the video footage over a 10 s interval where the wind speed remained constant. Manual analysis was chosen as it provided sufficient accuracy within the available time constraints. The resulting amplitudes and frequencies are presented in subsection 4.1.2.

4.1.2. Wind lab results and discussion

The average wind speed from Table 4.1 is the wind speed that is taken as the speed per fan power in the strut wake calculations. This average consists of the 2 measurements next to the model and one in front. The results of the measurements are plotted in figure 4.4. In the measurements, it is evident that the wind speed measured right in front of the model is indeed slightly slower than the wind speed measured next to the model. This is expected because the test setup and model influence the wind flow, and therefore also the flow around the measurement device.

The average wind speed from Table 4.1 is the wind speed that is taken as the speed per fan power in the strut wake calculations. This average consists of the 2 measurements next to the model and one in front. The results of the measurements are plotted in figure 4.4. In the measurements, it is evident that the wind speed measured right in front of the model is indeed slightly slower than the wind speed measured next to the model. This is expected because the test setup and model influence the wind flow, and therefore also the flow around the measurement device.

Table 4.1: Average air speed

Fan power [%]	Average wind speed [m/s]
20	3.50
40	6.65
60	9.55
75	11.95

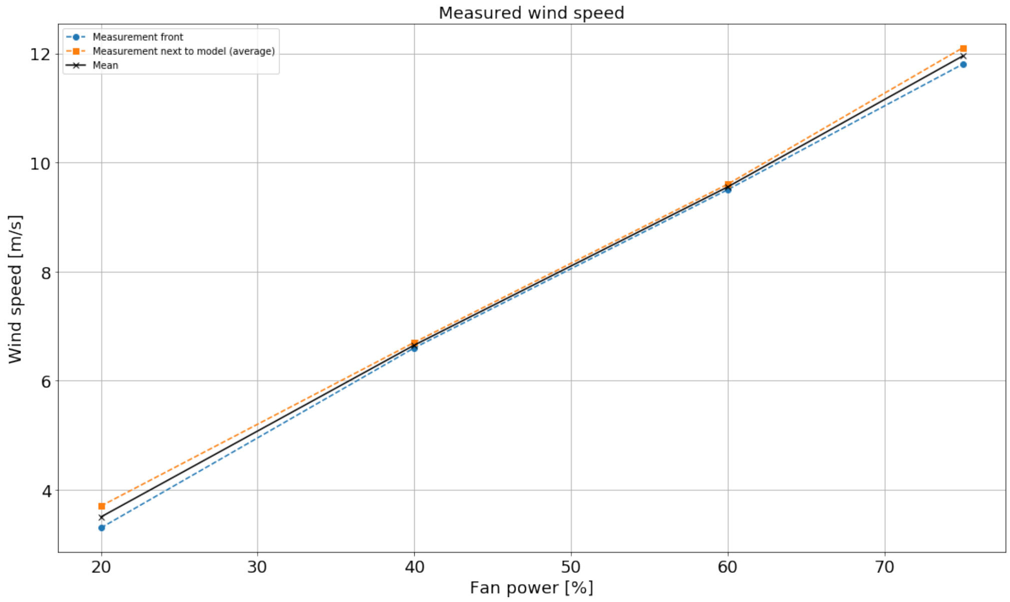

Figure 4.4: Measured air speeds

The expected wake frequency (Figure4.5) from the strut is expected to be higher than 16Hz and over 55Hz at the highest wind speed corresponding to 75% fan power. This is based on the calculation from equation 4.1. If the difference between the tail flapping frequency and the plate wake frequency is large, it is assumed that the strut does not influence the tail movement.

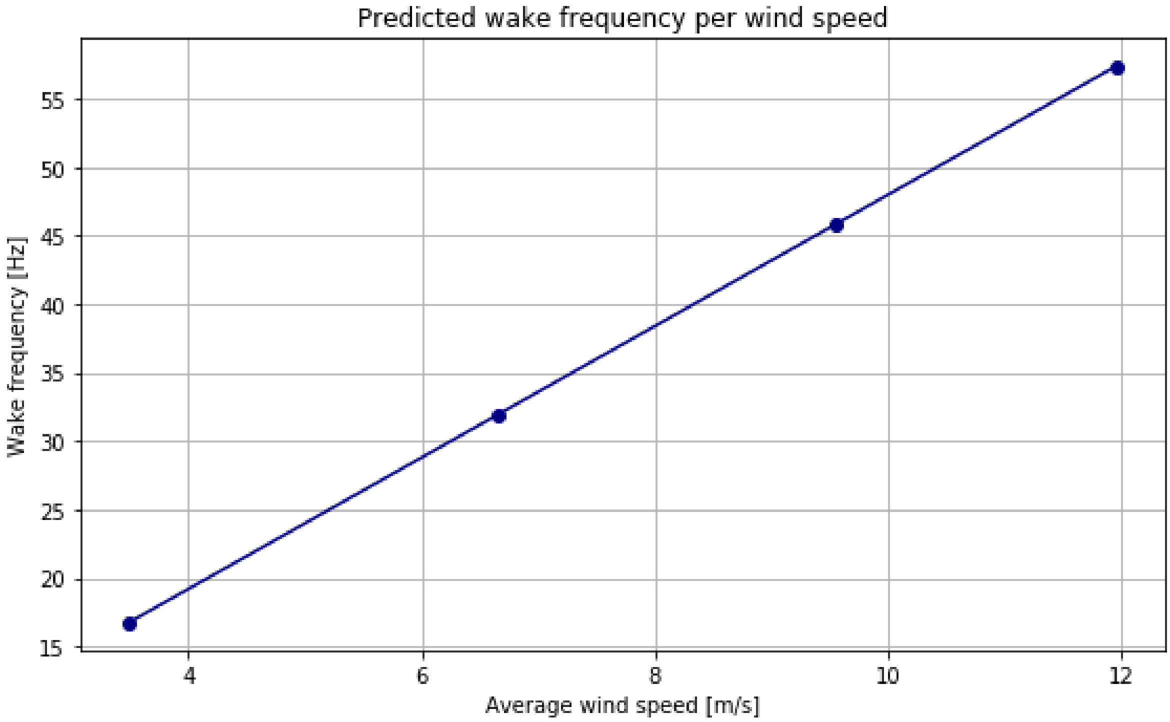

Figure 4.5: Predicted wind wake frequency

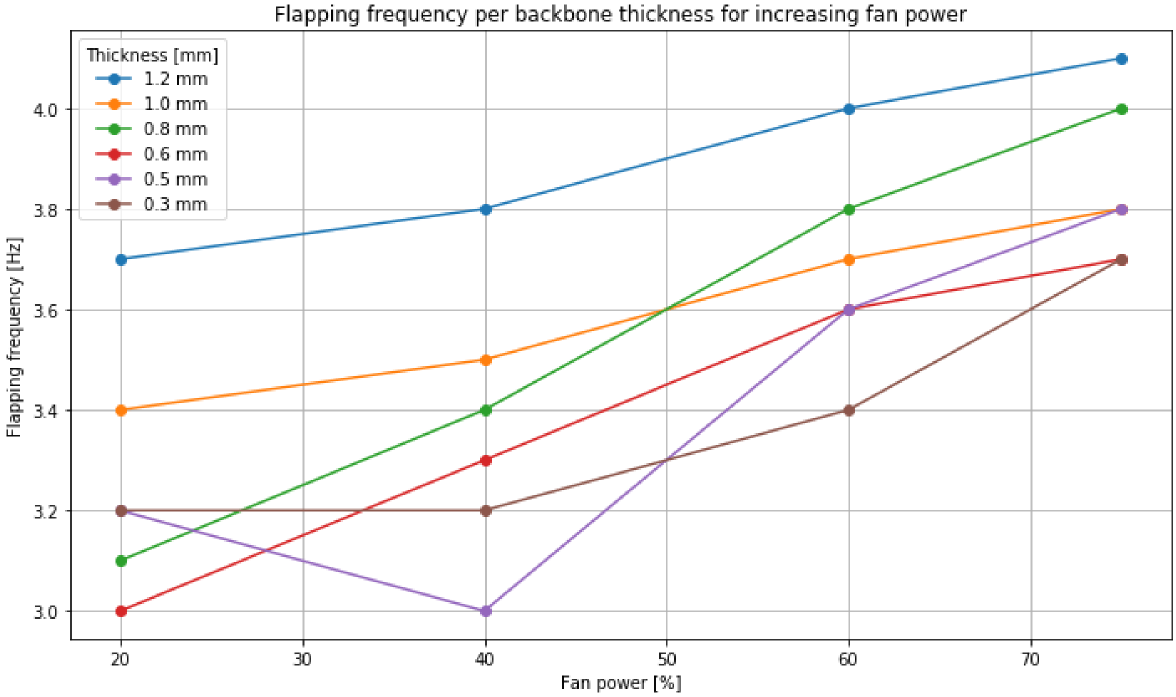

Figure 4.6: Wind lab flapping frequency results

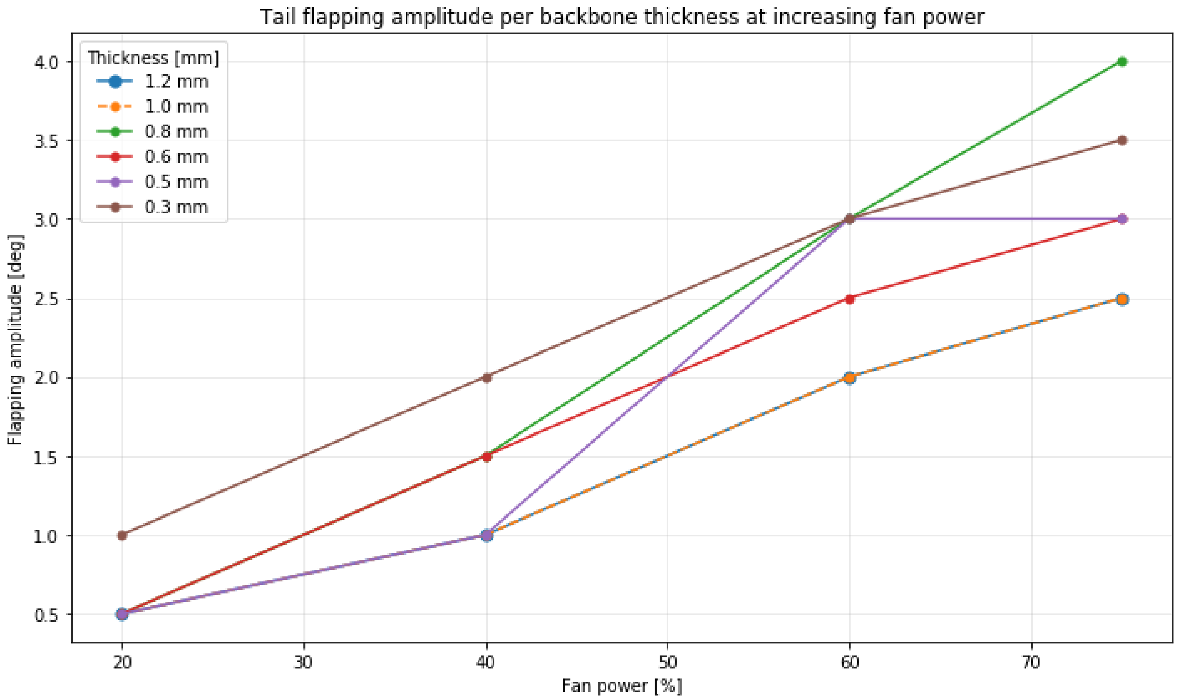

Figure 4.7: Wind lab flapping amplitude frequency

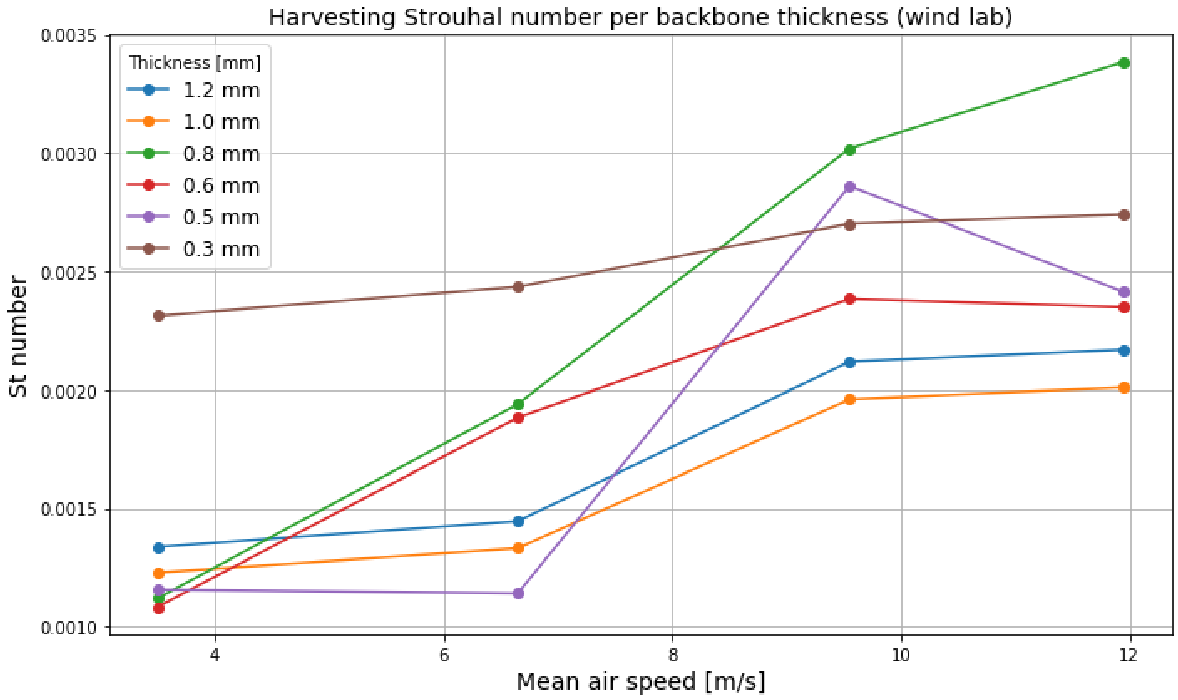

Figure 4.8: Strouhal number calculated based on the flapping results per air speed

From Figure 4.6, the flapping frequency increases with higher fan power. This trend is consistent with the literature, which states that harvesting efficiency depends on the Reynolds number (subsection 2.2.1, Equation 2.2). The highest flapping frequencies occur for the stiffest backbone, which aligns with previous research showing that stiffer foils generally exhibit higher efficiencies (subsection 2.2.1). The lowest backbone thicknesses exhibit the lowest frequencies overall and follow a different trend compared to the other stiffnesses. This may indicate that the stiffness of the silicone tail cover has influenced the flapping behaviour at these low backbone stiffnesses.

Figure 4.7 shows the corresponding flapping amplitudes for the same experimental runs. As with the frequencies, the amplitude increases with fan power, as expected. In general, the lower stiffnesses exhibit higher amplitudes, with the exception of the 0.8 mm backbone, which performs similarly to—or in some cases better than—the lower stiffnesses.

The corresponding Strouhal number (St) for each air speed is shown in Figure 4.8. At low air speeds, the thinnest backbone performs closest to the desirable St range; however, due to the very small amplitudes (in meters), the resulting St values still do not fall within the optimal interval. At higher air speeds, the 0.8 mm backbone shows the best overall performance. Neither the flapping frequency nor the amplitude increases linearly with wind speed.

These results do not include the video analysis. Visual inspection revealed that the flapping behaviour of the lowest stiffnesses (0.3–0.5 mm) is relatively inconsistent, particularly in terms of amplitude and frequency intervals. Although the plotted results represent averaged values, the video observations indicate relatively high uncertainty for these stiffnesses. For this reason, the 0.3 mm and 0.5 mm backbones were excluded from the flume-tank tests, even though their average flapping performance initially appeared favourable.

The best overall performance in terms of amplitude and frequency—particularly at higher air-flow speeds—is achieved by the 0.8 mm backbone. Therefore, this thickness was selected for the flume-tank experiments. While the 1.2 mm backbone exhibits a slightly higher St than the 1 mm backbone, increasing the stiffness beyond that of the original design would require a higher actuation force during swimming. Consequently, the 1.2 mm backbone was also excluded. Thus, three backbone stiffnesses were tested in the flume tank: 1.0 mm, 0.8 mm, and 0.6 mm.

4.2. Flume tank test

The underwater tests were conducted to evaluate the flapping behaviour of the robotic fish tail under realistic submerged conditions. The experimental setup and model were identical to those used in the wind lab, except that the solid wooden base was replaced with a wider (PMMA) version to ensure water resistance and to provide sufficient space for attaching external weights that stabilised the setup during water flow.

The flume tank at TU Delft is a closed-circuit facility capable of generating flow velocities between 0 and approximately 0.5 m/s, taking safety margins into account. The water depth can be varied up to approximately 45 cm, and the flow velocity is controlled by adjusting the pump power as a percentage of the total capacity. During the experiments, the power was set to 10%, 20%, 30%, and 40% of the maximum output.

4.2.1. Flume tank test setup and testing

The test setup, contrary to the wind lab experiments, is expected to influence the movement of the tail. This means that the wake from the strut may interfere with the flapping amplitude and frequency of the tail during measurements. This has been considered, and the setup remains unchanged for the flume tank tests. This decision is made considering the simplicity of the setup and the reliance of tail movement during tests due to the strut-generated wake. Alternative test setups require complex solutions to measure the tail flapping amplitude and keep the model stationary with minimal influence on the flow.

The corresponding flow velocities were measured using a Valeport flow meter [129], positioned approximately (300 cm) downstream and (55 cm) laterally offset from the model, as shown in Figure 4.9. The instrument operates in the range of 0.03–10 m/s, with an accuracy of ±1.5% of the reading for $U > 0.15$ m/s and ±0.004 m/s for $U \leq 0.15$ m/s.

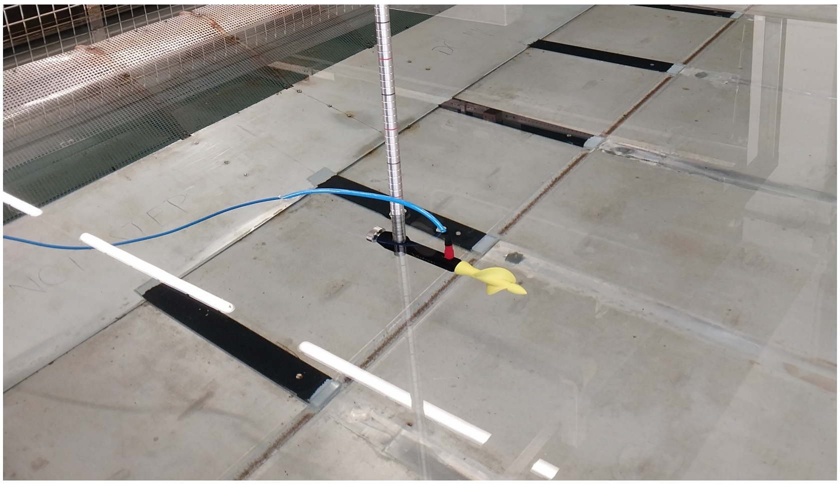

Figure 4.9: Flow meter setup

Three measurement runs were performed to determine the relationship between flow percentage and flow velocity. One run was conducted without the model in the tank to characterise the baseline flow, and two runs were performed with the model present. The resulting velocities were averaged over a 90 s interval once a steady-state flow was reached, and the results are presented in Figure 4.11 and Table 4.2.

Before connecting the energy-harvesting circuit, the model was tested without electrical components to (i) verify the mechanical integrity of the setup, (ii) determine which backbone stiffness would be used for the circuit tests, and (iii) allow additional time for waterproofing the circuit components without risk of damage.

A stiffness of 0.8 mm was ultimately chosen for the circuit-integrated tests. Additionally, a slightly increased effective stiffness was expected once the piezoelectric film and its mechanical connection to the backbone were added. Since the difference between the stiffness of 1mm and 0.8mm is similar. The latter was chosen because the stiffness increase due to the piezoelectric film is not expected to exceed the stiffness of 1mm. Excessive stiffness, however, would negatively affect swimming performance by increasing the required actuation force.

The model was waterproofed using waterproof tape and sealing wax. Since the 3D-printed parts are not inherently watertight, additional wax was applied in small crevices, and a waterproof spray was used as a protective coating.

The setup was anchored in the tank using three (5 kg) weights on each side of the support brackets. The centerline of the tank was located with a measuring tape, and the setup was positioned parallel to the walking bridge at a distance of (315 m). The water depth was set to 41 cm—sufficient to fully submerge the model. A photograph of the submerged setup is shown in Figure 4.10.

Figure 4.10: Flume tank test setup

The first phase of testing, performed without the electrical circuit, followed the same procedure as the wind lab experiments. The tail's flapping amplitude and frequency were determined from camera footage after at least one minute of steady flow had been achieved. The GoPro camera lens was positioned underwater to eliminate surface reflections and ensure clear visualisation of the tail motion.

4.2.2. Flume tank results and discussion

The average measured flow speed in the flume tank is given in Table 4.2. These are the water speeds that are used in the strut wake calculations. In figure 4.11, the 3 water flow speed measurements are plotted. The measurement with the model and measurement 2 without the model have very few deviations from each other. Therefore, it is concluded that the model does not influence the measurement of the water flow speed.

Table 4.2: Average flume tank flow speed

Flume tank power [%]	Average flow speed [m/s]
10	0.081
20	0.196
30	0.285
40	0.364

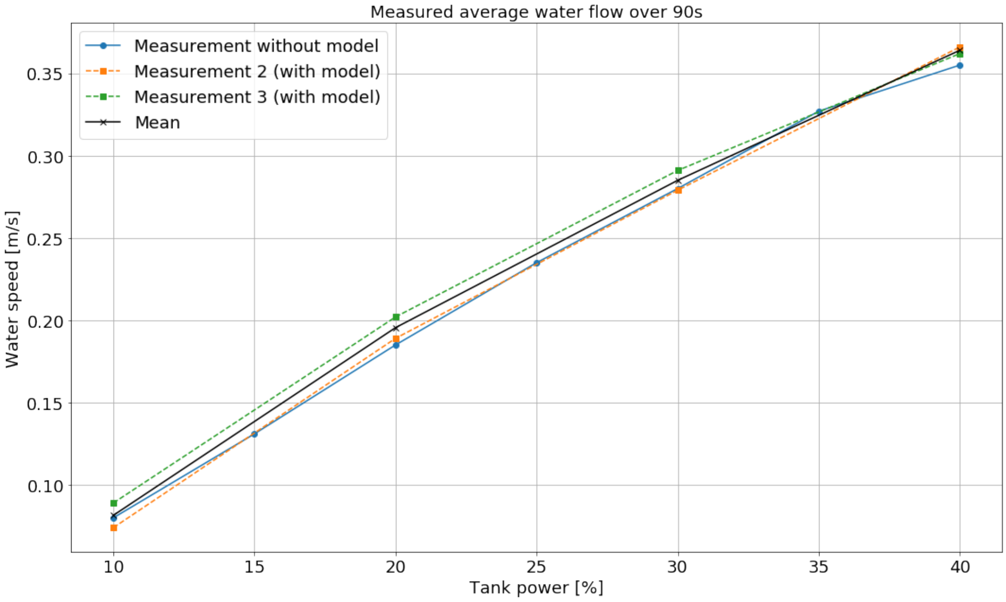

Figure 4.11: Measured water flow speeds

The 3 different measurements show some deviations in speed. This may have an influence on the tail motions, but the largest expected influence on the tail flapping frequency and amplitude is the strut of the test setup. The wake frequency of the strut is dependent on the water flow speed. The frequency results of each stiffness in Figure 4.12 are relatively close together. The reason behind this is described in subsection 4.2.1.

The flapping amplitude, shown in Figure 4.13, corresponds to the same experimental runs presented in Figure 4.12. The largest differences in amplitude occur at low flow speeds, whereas at the highest flow speeds the amplitudes become similar across the tested stiffnesses. This may indicate that, at certain flow velocities, the tail motion becomes dominated by the wake-induced forcing rather than by backbone stiffness. Alternatively, it may suggest that each flow speed imposes a maximum achievable deflection, beyond which the tail doesn't bend further.

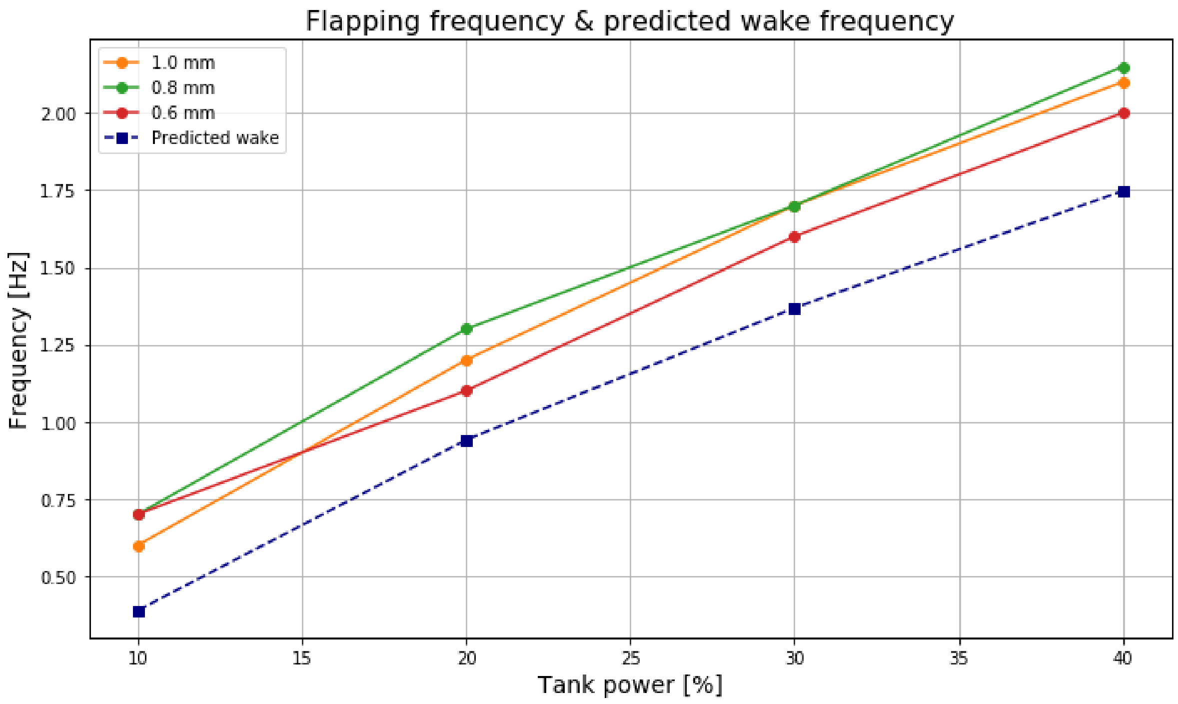

Figure 4.12: Predicted water wake and tail flapping frequency

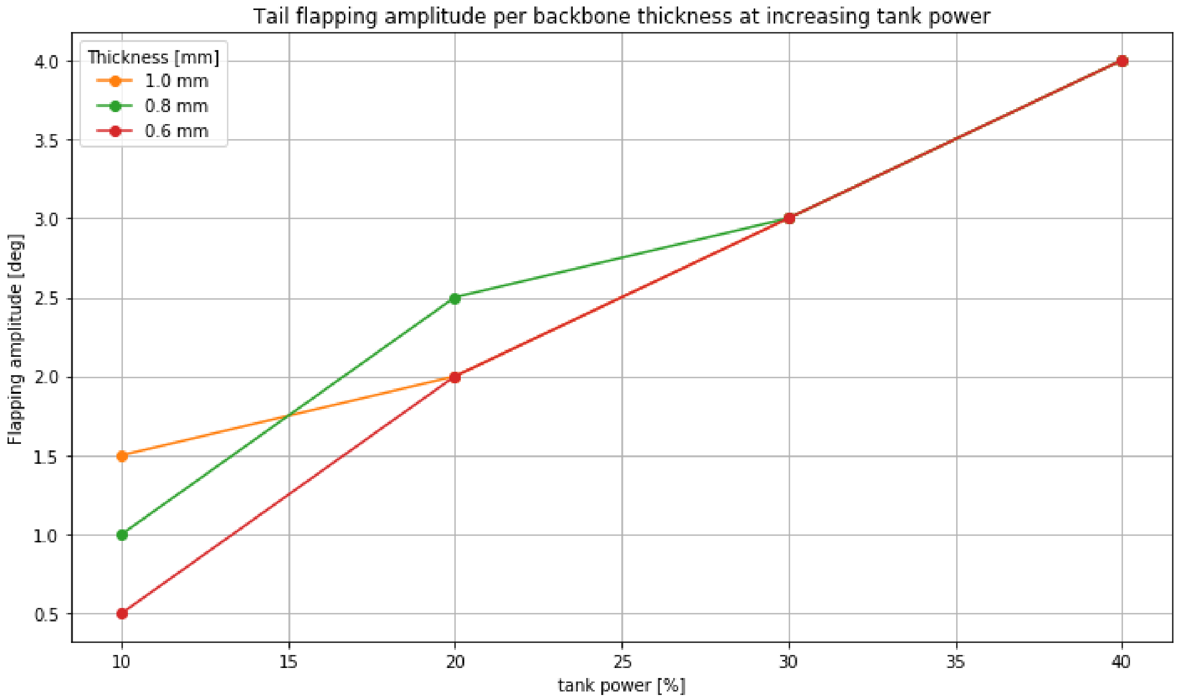

Figure 4.13: Flume tank tail flapping amplitude

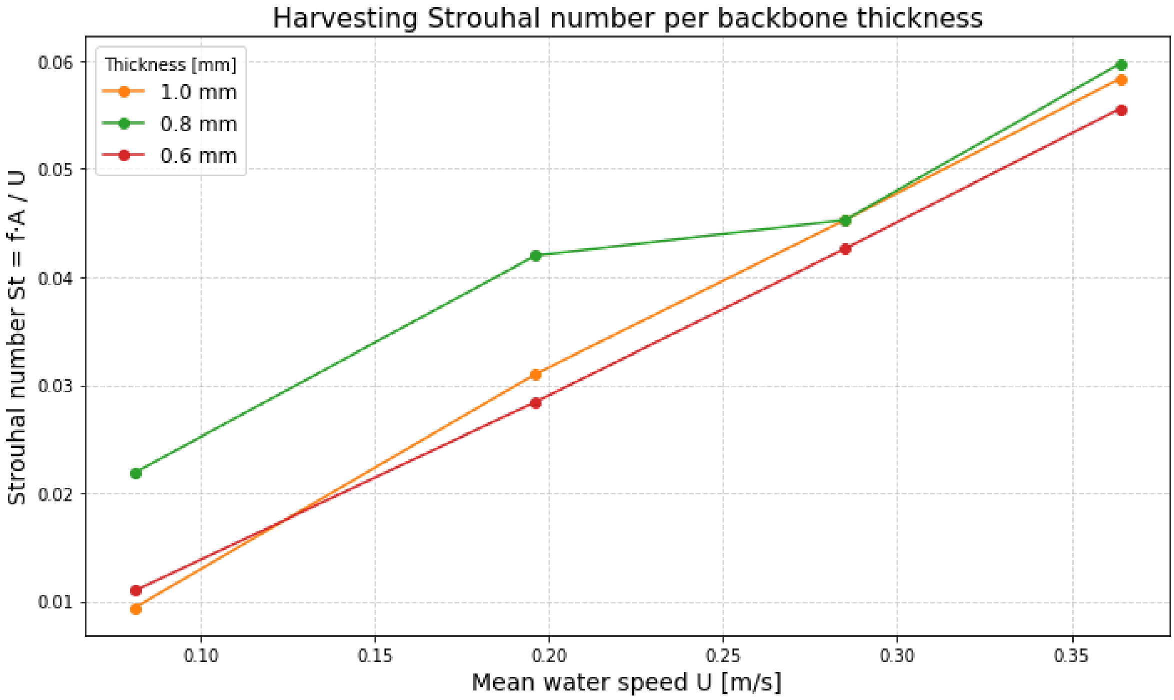

Figure 4.14: Strouhal number calculated based on flapping results per water flow speed

Similar to the wind-lab tests, all measured trends increase with tank power. The calibration results are the same as for the wind lab tests discussed in subsection 4.1.1. The most notable difference between the wind and water results is the corresponding St number, shown in Figure 4.14. Although the values remain outside the desired range, they are substantially higher than those obtained in air. This difference arises because the water speeds in the flume tank are considerably lower, while the flapping frequency is only about 1 Hz lower, and the amplitude is comparable or larger. The larger caudal fin used during the flume-tank experiments, as well as the additional hydrodynamic mass, are assumed to contribute to this increase in performance.

Among the tested stiffnesses, the 0.8 mm backbone exhibits the highest efficiency in terms of St number. Consequently, this backbone thickness is selected for the final design in which the harvesting circuit is integrated. This selection ensures that the final prototype operates within the most favorable balance of actuation requirements and harvesting efficiency identified during experimental validation.

4.3. Energy harvesting test

This section describes the development, implementation, and evaluation of the energy harvesting circuit used in this research. The goal of this test is to verify whether the electrical output generated by the piezoelectric films during tail flapping can be rectified, stored, and measured in a controlled manner. The design of the circuit is based on established principles for piezoelectric energy harvesting. The following subsections outline the circuit architecture, component selection, and experimental procedures used to assess the feasibility and performance of the harvesting system.

4.3.1. Electrical harvesting circuit

The electrical circuit described in this section is based on the energy harvesting part of the setup. The circuit was developed together with technician Jacques Brenkman from FW and underwent several iterations to verify proper operation.

The aim of the circuit setup is to quantify how much power can be extracted from a single piezoelectric film when subjected to water flow. Only one piezoelectric film was used, both to simplify the circuit and due to the limited availability of samples.

The piezoelectric film used is a PVDF element from PolyK [122]. These $50\,\mathrm{mm} \times 10\,\mathrm{mm}$ films are highly flexible and therefore resistant to mechanical failure, making them suitable for experimental purposes. The dimensions fit precisely within the interior structure of the underwater robot's tail. Therefore, no alterations to the dimensions of the original tail have been made. These films are also inexpensive and readily available in bulk, which makes them practical for research and prototyping. However, this cost advantage comes at the expense of optimal performance; this trade-off is acceptable for this study, as more efficient films can later be integrated for upscaling.

The $50\,\mu\mathrm{m}$ thick film has a capacitance of $1.25\,\mathrm{nF}$, a Young's modulus of $2200\,\mathrm{MPa}$, and piezoelectric constants $d_{31} = 15\,\mathrm{pC/N}$ and $d_{33} = 30\,\mathrm{pC/N}$ at $22\,^{\circ}\mathrm{C}$ and $100\,\mathrm{Hz}$. The voltage output can be approximated using Eq. 4.3:

$$U = \frac{g_{33} \times F \times t}{B \times L} \tag{4.3}$$

Here, $g_{33} = 350\,\mathrm{mV\,m/Nm^2}$, F is the applied force, t is the film thickness, and $B \times L$ represents the electrode area. The resulting output voltage U is expressed in millivolts.

The circuit was assembled on a perfboard of approximately $4 \times 2\,\mathrm{cm}$. All connections were soldered, except for the piezoelectric film leads, which were placed in a 2.54 mm connector. This was done because the piezoelectric film material can be damaged by heat during soldering.

The simplest circuit consisted of a direct connection between the piezoelectric film and a voltage meter. According to the datasheet, the output voltage U under a 1 N applied force, as given by equation 4.3, is 35 mV. This basic configuration served to verify the accuracy of the datasheet specifications.

Subsequently, the piezoelectric film was connected to an LED to assess whether it could generate sufficient power to illuminate the LED. To compensate for the low voltage and current output, a millivoltage amplifier was introduced. This approach provided a practical and rapid solution, as stacking multiple piezoelectric films in series—though an alternative to increase the voltage—would require additional films and considerable manual labour, which were not available within the scope of this project. An iteration that includes all the components before soldering is given in Figure 4.15. Here, the voltage output is checked with a voltage meter to determine whether the output after adding the voltage amplifier is sufficient.

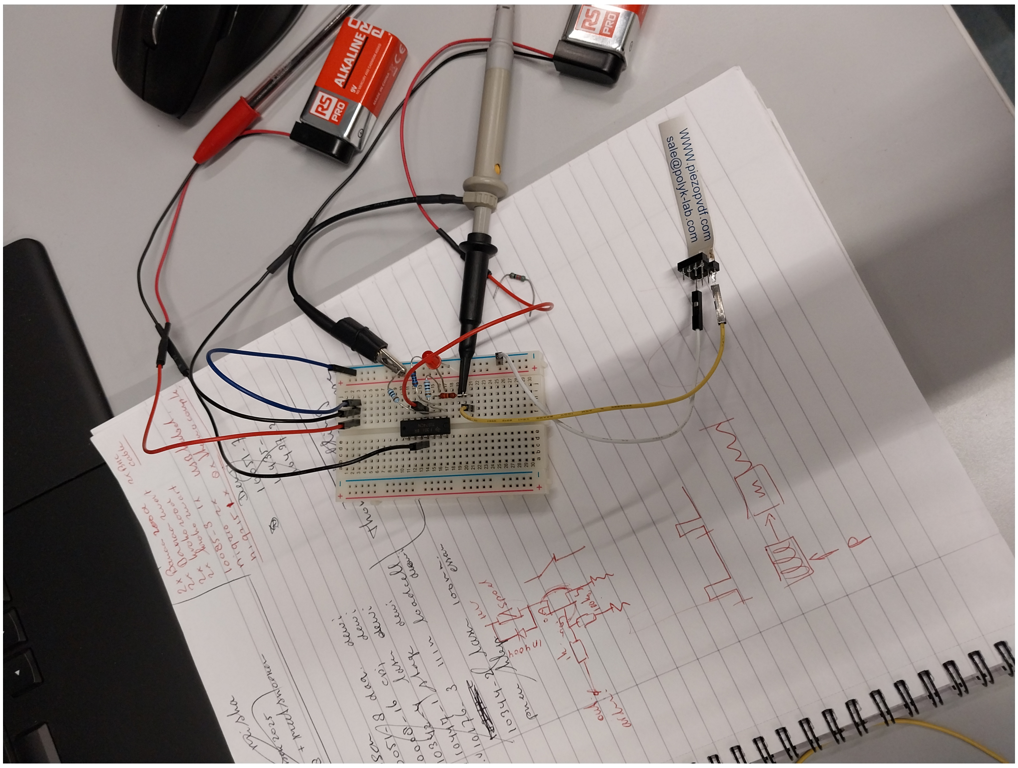

Figure 4.15: Circuit iteration with piezoelectric film, amplifier, and voltage meter

Because the output voltage of a single piezoelectric film is positive when bending in one direction and negative when bending in the opposite direction, multiple films must be stacked to avoid voltage cancellation. Such a stack needs to be in series to increase the net voltage output. While the LED served as a qualitative indicator of piezoelectric functionality, it does not provide precise quantification of the voltage generated. Therefore, in the final iteration, the LED was replaced with a voltage meter connected across a resistor to allow accurate measurement of the electrical output.

A schematic of the circuit is shown in Figure 4.17. The circuit consists of a signal source — the piezoelectric film — which generates voltage under mechanical stress. The voltage amplifier remains in the final circuit because the raw output from the piezoelectric film is too low to be reliably distinguished from measurement noise or offset. The amplification rate is determined by resistors R_1 and R_F, as given by Eq. 4.4:

$$\text{Amplification rate} = \frac{R_F}{R_1} = \frac{100\,k\Omega}{1\,k\Omega} = 100\times \tag{4.4}$$

With an average voltage output of 35mV, an amplification factor of 100 is sufficient to power the LED, taking into account the boundary conditions of the LED. In the final version, 100 times has been decided as a suitable amplification factor because it gives a clear voltage signal and is an easy number to make further calculations with. The specific voltage output of a single piezoelectric film is so low that it is difficult to distinguish from noise, or at all. Therefore, the amplification is left in the testing circuit.

The amplifier used is a TL074, with only one of its four operational amplifiers active, effectively operating as a TL071 equivalent. The circuit is powered by two 9 V batteries. Resistor R_2 is part of the amplifier's internal design, while the capacitor and R_4 were included to reduce high-frequency noise and external interference. These components may become redundant after replacing the unshielded wiring with a coaxial cable, but they were retained as a precaution to ensure signal stability.

The voltage over R_3 is measured to determine the output voltage and current of the system. This measurement is performed using an NI USB-6008 data acquisition device connected to LabVIEW on a laptop. The resistance value of R_3 was chosen based on the expected current output of the amplifier, approximately 10 mA.

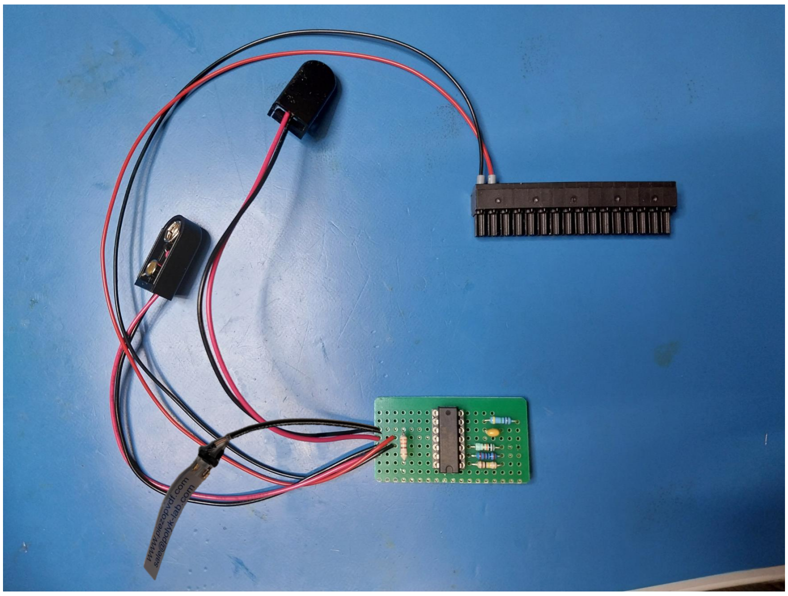

Figure 4.16: Final circuit including the piezoelectric film, amplifier, battery and voltage meter connections

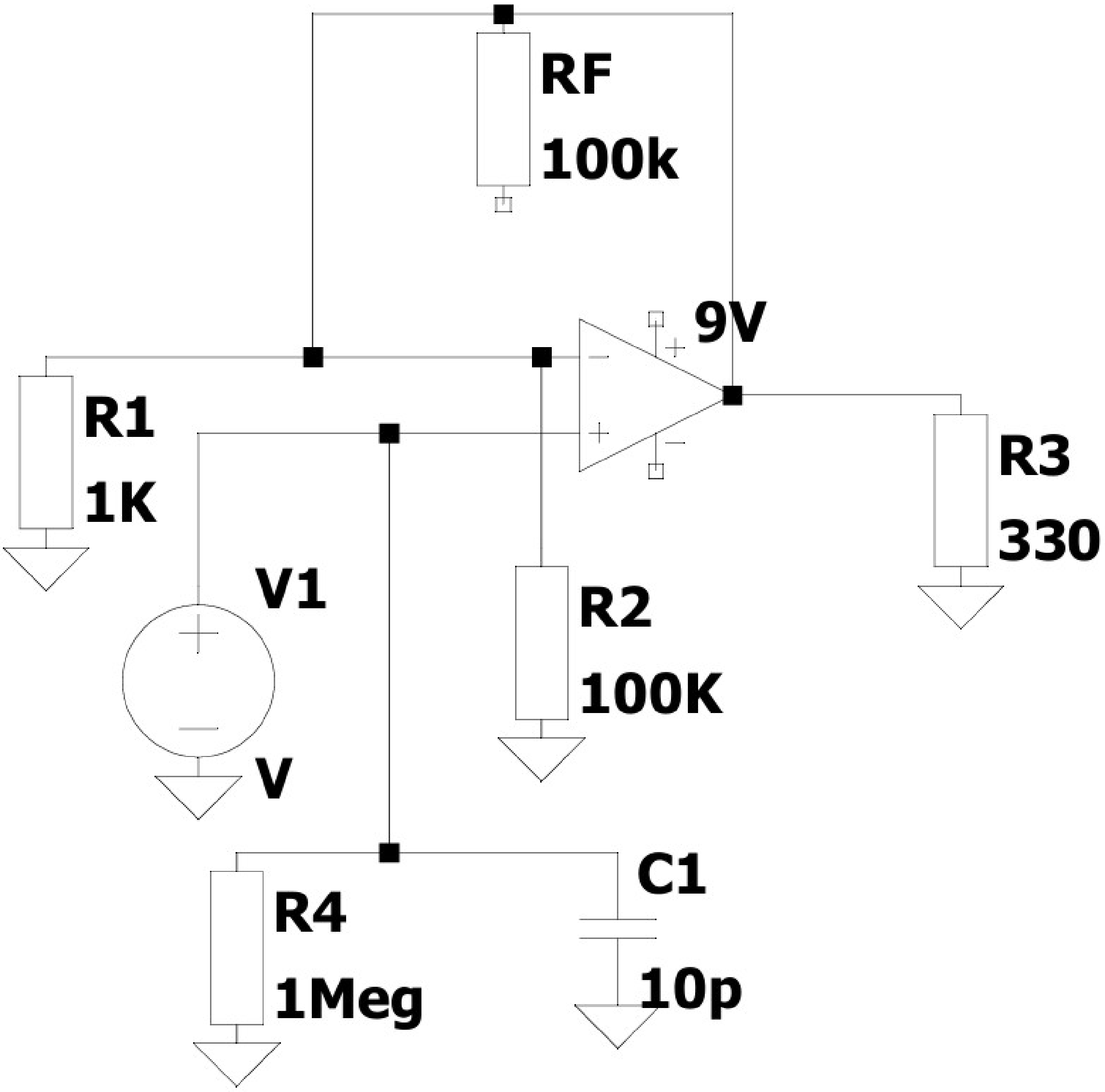

Figure 4.17: Harvesting electrical circuit

For the energy-harvesting experiments, a 1.3 m cable was added between the piezoelectric film and the remaining circuit components to minimise the amount of electronics exposed to water. The PVDF film was attached to the 0.8 mm backbone so that both elements moved together during flapping while allowing relative bending between them (connection method: tape type to be specified). The electrical connection between the film and the circuit was encapsulated in a thin layer of EcoFlex 20 silicone for additional waterproofing. The remaining electronic components—including the perfboard, voltage meter, and data acquisition laptop—were positioned on the bridge above the tank.

Voltage measurements were conducted simultaneously with video recordings for each flow speed. They have not been synchronised since pressing the recording button caused too much interference with the voltage measurements. The LabVIEW system was configured to record voltage data at 1 kHz (sampling interval of 0.001 s) for 30 s per run, resulting in 30,000 data points per measurement. This sampling rate provided sufficient temporal resolution to capture the expected flapping frequency of less than 10 Hz. A baseline (zero-flow) measurement was taken before each run to correct for possible voltage offsets and surrounding noise.

Due to the time-intensive waterproofing process, which required complete resealing of the model for each configuration, only one measurement run was performed per stiffness level and flow condition.

The calibration measurements were performed before putting the setup in the water. The calibration measurement has been performed twice, only when the strut has been moved for the reconstruction of the model.

4.3.2. Energy harvesting results and discussion

The energy harvesting results are presented in Figures 4.21, 4.20, 4.19 and 4.18. These figures show the direct voltage measurements over time. The baseline measurement, which contains noise between –0.14 and 0.2 V, has been subtracted from the signals to ensure that internal system noise does not influence the results.

To verify whether the voltage signals correspond to the flapping motion of the tail, several verification steps were carried out. First, the peak intervals were compared to the flapping frequency obtained from the video recordings. These match within <0.1 Hz, indicating that the peaks are unlikely to originate from tank vibrations or other external sources. Second, the baseline measurements do not show any recurring peaks, only a constant offset. Lastly, the observed voltage peaks are within the expected range: for small deflections no unusually large or small peaks are present.

The voltage measurements are plotted side by side so that three trends are immediately visible. (1) The flapping frequency increases with increasing flume tank power, which is reflected by the increasing number of voltage peaks over time. (2) The amplitude of the voltage peaks increases with increasing tank power. (3) The signal-to-noise ratio improves with tank power.

All of these trends are consistent with expectations. The flapping frequency increases with flume tank power (Figure 4.12), and therefore the voltage peak interval decreases. At higher tank power, the tail exhibits larger flapping amplitudes, which results in higher voltage peaks. The improvement in signal-to-noise ratio is caused by the growth of the voltage peaks: the relative noise contribution becomes smaller for the large peaks in Figure 4.18 compared to the smaller peaks in Figure 4.21. This suggests that the noise is not proportional to tank power and therefore that the measured voltage signals indeed originate from the tail flapping motion.

While the absolute time component of the voltage measurements does not by itself contain meaningful trends, the temporal structure of the signal is highly informative. In particular, the spacing between consecutive voltage peaks provides insight into the tail's dynamic behaviour. By analysing the peak intervals in detail, both the dominant flapping frequency and the characteristic frequencies of the background noise can be determined. This makes the peak-interval analysis a crucial step in confirming that the measured voltage originates from the tail motion rather than from external disturbances such as tank vibrations or electronic artefacts.

A more detailed investigation of the peak intervals across the different flume tank power settings reveals consistent patterns. For each measurement series, the distribution of peak intervals, their variability, and the presence of any secondary frequency components were examined.

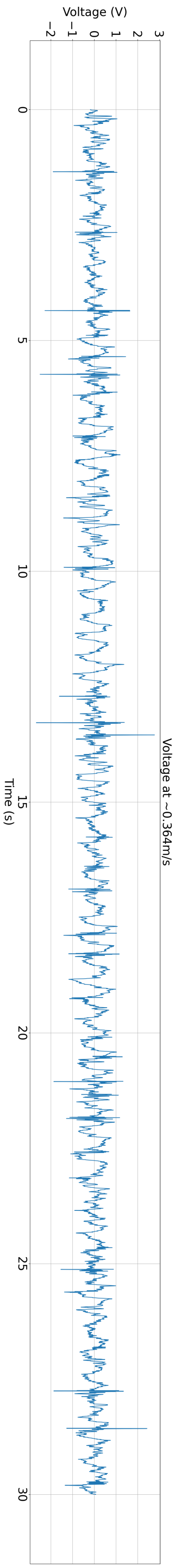

Figure 4.18: Voltage output at 40% power

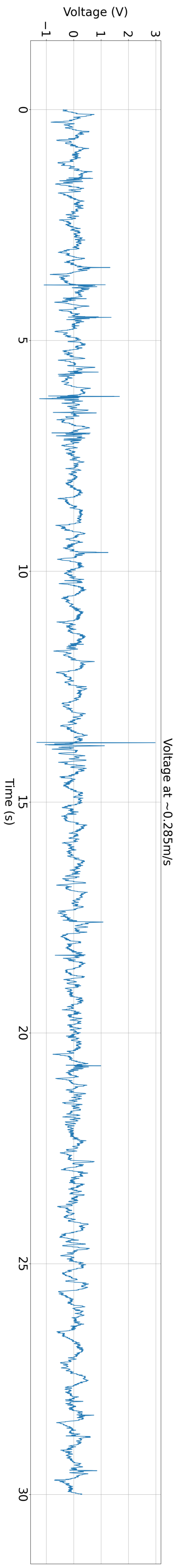

Figure 4.19: Voltage output at 30% power

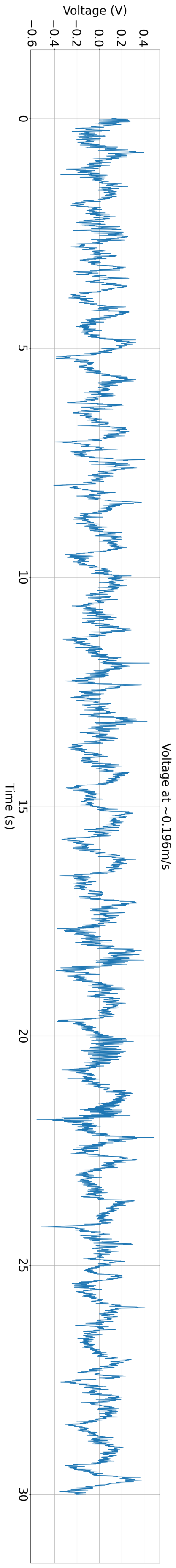

Figure 4.20: Voltage output at 20% power

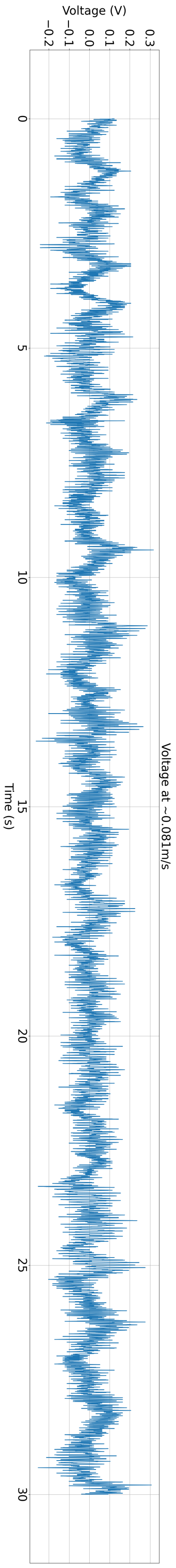

Figure 4.21: Voltage output at 10% power

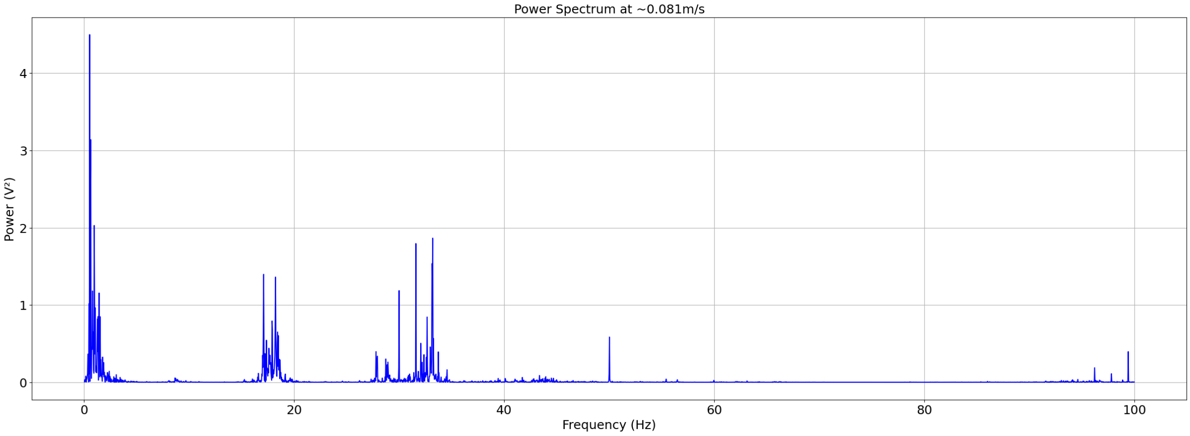

Figure 4.22: Voltage peak FFT plot (0-100Hz) at 10% tank power

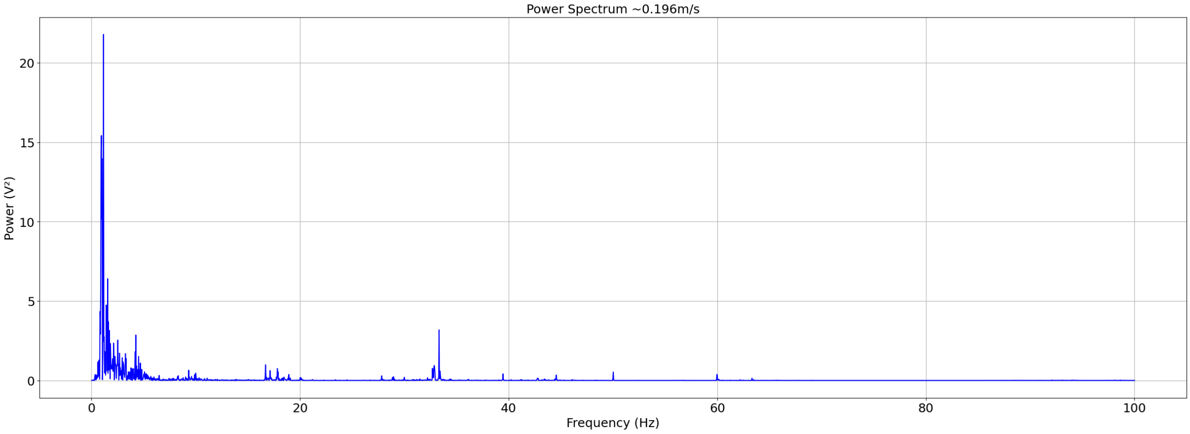

Figure 4.23: Voltage peak FFT plot (0-100Hz) at 20% tank power

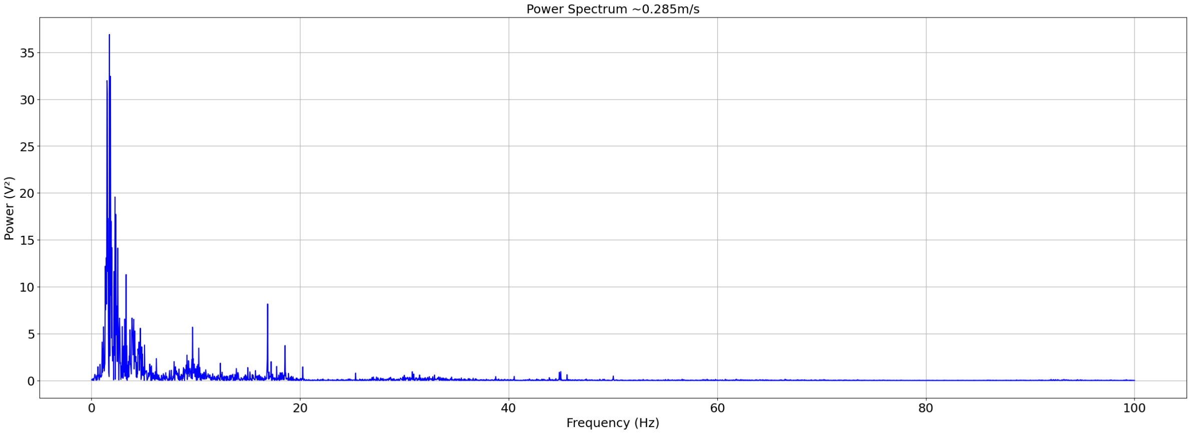

Figure 4.24: Voltage peak FFT plot (0-100Hz) at 30% tank power

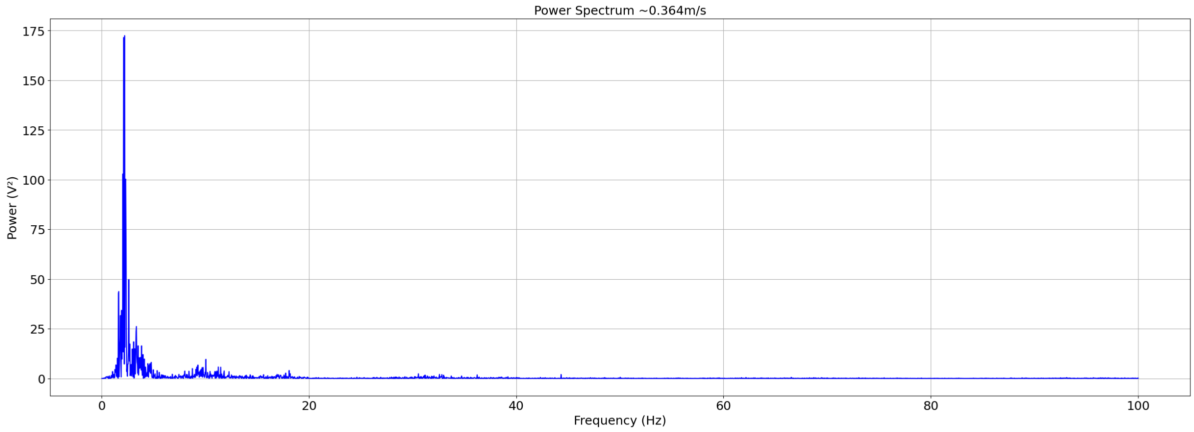

Figure 4.25: Voltage peak FFT plot (0-100Hz) at 40% tank power

Figures 4.22, 4.23, 4.24 and 4.25 present the spectral power distribution of the measured signal. In these plots, the power—defined as the square of the voltage—is represented in the frequency domain, effectively replacing the time axis with the corresponding frequency components. The strong noise signals are significantly far away from the dominant peak, and therefore, the highest power signal is assumed to be dominantly tail flapping related. To ensure that no information is lost, Parseval's theorem is applied, which states that the total energy in the time domain is equal to the total energy in the frequency domain (Equation 4.5). In this analysis, the energy carried by the measured voltage signal is evaluated both in the time domain and in the frequency domain [130].

$$E_{\text{time}} = \sum_{n=0}^{N-1} |x[n]|^2 \, \Delta t \;\approx\; E_{\text{freq}} = \sum_{k=0}^{N-1} |\text{FFT}(x)[k]|^2 \, \frac{\Delta t}{N} \tag{4.5}$$

N is the number of measurement points during the measurement time (from subsection 4.3.1) and $n = 0, 1, 2, ..., N1$. So $x[n]$ is each measured voltage value. This is squared with respect to the power value corresponding to each measurement. Δt is the time between each measurement. The summation is the total energy within the time domain.

The Fourier transformation $FFT[k]$ with $k = 0, 1, 2, ..., N1$ corresponds to the signal strength per frequency. This is squared, similar to the left side, to define the power. The Fourier Transformation needs to be divided by N to scale the results properly. For each graph, Parseval's theorem suffices, and therefore, the FFT plots are considered reliable.

There is only one peak that is relevant for determining the power output from the tail-flapping motion. This peak represents the specific contribution from the relevant frequency range, while excluding noise contributions.

Due to the high sampling resolution (1 kHz) relative to the relevant frequency range (0–3 Hz), and because the tail motion is not perfectly periodic, the dominant peak may appear as multiple nearby peaks. To account for this, the plots have been smoothed into a single peak. The smoothed peak represents the same total power as the original data, corresponding to the area under the curve. As a result, the smoothed peak appears lower in height but wider in shape.

The original and smoothed results are presented in Figures 4.26, 4.27, 4.28, and 4.29. The largest smoothed peak is considered to correspond to the tail-flapping contribution. The width of each smoothed peak is determined, and the area under the graph is calculated. These include specific steps accounting for windowing effects.

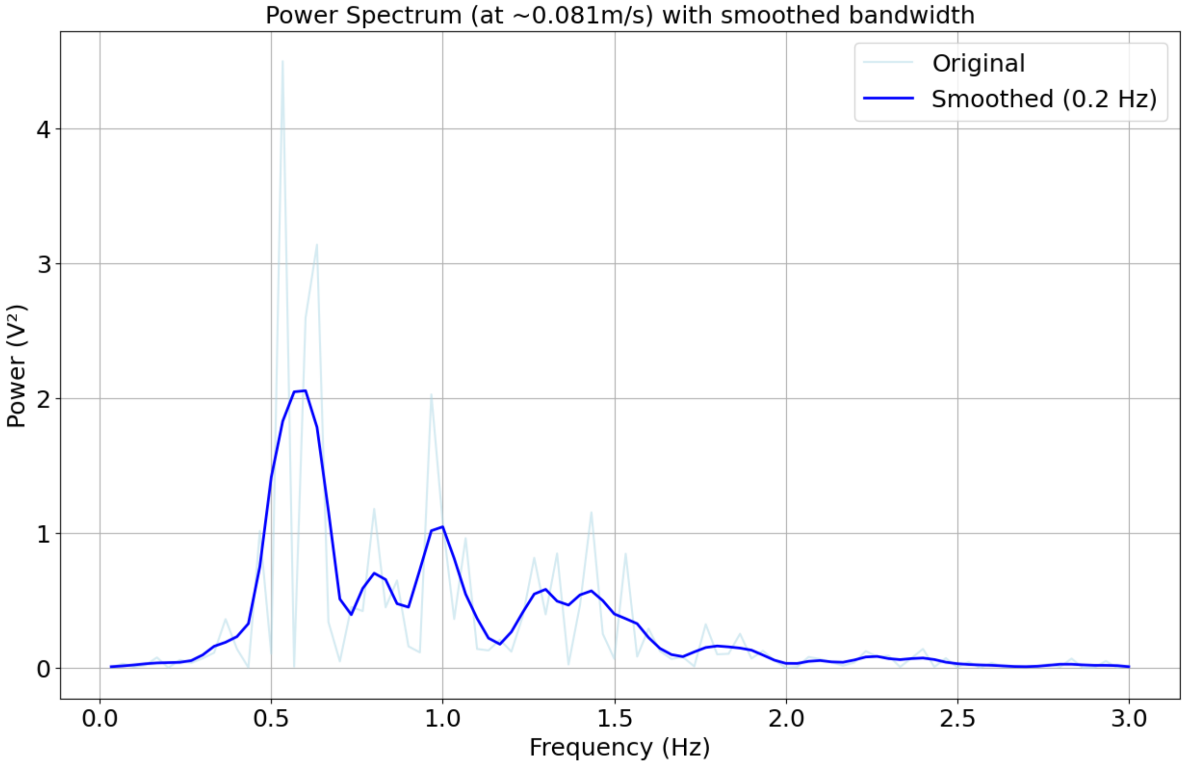

Figure 4.26: Flume tank tail flapping amplitude

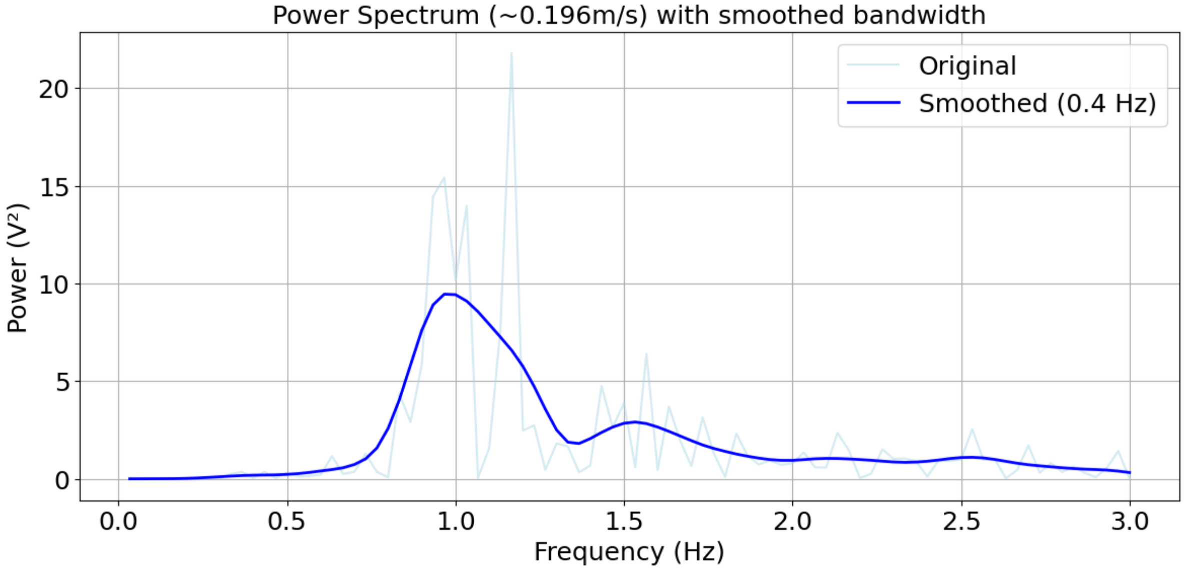

Figure 4.27: Flume tank tail flapping amplitude

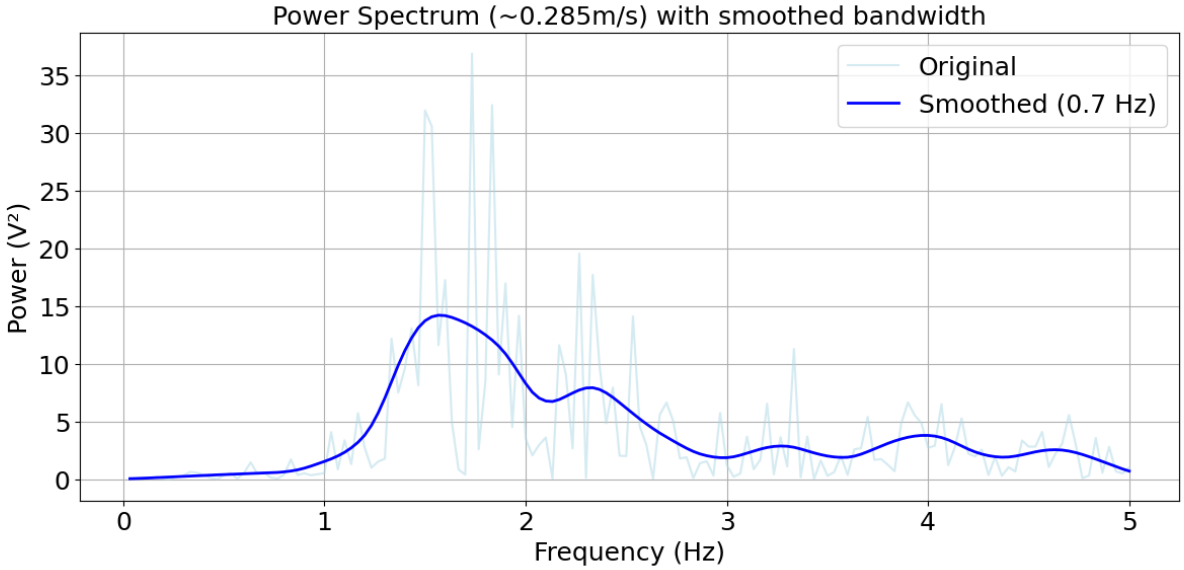

Figure 4.28: Flume tank tail flapping amplitude

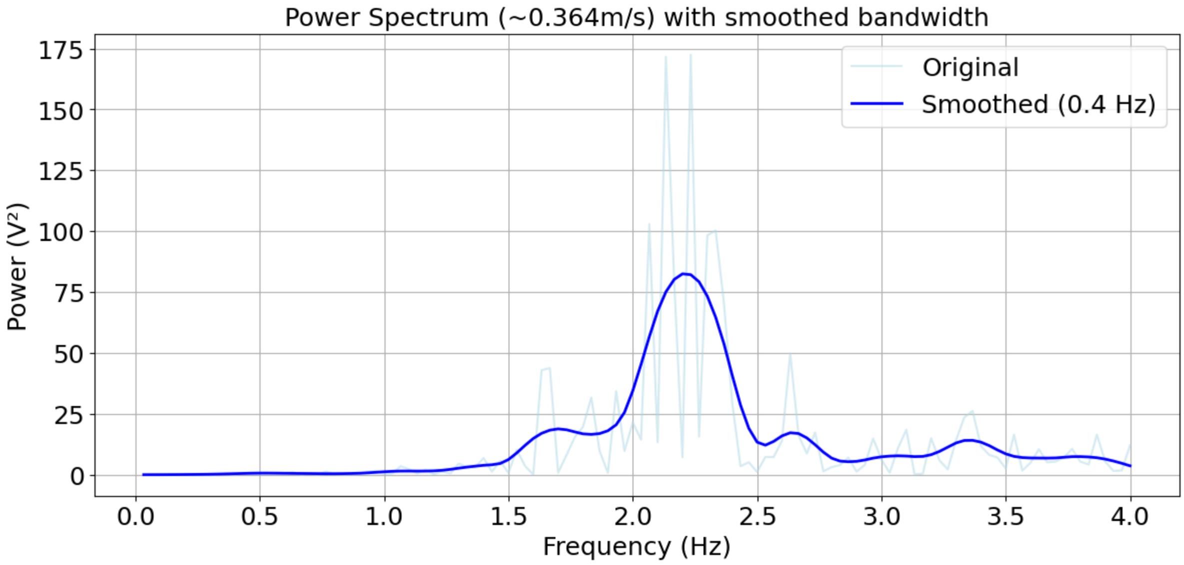

Figure 4.29: Flume tank tail flapping amplitude

To smooth the results, the Hanning window preserves a reasonable main-lobe width, offering a balanced trade-off between leakage suppression and frequency resolution, which is particularly important for accurately resolving the narrowband tail-beat frequencies in this study [131]. This process applies a taper to the signal, reducing abrupt transitions at its boundaries and thereby reducing spectral leakage. Spectral leakage arises when energy from one frequency component spreads into neighbouring frequencies, complicating the accurate identification and quantification of individual spectral components [132]. The Hanning window can be defined as (Equation: 4.6) [133]:

$$w[n] = 0.5\left(1 - \cos\left(\frac{2\pi n}{N-1}\right)\right), \quad n = 0, 1, \ldots, N-1 \tag{4.6}$$

The frequency band for each flumetank power is determined manually and presented in Table 4.3. After windowing the calculated power from the area under the smoothed curve will be underestimated. This is because the process of windowing reduces the amplitude and power of the signal. Therefore, a correction must be applied to ensure that the calculated power is not underestimated [134].

Table 4.3: Manually determined peak bandwidth

Tank power [%]	Bandwidth [Hz]
10	0.42-0.74
20	0.70-1.35
30	1.10-2.10
40	1.80-2.60

The energy in each band can be defined as (Equation: 4.7):

$$E_{\text{band},w} = \sum_{k \in \text{band}} \frac{|X_w[k]|^2}{N} \Delta t \tag{4.7}$$

$|X_w[k]|$ is the power of the windowed graph. Absolute values are taken to account for the negative voltage peaks when moving to either side during the flapping motion. The energy from the band is the windowed energy and needs to be corrected; the correction factor is $1/U$ (Equation: 4.8). Here, U is the average of the windowed power $(w[n]^2)$ over the entire frequency domain. The corrected energy within the specific bandwidth is calculated by applying equation 4.9 [134].

$$U = \frac{1}{N} \sum_{n=0}^{N-1} w[n]^2 \tag{4.8}$$

$$E_{\text{band,corr}} = \frac{E_{\text{band,w}}}{U}, \tag{4.9}$$

The current comping from the piezoelectric film is dependent on the voltage change per time. Therefore the current can be calculated using (Equation: 4.10)[135]:

$$I[n] = C\,\frac{dV}{dt} = C\,\frac{v[n+1] - v[n]}{\Delta t} \tag{4.10}$$

I is the current from the piezoelectric film, and n in this case is the number of measurements within the determined frequency bandwidth. dV/dt is the change in voltage and C is the capacitance. The current from a piezo is generally very low. The currents, within the bandwidths, are given in Table 4.4. The values in this table correspond to the values of a single piezoelectric film, meaning that the values are scaled back (divided by 100) to account for the amplifier.

Table 4.4: Current from the piezoelectric film in the power peak for each flumetank power

Tank power [%]	**Current [A]**
10	9.6×10^{-18}
20	3.2×10^{-18}
30	5.3×10^{-17}
40	5.6×10^{-16}

The power output is a simple equation stated below (Equation 4.11. The values taken in this equation are only within the bandwidth of the peak. The corresponding values are for a single piezoelectric film. The results are presented in Table 4.5

$$P_{\text{inst}}[n] = v[n] \cdot I[n] \tag{4.11}$$

Table 4.5: Power output from a single piezoelectric film from tail flapping movement per flumetank power

Tank power [%]	Power [W]
10	7.8×10^{-8}
20	9.5×10^{-7}
30	2.0×10^{-6}
40	9.0×10^{-6}

The energy harvested from the piezoelectric film is lower than that of the trout-like swimmer (peaking between 18-121μW) by D. Tan et al. [70]. This has two important reasons. First, Tan's design drives the tail against the flow instead of with the flow. This results in a higher oscillation frequency and a larger tail amplitude, which in turn produces larger voltage spikes in the piezoelectric film. Second, the type of piezoelectric material plays a major role. The MFC patch used by D. Tan et al. has a significantly higher capacitance, which leads to a higher current output per voltage spike. As a result, the total harvested power is higher for such piezoelectric films.

Nevertheless, considering that the current system uses a less efficient harvester and is subjected only to a forward flow stream, the obtained harvesting results are still relatively close.

The performance of the underwater robot as an energy harvester is by no means at its highest efficiency, and several improvements can be made (discussed in Chapter 5). However, overall, the performance represents a very strong first step.

4.4. Stiffness test

The stiffness of each tail configuration is determined by performing a stiffness test. This test aims to quantify the force required to bend the tail by at least 10° without including hydrodynamic effects. Only the backbones that have been tested in the flume tank (thicknesses 1, 0.8, and 0.6 mm) are tested here. The stiffness test is based on deflection measurements induced by gravitational forces using weights.

4.4.1. Stiffness test setup and testing

The tail base is mounted on a 1 mm steel plate with holes matching the T-shaped strut. The first rib of the tail fits into these holes, forming a rigid connection to the steel plate. The steel plate is inserted into a slit on a wooden base, which has 180° angles printed on its surface. The 90° angle between the wooden base and the steel plate is ensured by the slit

The wooden base is held upright in a table vise, and both the steel plate and base are levelled to align with gravity. A bubble level is used to confirm that both the wooden base and the steel plate are perfectly aligned with gravity. The setup is shown in Figure 4.30. The tail of the underwater robot is now sideways, bending in the vertical direction. The tail construction includes the interior backbone and the silicone cover, but not the caudal tail. The caudal tail does not contribute to the tail stiffness, and in this test, it will cause an uncertain gravitational moment depending on the deformation of the tail. Therefore, the caudal fin is not included in this test. The tail is weighed before testing. The weights of different parts of the tail are:

- Backbone < 1g (for each thickness)
- 2 middle ribs 7g
- Last rib with screws 6g
- Silicone tail cover 58g
- Total weight 71g

The scale used to weigh the parts is a Kern EMB 2200-2 [136]. This scale has a resolution of 1g, and the uncertainty is dependent on the measuring conditions, but the scale has a linearity of 2g.

The parts of the tail are measured separately because not every component causes the same amount

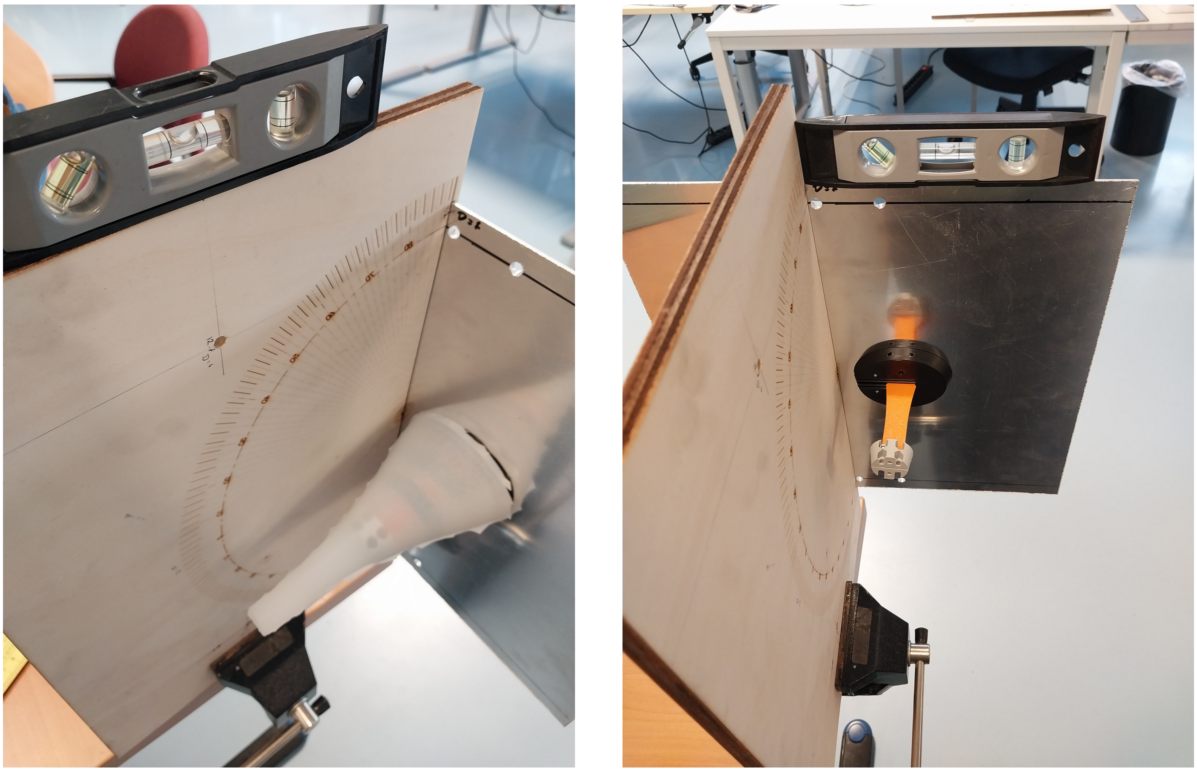

(a) Base calibration **(b)** Plate calibration

Figure 4.30: Stiffness test setup for base and plate calibration

of deflection, depending on where they are on the tail. The biggest force components are the silicone tail cover and the last rib. Therefore, this gravitational force of the weight of the tail itself has been used as the driving gravitational force.

The first rib and screws do not contribute to the force or the stiffness of the system, but ensure a clamped end of the backbone connecting to the front of the underwater robot. The stiffness is determined by the thickness of the backbone and the stiffness and stretching characteristics of the silicone. The silicone is attached to the first rib, the base of the tail, and to the rest of the underwater robot. If the backbone bends, the silicone stretches on one side. The further it stretches, the stiffer it gets.

The starting force due to the weight of the tail itself is taken at 65g. This is an approximation based on the weight of the silicone cover (58g), the last rib (6g) and the minor contributions of the backbone itself and the other 2 ribs (1g). So the starting weight is (equation 4.12):

$$F_g = weight[kg] \times 9.81[m/s^2] = 0.065 \times 9.81 = 0.63765N \tag{4.12}$$

The stiffness test is performed using 5g weights. The deflection of the tail is measured using a 90° angle try square. This way it is possible to read the deflection angle on the wooden base without an offset. The deflection is measured at the tip as it is assumed to be linear. The bending of the silicone is not perfectly linear but the difference is in terms of <0.1mm. The deflection in the end of the tail is taken because that is the deflection used to measure the St number. The weights are placed on the last rib because that is where the actuation force will be applied if the piezoelectric film is placed on the backbone.

The first measurement is without any extra weight and the next measurements are with increments of 5g steps until 30g. Only the lower angles above 10° are measured. This is because it seems realistic that the deflection made by the piezoelectric film will be smaller rather than larger. If larger angles need to be made, the data can be extrapolated.

These results, expressed both as angular and linear deflections, are subsequently used to define the requirements for the actuation circuit (see Section 4.5.1). These results are used for the requirements of the actuation circuit. The force needed to deflect the tail between 10 and 20° needs to be realised by the actuation circuit.

4.4.2. Stiffness test results and discussion

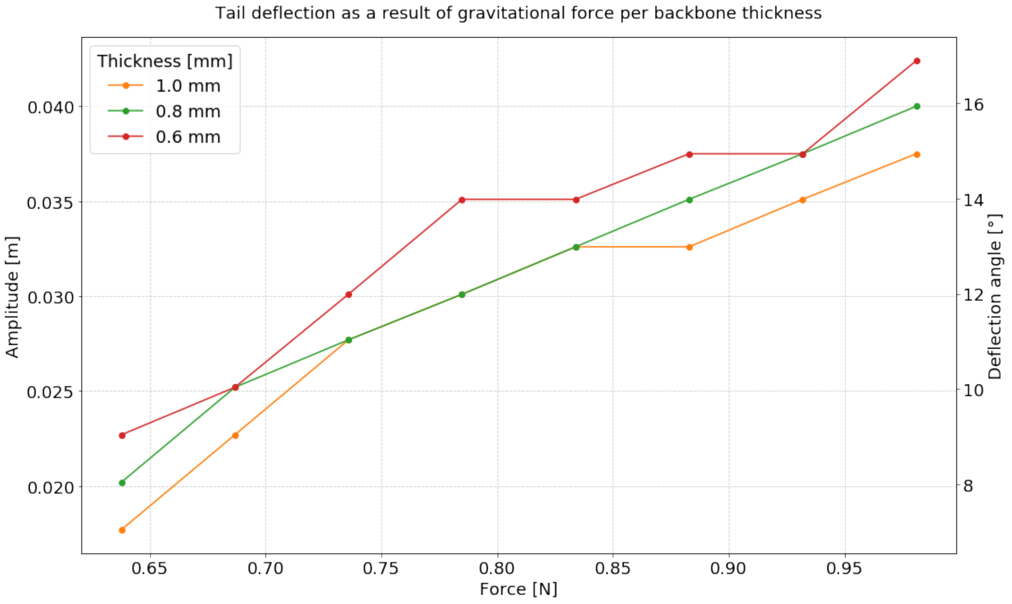

Figure 4.31: Measured deflection from gravitational force per backbone

As expected, the lowest backbone stiffness from Figure 4.31 corresponds to the largest deflection from the same force, and the highest backbone thickness to the smallest deflection. The stiffness results are used to determine the strength needed from the piezoelectric film to actuate the tail in section 4.5.1.

The results are not perfectly linear; this may be caused by the added stiffness of the silicone tail or the shape of the backbone. The force needed to deflect the tail 10°, which is 2.5cm deflection about 0.68N for a backbone thickness of 0.8mm

4.5. Actuation test

The full actuation test has not been performed due to a lack of materials. However, the entire circuit has been developed, and with the information from the datasheet for the piezoelectric film, predictive calculations have been performed, which give a very strong indication of the feasibility of the application.

The actuation circuit has been designed apart from the harvesting circuit for simplicity. The actuation circuit is developed to determine the force in N that can be realised by actuating the piezoelectric film at certain voltages.

4.5.1. Actuation circuit

Piezoelectric films can be actuated at very low current, making the total power needed relatively low. However, in order to actuate piezoelectric materials, a very high voltage is needed. To source such high voltages, a voltage amplifier is needed. Voltage amplifiers come in many shapes and sizes, depending on the requirements of the voltage signal. Voltage amplifiers send voltage signals at a certain maximum frequency and current. This strongly defines the type of amplifier that is needed.

Because the voltage amplifier requirements may vary per piezoelectric product, most piezoelectric materials come with recommended or custom-designed voltage amplifiers. The output force and deflection per setting are specific to each type of piezofilm and can be determined using the datasheet.

However, doing a measurement is necessary to confirm that the piezoelectric film is responding as expected before integrating it in the design.

The circuit is based on the BD300 small amplifier by PiezoDrive [137]. This amplifier needs a 24V source and a 3V source that will be amplified a maximum of 100 times. The piezoelectric film, contrary to the harvesting system, is depicted as a resistor. The full circuit is presented in figure 4.32

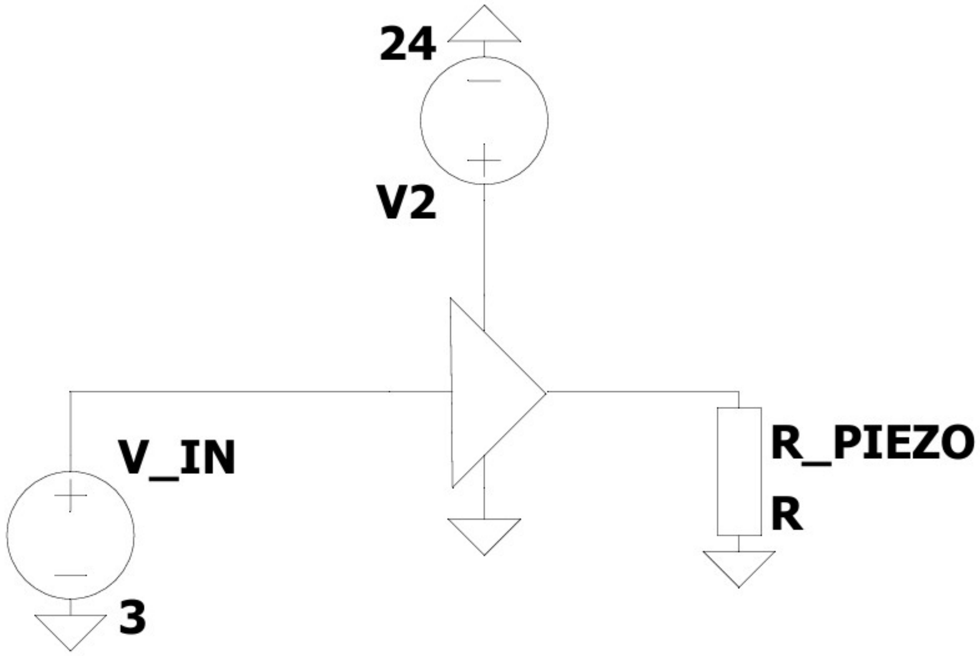

Figure 4.32: Piezoelectric actuation circuit

The circuit has been tested for functionality. Since the voltage is too low to achieve the desired deflection, the test focused on verifying whether the circuit operates correctly and how the piezoelectric film responds. A 3 V voltage source was set to oscillate between -1.5 V and +1.5 V to account for the two directions in which the piezoelectric film can move. The voltage supply was driven with a 2 Hz triangular waveform.

The response of the piezoelectric film was noticeable to some extent: its oscillatory motion corresponded both in shape and in frequency to the applied voltage signal. This was as expected, and therefore the circuit suffices. A similar circuit can be developed for other amplifiers, depending on the amplifier requirements.

4.5.2. Predictive actuation results

The deflection of the piezoelectric film is based on the difference in length of the film according to the given data sheet. The change in length (ΔL) is defined by equation 4.13:

$$\Delta L = d_{33} \times U \tag{4.13}$$

U is the voltage needed to change the length L (50mm) and d_{33} is given in the datasheet as $15pC/N = 15 \times 10^-12m/V$. ΔL can be approximated as (equation 4.14)

$$\Delta L = \frac{\frac{\delta}{L} \times \frac{t}{2}}{d_{33}} \tag{4.14}$$

The deflection (δ), length L and thickness t are in [m]. This equation is derived from $\sin\alpha = \frac{\delta}{L}$. An extreme sketch is given in Figure 4.33.

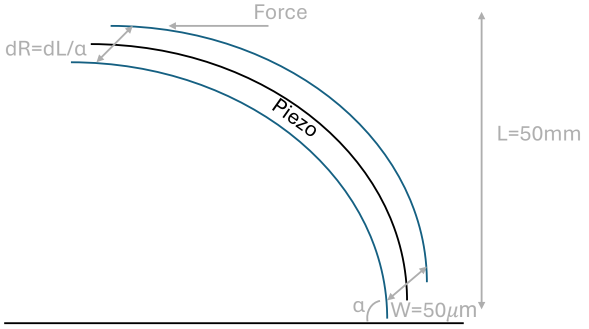

Figure 4.33: Extreme piezoelectric film bending for actuation voltage calculation

Using equations 4.13 and 4.14 and $t = 50\mu m$, the voltage needed to create 1° of bending, causing $\delta = 0.873mm$, resulting in a length change of $\Delta L = 0.000436mm = 0.436\mu m$. The voltage requirement for this bending movement is $U = 29087V = 29kV$.

The mechanical force generated by the piezoelectric film can be estimated using the clamped–free beam approximation. This is justified because the piezoelectric film is fixed at one end in the circuit while the other end is free, making its mechanical behaviour equivalent to that of a cantilever beam. The standard deflection relations for such a beam are shown in Figure 4.34.

Beam type	Slope at free end	Deflection at critical location(s)
a) 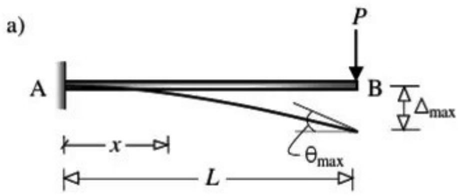	$\theta_{max} = \frac{PL^2}{2EI}$	$\Delta_{max} = \frac{PL^3}{3EI}$

Figure 4.34: Clamped beam deflection equations [138]

For a prescribed tip deflection angle, the corresponding force at the free end can be determined. The deflection angle θ is taken as $10°$, which corresponds to 0.175 rad. The reaction force F is obtained from the standard relation for a clamped beam:

$$F = \frac{\theta\, 2EI}{L^2}, \tag{4.15}$$

where E is the Young's modulus, I is the second moment of area, and L is the beam length.

The second moment of area for a rectangular cross-section is given by

$$I = \frac{bh^3}{12},$$

which evaluates to

$$I = 1.05 \times 10^{-4} \text{ mm}^4$$

for a film width of $b = 10$ mm and thickness $h = 50$ μm $= 0.05$ mm.

The material stiffness of the piezoelectric film is taken as

$$E = 2200 \text{ N/mm}^2,$$

and the film length is

$$L = 50 \text{ mm}.$$

Substituting these values into Equation 4.15 yields the reaction force corresponding to a $10°$ tip deflection. The resulting force produced by a single piezoelectric film is

$$F = 32\ \mu\text{N}.$$

This represents the mechanical loading capacity of the film when driven to the specified angular displacement.

5

Discussion and conclusion

The preceding chapters have presented the development, implementation, and experimental validation of a piezoelectric-based actuation and energy harvesting system for a soft underwater robot. This chapter critically evaluates the feasibility of the proposed system, reflects on the performance outcomes, and discusses the broader implications of using piezoelectric materials in dual-mode underwater robotics. The analysis integrates experimental findings with theoretical considerations to assess whether piezoelectrics can realistically replace conventional actuation technologies while simultaneously enabling onboard energy harvesting.

In addition, this chapter examines the trade-off between system simplicity and efficiency, identifying where increased design complexity becomes necessary to achieve meaningful performance gains. Finally, future design requirements are formulated based on the technological limitations encountered in this work, the insights gained from the literature, and the expected direction of further research. Together, these discussions provide a comprehensive evaluation of the current design and outline the essential steps required to advance the concept toward a functional and efficient dual-mode underwater robotic system.

5.1. Feasibility evaluation of actuation and harvesting system

The results presented in Chapter 4 are based on the final prototype design and the performance of a single piezoelectric film. As expected, a single film is not sufficient to harvest meaningful amounts of energy or to actuate the tail. However, the system's performance can be scaled by incorporating multiple piezoelectric films. Such scaling can be implemented either in series or in parallel, which affects the resulting voltage (input or output), current (input or output), and the overall mechanical stiffness of the system.

This section evaluates whether it is feasible to replace the electromotor used in the original design by S. C. van den Berg et al. [65] with a fully piezoelectric actuation system. Furthermore, the harvesting potential of the system is assessed to determine whether it can realistically charge a battery that subsequently powers the actuation mechanism within an acceptable time span.

5.1.1. Actuation feasibility

The piezoelectric film used in this research is not an efficient actuator. These predictive calculations do not take into account that the amplifier required to drive this type of piezoelectric film is too large for the system. Future implementations should consider alternative material configurations that require a lower actuation voltage while maintaining comparable performance.

Figure 5.1 illustrates the difference between series and parallel connections. In series, the total input voltage is the sum of the voltages required for each piezoelectric film, while the input current equals that of a single film. The output voltage adds the contributions of all films, with the output current of a single film. In parallel, the input voltage equals that of a single film, while the input current is the sum of the currents of all films. Similarly, the output voltage corresponds to a single film, and the output current is the sum of all individual currents.

To reach a mechanical force of $0.68N$ there must be multiple piezoelectric films bending in the same direction. These have to be connected in parallel. Since all piezoelectric materials require high voltages for actuation it is not feasible to have piezoelectric films as actuators connected in series. This would require an excessively high voltage. The force improvement is linear to the number of films added (Equation 5.1).

$$N = \frac{F_{stiffness}}{F_{piezo}} = \frac{0.68N}{0.000032N} = 21250 \tag{5.1}$$

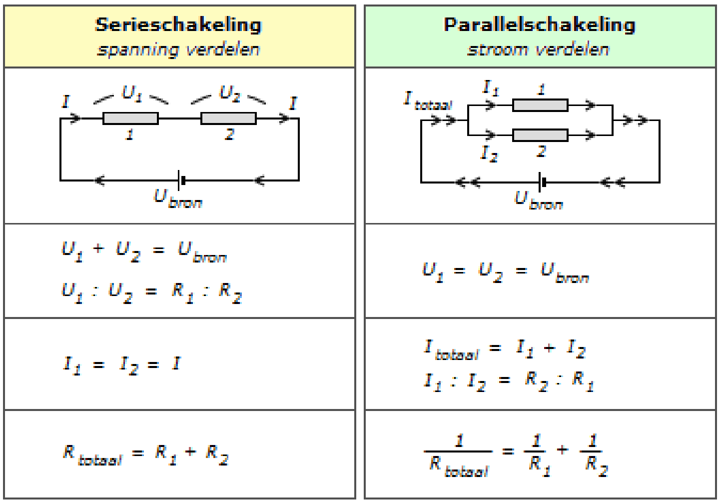

Serieschakeling *spanning verdelen*	**Parallelschakeling** *stroom verdelen*
$U_1 + U_2 = U_{bron}$ $U_1 : U_2 = R_1 : R_2$	$U_1 = U_2 = U_{bron}$
$I_1 = I_2 = I$	$I_{totaal} = I_1 + I_2$ $I_1 : I_2 = R_2 : R_1$
$R_{totaal} = R_1 + R_2$	$\frac{1}{R_{totaal}} = \frac{1}{R_1} + \frac{1}{R_2}$

Figure 5.1: Series or parallel connections [139]

To realise a force of 0.68N by adding piezoelectric films which are $50\mu m$ thick, this would result in a thickness of 1.0625m. This does not fit in the underwater robot. Realistically, the thickness should be reduced at least 10 times. There are 2 main ways to improve the required thickness. Either the piezoelectric material should have a higher stiffness without requiring too much voltage. Another way is for the underwater robot to have a less stiff structure without becoming unstable or inefficient.

5.1.2. Harvesting feasibility

The charging requirements of a battery depend on the battery itself and its capacity [Ah] [140]. The voltage required to charge a battery is typically similar to the nominal voltage of the battery.

The average voltage output of a single piezoelectric film in the tail is approximately 0.006 V. To reach 24 V, which is a realistic voltage requirement for an amplifier source, around 4000 piezoelectric films would need to be connected in series. This corresponds to a total thickness of 20 cm, which would not fit within the tail. Adding this many films would increase the stiffness, but the resulting stiffness would still not exceed that of the current backbone. Therefore, this increase in stiffness could be mitigated.

It is important to note that in harvesting mode, piezoelectric films generate positive or negative voltage depending on the bending direction. To achieve a desired voltage, each individual film must bend in the same direction; otherwise, the voltage contributions may partially cancel, reducing the total harvested voltage.

This requirement significantly complicates the system. Furthermore, piezoelectric films connected in series for energy harvesting cannot simultaneously be used for actuation without introducing additional circuit complications.

However, the voltage output of the piezoelectric film is the least limiting factor. As shown in Table 4.4, the output current of a single piezoelectric film is extremely low. To charge a fast-charging battery (with a capacity ≤ 10Ah), the current must be at least 0.05A [140]. This implies that the number of piezoelectric films required in parallel would not physically fit within the underwater robot. With a low battery capacity and low current, the charging time of such a battery would be at least a week (approximately 200 hours/ 9 days), assuming the maximum power output at the highest flow speed.

To address the current limitation, significant measures are required to improve the system's power output. The tail flapping motion must be greatly enhanced, since the output current depends on the voltage, which in turn is directly related to the flapping amplitude (Eq. 4.13). Furthermore, the piezoelectric material should have a higher capacitance, such as the MFC used by D. Tan et al. which is at least 2 times as large [70, 91].

A low battery capacity also implies that the underwater robot would need to recharge frequently. Ideally, the robot could recharge a battery with a larger capacity; however, this consideration is not addressed in the current analysis.

Based on the current design and piezoelectric system, it can be concluded that piezoelectrics cannot simultaneously charge and actuate a soft underwater robot. The output current of the system is too low. This project represents a very preliminary stage of piezoelectric application research, and there are multiple ways to improve both harvesting and actuation efficiency. However, the main limitation remains the inherent efficiency of the piezoelectric materials. Commercially available and affordable piezoelectric films are not efficient enough to power a standard battery, neither under extreme bending conditions nor with the flapping motion exhibited by the final design. Additionally, these materials are not strong enough to actuate a flexible system without requiring prohibitively high voltage and power.

5.2. Simplicity and efficiency trade-off

The objective of this research is to develop a system that is both simple and efficient. However, operation in dual modes inherently introduces complexity, and prioritising simplicity may reduce overall performance efficiency. This section evaluates whether maintaining a minimalistic system design is advantageous or if increasing the system's complexity can lead to significantly improved efficiency. By analysing the trade-offs between simplicity and performance, the optimal balance for the actuation and energy harvesting system is determined.

Table 2.1 presents the differences between the two operational modes. A simplified system is unable to fully satisfy the requirements for both modes simultaneously. Consequently, an increased level of complexity is necessary to account for variations in angle of attack and stiffness characteristics. Furthermore, the optimal placement of the piezoelectric film is mode-dependent and cannot be confined to a single location within the underwater robot. This additional complexity appears essential to achieve a significant improvement in efficiency, making the potential increase in maintenance requirements and design challenges justifiable in light of the efficiency gains.

The optimal balance between system complexity and efficiency is illustrated in Figure 5.2. The current design is positioned in the lower left corner, where low complexity corresponds to low efficiency. Enhancing efficiency requires an increase in system complexity.

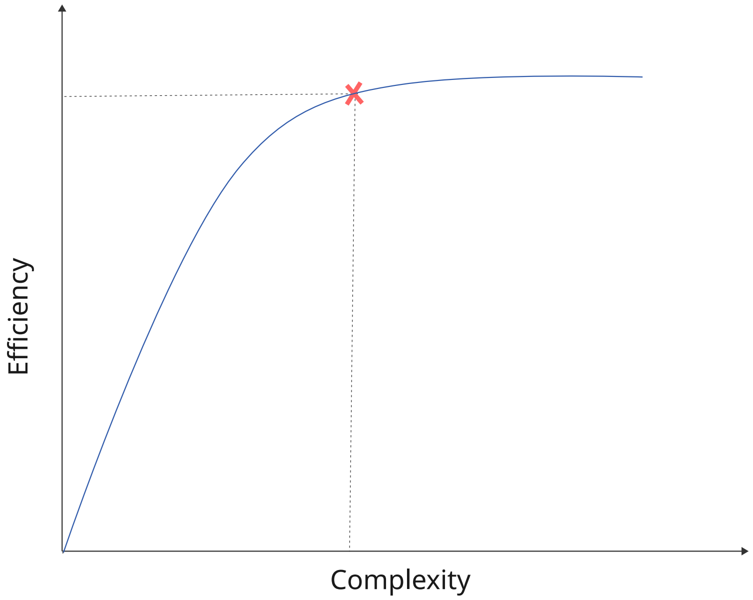

Figure 5.2: Optimal trade-off between efficiency and complexity.

Identifying the optimal trade-off within design research is inherently challenging, and design outcomes may not always follow the path suggested in Figure 5.2. Nevertheless, for the current concept and system, introducing additional complexity is necessary to achieve higher efficiency in further development.

5.3. Future design requirements

There are two main directions for improving the final design. First, piezoelectric applications for larger robots, such as the current system, must be enhanced in terms of efficiency and tailored for specific functionalities. Second, the mechanical design structure must be optimised to achieve the appropriate motion characteristics for each operational mode

Future structural design requirements are derived from the results of the literature review (Table 2.1). A key structural improvement that can significantly enhance the efficiency of the design is the implementation of tunable stiffness. This approach has been highlighted in studies on fish-like propulsion for underwater robots to improve swimming efficiency. In the context of the current design, tunable stiffness primarily addresses the stiffness and angle-of-attack requirements associated with the different operational modes.

The ability to adjust stiffness for each mode provides the opportunity to achieve the desired efficiency parameters, which have not been fully realised in the current design. Ultimately, implementing mode-specific tunable stiffness could further optimise performance and increase efficiency for each operational mode.

For dual-mode applications, piezoelectric materials—or smart materials in general—must be specifically developed to accommodate both operational modes. Currently, most commercial applications are optimised for a single mode, which negatively affects the overall performance of the system. Furthermore, the intrinsic efficiency of piezoelectric materials requires improvement. These enhancements are largely dependent on industry developments and may not progress simultaneously.

Ultimately, a piezoelectric system adapted from commercial technologies should be tailored specifically to the current application. Such a tailored system has the potential to improve overall performance efficiency while potentially reducing the additional complexity associated with multi-mode operation.

The design process presented here was conducted over a relatively short timespan. Design research generally benefits from an extensive iterative process spanning multiple years and fields of expertise [120], and the same applies to this work. Future designs would benefit substantially from additional iterations of the Double Diamond method (Figure 3.1), both within each diamond and across both diamonds. Furthermore, the design process would be greatly enhanced by interdisciplinary collaboration between electrical engineering, mechanical engineering, and soft robotics, enabling the integration of specific design systems from an early stage.

The future design requirements underscore the need for both material and structural innovations. Enhancing the efficiency and functionality of piezoelectric or other smart materials, in combination with mode-specific tunable stiffness, is essential to meet the operational demands of dual-mode underwater robots. These requirements highlight that achieving optimal performance necessitates a holistic approach, integrating advances in material science, mechanical design, and interdisciplinary collaboration. Implementing these targeted improvements will form the foundation for subsequent iterations and enable the development of a more capable, efficient, and adaptable soft robotic system.

References

[1] Stephen C.L. Watson et al. “The global impact of offshore wind farms on ecosystem services”. In: *Ocean and Coastal Management* 249 (2024). DOI: `10.1016/j.ocecoaman.2024.107023`.

[2] Tara Hooper, Nicola Beaumont, and Caroline Hattam. “The implications of energy systems for ecosystem services: A detailed case study of offshore wind”. In: *Renewable and Sustainable Energy Reviews* 70 (2017). DOI: `10.1016/j.rser.2016.11.248`.

[3] D. Benkort et al. *How Do Offshore Wind Farms Affect the Ocean?* Frontiers for Young Minds. 2025. URL: `https://kids.frontiersin.org/articles/10.3389/frym.2024.1336535` (visited on 11/12/2025).

[4] Ian F. Spellerberg. *Monitoring Ecological Change*. 2nd ed. Lincoln University, New Zealand: Cambridge University Press, 2005.

[5] David Grémillet et al. “Robots in ecology: welcome to the machine”. In: *Open Journal of Ecology* 2.2 (2012), pp. 49–57. DOI: `10.4236/oje.2012.22006`. URL: `https://hal.science/hal-00706870`.

[6] NOS. *’Zeeuwse Freek Vonk’ (19) ontdekt nieuwe vissoort in Nederland*. 2025. URL: `https://nos.nl/artikel/2585981-zeeuwse-freek-vonk-19-ontdekt-nieuwe-vissoort-in-nederland` (visited on 11/09/2025).

[7] Kris Havstad and Jeffrey Herrick. “Long-Term Ecological Monitoring”. In: *Arid Land Research and Management* 17 (Nov. 2010). DOI: `10.1080/713936102`.

[8] W. Yang. *Condition monitoring of offshore wind turbines*. 2016. DOI: `10.1016/B978-0-08-100779-2.00018-0`.

[9] NASA. *The Ocean and Climate Change*. 2025. URL: `https://science.nasa.gov/earth/explore/the-ocean-and-climate-change/` (visited on 10/22/2025).

[10] Aditi Raj and Atul Thakur. “Fish-inspired robots: design, sensing, actuation, and autonomy—a review of research”. In: *Bioinspiration Biomimetics* 11.3 (Apr. 2016), p. 031001. DOI: `10.1088/1748-3190/11/3/031001`. URL: `https://dx.doi.org/10.1088/1748-3190/11/3/031001`.

[11] G. Picardi et al. “Bioinspired underwater legged robot for seabed exploration with low environmental disturbance”. In: *Science Robotics* 5.42 (2020), eaaz1012. DOI: `10.1126/scirobotics.aaz1012`. eprint: `https://www.science.org/doi/pdf/10.1126/scirobotics.aaz1012`. URL: `https://www.science.org/doi/abs/10.1126/scirobotics.aaz1012`.

[12] BlueRobotics. *BlueROV2*. 2025. URL: `https://bluerobotics.com/store/rov/bluerov2/` (visited on 10/22/2025).

[13] Woods Hole Oceanographic Institution. *REMUS 600*. 2025. URL: `https://www2.whoi.edu/site/osl/vehicles/remus-600/` (visited on 10/22/2025).

[14] GlobeNewsWire. *Offshore Remotely Operated Vehicle (ROV) Market Report 2025-2035 | Expanding Deepwater Exploration Boosts ROV Demand / High Capital Costs Restrain Smaller ROV Providers*. 2025. URL: `https://www.globenewswire.com/news-release/2025/07/09/3112377/0/en/Offshore-Remotely-Operated-Vehicle-ROV-Market-Report-2025-2035-Expanding-Deepwater-Exploration-Boosts-ROV-Demand-High-Capital-Costs-Restrain-Smaller-ROV-Providers.html` (visited on 10/22/2025).

[15] SeaBear. *An advanced YUCO micro AUV*. 2025. URL: `https://seaber.fr/` (visited on 10/22/2025).

[16] Y. Liu, M.Hajj, and Y.Bao. “Review of robot-based damage assessment for offshore wind turbines”. In: *Renewable and Sustainable Energy Reviews* 158 (2022). DOI: `10.1016/j.rser.2022.112187`.

[17] Jixin Liu et al. "A review of underwater docking and charging technology for autonomous vehicles". In: *Ocean Engineering* 297 (2024), p. 117154. ISSN: 0029-8018. DOI: `https://doi.org/10.1016/j.oceaneng.2024.117154`. URL: `https://www.sciencedirect.com/science/article/pii/S0029801824004918`.

[18] Paul Phamduy, Jayhwan Cheong, and Maurizio Porfiri. "An Autonomous Charging System for a Robotic Fish". In: *IEEE/ASME Transactions on Mechatronics* 21 (Dec. 2016), pp. 1–1. DOI: `10.1109/TMECH.2016.2582205`.

[19] Feng Lyu, Tianhao Cai, and Fushi Huang. "A universal wireless charging platform with novel bulged-structure transmitter design for multiple heterogeneous autonomous underwater vehicles (AUVs)". In: *IET Power Electronics* 16.13 (), pp. 2162–2177. DOI: `https://doi.org/10.1049/pel2.12536`. URL: `https://ietresearch.onlinelibrary.wiley.com/doi/abs/10.1049/pel2.12536`.

[20] Rijkswaterstaat. *HKZ Windpark Noord*. 2025. URL: `https://waterinfo.rws.nl/publiek/stroming/HKZ-Windpark-Noord%28HKZWN%29/details` (visited on 11/12/2025).

[21] "A review of progress and challenges in flapping foil power generation". In: *Progress in Aerospace Sciences* 67 (2014), pp. 2–28. ISSN: 0376-0421. DOI: `https://doi.org/10.1016/j.paerosci.2013.11.001`.

[22] Qing Xiao and Qiang Zhu. "A review on flow energy harvesters based on flapping foils". In: *Journal of Fluids and Structures* 46 (2014), pp. 174–191. ISSN: 0889-9746. DOI: `https://doi.org/10.1016/j.jfluidstructs.2014.01.002`. URL: `https://www.sciencedirect.com/science/article/pii/S0889974614000140`.

[23] Salma Sherbaz and Wenyang Duan. "Propeller efficiency options for green ship". In: 2012, pp. 155–161. DOI: `10.1109/IBCAST.2012.6177547`. URL: `https://www.scopus.com/inward/record.uri?eid=2-s2.0-84860854916&doi=10.1109%5C%2fIBCAST.2012.6177547&partnerID=40&md5=678c2989a688aafbc29969a50689d931`.

[24] Pritam Majumder and Subhendu Maity. "A critical review of different works on marine propellers over the last three decades". In: *Ships and Offshore Structures* 18.3 (2023), pp. 391–413. DOI: `10.1080/17445302.2022.2058767`. URL: `https://www.scopus.com/inward/record.uri?eid=2-s2.0-85129742266&doi=10.1080%5C%2f17445302.2022.2058767&partnerID=40&md5=50e28ad44ca9df2640eddc2dd3abd886`.

[25] Frank Fish, Laurens Howle, and M. Murray. "Hydrodynamic flow control in marine mammals". In: *Integrative and comparative biology* 48 (Dec. 2008), pp. 788–800. DOI: `10.1093/icb/icn029`.

[26] Alpha motor inc. *EV Vs. ICE: Fewer Moving Parts, Less Maintenance*. URL: `https://www.alphamotorinc.com/about/ev-vs-ice-fewer-moving-parts-less-maintenance#:~:text=The%20reduced%20number%20of%20moving,vehicles%20in%20today's%20automotive%20market.` (visited on 11/13/2025).

[27] Huanyu Ou et al. "Investigation of self-adjusting cooling system for the autonomous underwater vehicle propulsion motor". In: *Applied Thermal Engineering* 238 (2024), p. 121972. ISSN: 1359-4311. DOI: `https://doi.org/10.1016/j.applthermaleng.2023.121972`. URL: `https://www.sciencedirect.com/science/article/pii/S135943112302001X`.

[28] Paul Chapman, Warren Viant, and Mitchell Munoko. "Constructing Real-Time Immersive Marine Environments for the Visualization of Underwater Archaeological Sites". In: Apr. 2004.

[29] Yueping Wang et al. "A biorobotic adhesive disc for underwater hitchhiking inspired by the remora suckerfish". In: *Science Robotics* 2.10 (2017), eaan8072. DOI: `10.1126/scirobotics.aan8072`. eprint: `https://www.science.org/doi/pdf/10.1126/scirobotics.aan8072`. URL: `https://www.science.org/doi/abs/10.1126/scirobotics.aan8072`.

[30] M. Hernando, A. Brunete, and E. Gambao. "ROMERIN: A Modular Climber Robot for Infrastructure Inspection". In: *IFAC-PapersOnLine* 52.15 (2019). 8th IFAC Symposium on Mechatronic Systems MECHATRONICS 2019, pp. 424–429. ISSN: 2405-8963. DOI: `https://doi.org/10.1016/j.ifacol.2019.11.712`. URL: `https://www.sciencedirect.com/science/article/pii/S2405896319317045`.

[31] Siqi Wang et al. “Detachment of the remora suckerfish disc: Kinematics and a bio-inspired robotic model”. In: *Bioinspiration Biomimetics* 15 (Aug. 2020), p. 056018. DOI: `10.1088/1748-3190/ab9418`.

[32] Pengfei Zhang et al. “Development and Control of a Bioinspired Robotic Remora for Hitchhiking”. In: *IEEE/ASME Transactions on Mechatronics* 27.5 (2022), pp. 2852–2862. DOI: `10.1109/TMECH.2021.3119022`.

[33] Junqiang Zhang et al. “Optimal selection of time windows for preventive maintenance of offshore wind farms subject to wake losses”. In: *Wind Energy* 26 (Sept. 2023), n/a–n/a. DOI: `10.1002/we.2815`.

[34] Don Stevens. “Buoyancy, Locomotion, and Movement in Fishes: An Introduction”. In: 2011.

[35] Michael Triantafyllou, George Triantafyllou, and Dick Yue. “Hydrodynamics of fishlike swimming”. In: *Annual Review of Fluid Mechanics* 32 (2000), pp. 33–53. DOI: `10.1146/annurev.fluid.32.1.33`.

[36] T. Yao-Tsu Wu. “Hydromechanics of swimming propulsion. part 1. Swimming of a two-dimensional flexible plate at variable forward speeds in an inviscid fluid”. In: *Journal of Fluid Mechanics* (1970).

[37] Frank E Fish. “The myth and reality of Gray’s paradox: implication of dolphin drag reduction for technology”. In: *Bioinspiration Biomimetics* 1 (2006). DOI: `10.1088/1748-3182/1/2/R01`.

[38] Frank E. Fish et al. “Measurement of hydrodynamic force generation by swimming dolphins using bubble DPIV”. In: *Journal of Experimental Biology* 217 (2014), pp. 252–260. DOI: `10.1242/jeb.087924`.

[39] Rahul Bale et al. “Gray’s paradox: A fluid mechanical perspective”. In: *Nature* 4 (2014). DOI: `10.1038/srep05904`.

[40] David E.Rival. *Biological and Bio-Inpsired Fluid Dynamics*. Springer, 2022.

[41] Frank E Fish. “Advantages of aquatic animals as models for bio-inspired drones over present AUV technology”. In: *Bioinspiration Biomimetics* 15 (2020). DOI: `10.1088/1748-3190/ab5a34`.

[42] Daniel B Quinn and George V Lauder. “Tunable stiffness in fish robotics: mechanisms and advantages”. In: *Bioinspiration Biomimetics* 17 (2021). DOI: `10.1088/1748-3190/ac3ca5`.

[43] Graham K. Taylor, Robert L. Nudds, and Adrian L. R. Thomas. “Flying and swimming animals cruise at a Strouhal number tuned for high power efficiency”. In: *Nature* (2003).

[44] J Rohr et al. “Observations of Dolphin Swimming Speed and Strouhal Number”. In: *Space and Naval Warfare Systems Center Technical Report 1769* (1998).

[45] Promode R. Bandyopadhyay. “Maneuvering Hydrodynamics of Fish and Small Underwater Vehicles1”. In: *Integrative and Comparative Biology* 42.1 (Feb. 2002), pp. 102–117.

[46] G.S. Triantafyllou, M.S. Triantafyllou, and M.A. Grosenbaugh. “Optimal Thrust Development in Oscillating Foils with Application to Fish Propulsion”. In: *Journal of Fluids and Structures* 7.2 (1993), pp. 205–224. ISSN: 0889-9746. DOI: `https://doi.org/10.1006/jfls.1993.1012`.

[47] Marin Lauber, Gabriel Weymouth, and Georges Limbert. “Rapid flapping and fibre-reinforced membrane wings are key to high-performance bat flight”. In: *Journal of the Royal Society, Interface* 20 (Nov. 2023), p. 20230466. DOI: `10.1098/rsif.2023.0466`.

[48] Jr Victor C. Sambilay. “Interrelationships between swimming speed, caudal fin aspect ratio and body length of fishes”. In: *Fishbyte* (1990).

[49] Andhini N. Zurman-Nasution, Bharathram Ganapathisubramani, and Gabriel D. Weymouth. “Fin sweep angle does not determine flapping propulsive performance”. English. In: *Journal of the Royal Society Interface* 18.178 (2021). ISSN: 1742-5689. DOI: `10.1098/rsif.2021.0174`.

[50] Tyler N. Wise, Margot A. B. Schwalbe, and Eric D. Tytell. “Hydrodynamics of linear acceleration in bluegill sunfish, Lepomis macrochirus”. In: *Journal of Experimental Biology* (2018).

[51] Kevin T. Du Clos et al. “Thrust generation during steady swimming and acceleration from rest in anguilliform swimmers”. In: *Journal of Experimental Biology* 222 (2019).

[52] Daniel B Quinn, George V Lauder, and Alexander J Smits. “Flexible propulsors in ground effect”. In: *Bioinspiration Biomimetics* 9 (2014). DOI: `10.1088/1748-3182/9/3/036008`.

[53] Qiang Zhong and Daniel B Quinn. “Streamwise and lateral maneuvers of a fish-inspired hydrofoil”. In: *Bioinspiration Biomimetics* 16 (2021). DOI: `10.1088/1748-3190/ac1ad9`.

[54] D.A. Read, F.S. Hover, and M.S. Triantafyllou. “Forces on oscillating foils for propulsion and maneuvering”. In: *Journal of Fluids and Structures* 17.1 (2003), pp. 163–183. ISSN: 0889-9746. DOI: `https://doi.org/10.1016/S0889-9746(02)00115-9`.

[55] GI. E. Garrick. “PROPULSION OF A FLAPPING AND OSCILLATING AIRFOIL”. In: 567 (1937).

[56] Michael Triantafyllou, George Triantafyllou, and R. Gopalkrishnan. “Wake mechanics for thrust generation in oscillating foils”. In: *Physics of Fluids* (1991).

[57] L. Schouveiler, F.S. Hover, and M.S. Triantafyllou. “Performance of flapping foil propulsion”. In: *Journal of Fluids and Structures* 20.7 (2005). Fluid-Plate Interactions, pp. 949–959. ISSN: 0889-9746. DOI: `https://doi.org/10.1016/j.jfluidstructs.2005.05.009`. URL: `https://www.sciencedirect.com/science/article/pii/S0889974605000770`.

[58] Alexander Matta et al. “Effects of fish caudal fin sweep angle and kinematics on thrust production during low-speed thunniform swimming”. In: *Biology Open* 8.7 (July 2019), bio040626.

[59] Chendur Singaram. *How do Hydrofoils work?* 2022. URL: `https://www.chendurs.com/blogs2/hydrofoils` (visited on 11/12/2025).

[60] Florine Paraz, L. Schouveiler, and Christophe Eloy. “Thrust generation by a heaving flexible foil: Resonance, nonlinearities, and optimality”. In: *Physics of Fluids* 28 (Jan. 2016), p. 011903. DOI: `10.1063/1.4939499`.

[61] Michael Triantafyllou and George Triantafyllou. “An Efficient Swimming Machine”. In: *Scientific American - SCI AMER* 272 (Mar. 1995), pp. 64–70. DOI: `10.1038/scientificamerican0395-64`.

[62] Carl H White, George V Lauder, and Hilary Bart-Smith. “Tunabot Flex: a tuna-inspired robot with body flexibility improves high-performance swimming”. In: *Bioinspiration Biomimetics* 16.2 (Mar. 2021), p. 026019. DOI: `10.1088/1748-3190/abb86d`. URL: `https://dx.doi.org/10.1088/1748-3190/abb86d`.

[63] Robert K. Katzschmann et al. “Exploration of underwater life with an acoustically controlled soft robotic fish”. In: *Science Robotics* 3.16 (2018), eaar3449. DOI: `10.1126/scirobotics.aar3449`. URL: `https://www.science.org/doi/abs/10.1126/scirobotics.aar3449`.

[64] Moise Raphael Tsimbo Fokou et al. “A Soft Robotic Fish Actuated by Artificial Muscle Modules (SoRoFAAM-1)”. In: *Journal of Bionic Engineering* 20.5 (2023), p. 2030. DOI: `10.1007/s42235-023-00390-6`. URL: `http://jbe.jlu.edu.cn/EN/abstract/article_1271.shtml`.

[65] Sander C. van den Berg et al. “OpenFish: Biomimetic design of a soft robotic fish for high speed locomotion”. In: *HardwareX* 12 (2022), e00320. ISSN: 2468-0672. DOI: `https://doi.org/10.1016/j.ohx.2022.e00320`. URL: `https://www.sciencedirect.com/science/article/pii/S2468067222000657`.

[66] World Animal Protection. *Fish facts*. URL: `https://www.worldanimalprotection.ca/education/animal-facts/fish-facts/#:~:text=There%20are%20over%2033%2C000%20different,these%20species%20are%20very%20distinct.` (visited on 11/14/2025).

[67] Thibaut Paschal et al. “Development of bio-inspired underwater robot with adaptive morphology capable of multiple swimming modes”. In: (2017), pp. 4197–4202. DOI: `10.1109/IROS.2017.8206281`.

[68] Junzhi Yu et al. “On a Bio-inspired Amphibious Robot Capable of Multimodal Motion”. In: *IEEE/ASME Transactions on Mechatronics* 17.5 (2012), pp. 847–856. DOI: `10.1109/TMECH.2011.2132732`.

[69] Dominik Fill et al. “Amphibious Bioinspired Robots for Ocean Objects Identification”. In: *AIAA AVIATION 2021 FORUM*. DOI: `10.2514/6.2021-2781`. URL: `https://arc.aiaa.org/doi/abs/10.2514/6.2021-2781`.

[70] David Tan et al. “Trout-like multifunctional piezoelectric robotic fish and energy harvester”. In: *Bioinspiration and Biomimetics* 16.4 (2021). Cited by: 30. DOI: 10.1088/1748-3190/ac011e. URL: https://www.scopus.com/inward/record.uri?eid=2-s2.0-85109115082&doi=10.1088%2f1748-3190%2fac011e&partnerID=40&md5=bfa12ac52cff361be33087d5a1e309dd.

[71] Heidi Dewar and Jeffrey Graham. “Studies of Tropical Tuna Swimming Performance in a Large Water Tunnel: III. Kinematics”. In: *The Journal of experimental biology* 192 (July 1994), pp. 45–59. DOI: 10.1242/jeb.192.1.45.

[72] Wendi Liu, Qing Xiao, and Qiang Zhu. “Passive Flexibility Effect on Oscillating Foil Energy Harvester”. In: *AIAA Journal* 54 (Jan. 2016), pp. 1–16. DOI: 10.2514/1.J054205.

[73] “Effects of free surface on a flapping-foil based ocean current energy extractor”. In: *Renewable Energy* 181 (2022), pp. 933–944. ISSN: 0960-1481. DOI: https://doi.org/10.1016/j.renene.2021.09.098. URL: https://www.sciencedirect.com/science/article/pii/S0960148121014270.

[74] Bradley Simpson, Franz Hover, and Michael Triantafyllou. “Experiments in direct energy extraction through flapping foils”. In: *18th international offshore and polar engineering conference, Canada* (Jan. 2008).

[75] Wendi Liu, Qing Xiao, and Fai Cheng. “A bio-inspired study on tidal energy extraction with flexible flapping wings”. In: *Bioinspiration Biomimetics* 8.3 (Aug. 2013), p. 036011. DOI: 10.1088/1748-3182/8/3/036011. URL: https://dx.doi.org/10.1088/1748-3182/8/3/036011.

[76] Bing Zhu, Junwei Zhang, and Wei Zhang. “Impact of the ground effect on the energy extraction properties of a flapping wing”. In: *Ocean Engineering* 209 (2020), p. 107376. ISSN: 0029-8018. DOI: https://doi.org/10.1016/j.oceaneng.2020.107376. URL: https://www.sciencedirect.com/science/article/pii/S0029801820304066.

[77] Guanghua He et al. “Numerical study of a semi-passive oscillating hydrofoil on power-extraction with wing-in-ground effect”. In: *Journal of Fluids and Structures* 115 (2022), p. 103761. ISSN: 0889-9746. DOI: https://doi.org/10.1016/j.jfluidstructs.2022.103761. URL: https://www.sciencedirect.com/science/article/pii/S0889974622001530.

[78] EDF. *Journey to the heart of energy - How a marine turbine works*. Accessed: 2024-11-26. 2019. URL: https://www.youtube.com/watch?v=fL04rayLiCo.

[79] S Vasiljević et al. “Regenerative braking on electric vehicles: working principles and benefits of application”. In: *IOP Conference Series: Materials Science and Engineering* 1271.1 (Dec. 2022), p. 012025. DOI: 10.1088/1757-899X/1271/1/012025. URL: https://dx.doi.org/10.1088/1757-899X/1271/1/012025.

[80] A. Sathishkumar et al. “Review on Regenerative Braking System”. In: *E-Mobility: A New Era in Automotive Technology*. Ed. by M. Kathiresh, G. R. Kanagachidambaresan, and Sheldon S. Williamson. Cham: Springer International Publishing, 2022, pp. 149–163.

[81] James Graves, Yang Kuang, and Meiling Zhu. “Pendulum energy harvester with torsion spring mechanical energy storage regulator”. In: *Sensors and Actuators A: Physical* 339 (2022), p. 113505. ISSN: 0924-4247. DOI: https://doi.org/10.1016/j.sna.2022.113505. URL: https://www.sciencedirect.com/science/article/pii/S0924424722001431.

[82] X. Yang, C. Wang, and S.K. Lai. “A magnetic levitation-based tristable hybrid energy harvester for scavenging energy from low-frequency structural vibration”. In: *Engineering Structures* 221 (2020), p. 110789. ISSN: 0141-0296. DOI: https://doi.org/10.1016/j.engstruct.2020.110789. URL: https://www.sciencedirect.com/science/article/pii/S0141029620314528.

[83] Yongkuang Zhang et al. “Cable-driven power take-off for WEC-glider: Modeling, simulation, experimental study, and application”. In: *Energy* 282 (2023), p. 128851. ISSN: 0360-5442. DOI: https://doi.org/10.1016/j.energy.2023.128851. URL: https://www.sciencedirect.com/science/article/pii/S0360544223022454.

[84] Saeed Rezaei et al. “Experimental and numerical study of a novel unidirectional mechanical power take-off system for two-body wave energy converters”. In: *Energy Conversion and Management: X* 19 (2023), p. 100385. ISSN: 2590-1745. DOI: https://doi.org/10.1016/j.ecmx.2023.100385. URL: https://www.sciencedirect.com/science/article/pii/S2590174523000417.

[85] Yiping Zhang, Li Xu, and Yi Zhou. “A wave foil with passive angle of attack adjustment for wave energy extraction for ships”. In: *Ocean Engineering* 246 (2022), p. 110627. ISSN: 0029-8018. DOI: `https://doi.org/10.1016/j.oceaneng.2022.110627`. URL: `https://www.sciencedirect.com/science/article/pii/S0029801822000956`.

[86] Benjamin Drew, Andrew Plummer, and Mehmet Sahinkaya. “A review of wave energy converter technology”. In: *Proceedings of The Institution of Mechanical Engineers Part A-journal of Power and Energy - PROC INST MECH ENG A-J POWER* 223 (Dec. 2009), pp. 887–902. DOI: `10.1243/09576509JPE782`.

[87] Pedro Rolo et al. “Self-adaptive rotational electromagnetic energy generation as an alternative to triboelectric and piezoelectric transductions”. In: *Communications Engineering* 3 (July 2024). DOI: `10.1038/s44172-024-00249-6`.

[88] Abdulrahman Jbaily and Ronald Yeung. “Piezoelectric devices for ocean energy: a brief survey”. In: *Journal of Ocean Engineering and Marine Energy* 1 (Feb. 2014), pp. 101–118. DOI: `10.1007/s40722-014-0008-9`.

[89] Li-Jiao Gong, Xing Shen, and Jiang-Quan Li. “Experimental investigation of energy harvesting from triple-layer piezoelectric bender”. In: 2009. DOI: `10.1109/ISAF.2009.5307542`. URL: `https://www.scopus.com/inward/record.uri?eid=2-s2.0-74349121872&doi=10.1109%5C%2fISAF.2009.5307542&partnerID=40&md5=1f8f8270144e20a726b472d5fd70e0af`.

[90] Shashank Pri 0ya and Daniel Inman. *Energy Harvesting Technologies*. Jan. 2009. ISBN: 978-0-387-76463-4. DOI: `10.1007/978-0-387-76464-1`.

[91] Smart Material Corp. *MFC V2.4 Datasheet*. `https://smart-material.com/wp-content/uploads/2025/02/MFC_V2.4-datasheet-web.pdf`. Accessed: 14 Nov 2025.

[92] Shashi Bahl et al. “Smart materials types, properties and applications: A review”. In: *Materials Today: Proceedings* 28 (2020). International Conference on Aspects of Materials Science and Engineering, pp. 1302–1306. ISSN: 2214-7853. DOI: `https://doi.org/10.1016/j.matpr.2020.04.505`. URL: `https://www.sciencedirect.com/science/article/pii/S2214785320331278`.

[93] Ibrahim Qader et al. “A Review of Smart Materials Researches and Applications”. In: *El-Cezeri Fen ve Mühendislik Dergisi* 6 (Sept. 2019), pp. 755–788. DOI: `10.31202/ecjse.562177`.

[94] Bo-Hua Sun. *Smart Materials and Structures*. Sept. 2015.

[95] Zhangxian Deng and Marcelo J. Dapino. “Review of magnetostrictive materials for structural vibration control”. In: *Smart Materials and Structures* 27 (2018). URL: `https://api.semanticscholar.org/CorpusID:139182196`.

[96] Ruiqian Wang et al. “Soft Underwater Swimming Robots Based on Artificial Muscle”. In: *Advanced Materials Technologies* 8 (Oct. 2022). DOI: `10.1002/admt.202200962`.

[97] Rabiu A Abubakar and Huyutian. “The feasibility design and modeling for thermo-mechanical ocean energy harvester using shape memory alloys”. In: *Journal of Physics: Conference Series* 1074.1 (Sept. 2018), p. 012065. DOI: `10.1088/1742-6596/1074/1/012065`. URL: `https://dx.doi.org/10.1088/1742-6596/1074/1/012065`.

[98] NASA. *NASA’s Shape Memory Materials Open Doors for Smart Tech*. Accessed: 2025-02-11. URL: `https://technology.nasa.gov/Shape%5C%20Memory%5C%20Materials%5C%20Open%5C%20Doors%5C%20for%5C%20Smart%5C%20Tech`.

[99] Jaronie Mohd Jani et al. “A review of shape memory alloy research, applications and opportunities”. In: *Materials Design (1980-2015)* 56 (2014), pp. 1078–1113. ISSN: 0261-3069. DOI: `https://doi.org/10.1016/j.matdes.2013.11.084`. URL: `https://www.sciencedirect.com/science/article/pii/S0261306913011345`.

[100] BALLUFF. *Magnetostrictive sensors*. Accessed: 2025-03-27. URL: `https://www.balluff.com/en-nl/products/areas/A0001/groups/G0116`.

[101] TdVibb. *CU18A Ultrasonic Actuator*. Accessed: 2025-03-27. URL: `http://tdvib.com/cu18a-ultrasonic-actuator/`.

[102] TdVibb. *Terfenol-D*. Accessed: 2025-03-27. URL: `http://tdvib.com/terfenol-d/`.

[103] Conrad. *electromagneet*. Accessed: 2025-03-27. URL: https://www.conrad.nl/nl/search.html?search=electromagneet.

[104] Exonetik. *Technology*. Accessed: 2025-03-27. URL: https://www.exonetik.com/technology.

[105] Allegro microsystems. *New High-Bandwidth Current Sensors Incorporating XtremeSense™ TMR Technology*. Accessed: 2025-03-27. URL: https://www.allegromicro.com/en/products/emerging-technologies/tmr?utm_source=google&utm_medium=cpc&utm_campaign=allegro+tmr+hsm&utm_term=&utm_campaign=TMR_pMAX_Google_2024&utm_source=adwords&utm_medium=ppc&hsa_acc=6276172133&hsa_cam=22318288009&hsa_grp=&hsa_ad=&hsa_src=x&hsa_tgt=&hsa_kw=&hsa_mt=&hsa_net=adwords&hsa_ver=3&gad_source=1&gclid=CjwKCAjw7pO_BhAlEiwA4pMQvBXt8D_aLU7UXHI-Ds1dEKX4H5XaqWSj0dE4ZESGJ8EeDD72RtuHJRoCX-MQAvD_BwE.

[106] Jiaqi Xu et al. “Flexible, self-powered, magnetism/pressure dual-mode sensor based on magnetorheological plastomer”. In: *Composites Science and Technology* 183 (2019), p. 107820. ISSN: 0266-3538. DOI: https://doi.org/10.1016/j.compscitech.2019.107820. URL: https://www.sciencedirect.com/science/article/pii/S0266353819314940.

[107] Xu Jin et al. “Bio-inspired soft actuator with contact feedback based on photothermal effect and triboelectric nanogenerator”. In: *Nano Energy* 99 (2022), p. 107366. ISSN: 2211-2855. DOI: https://doi.org/10.1016/j.nanoen.2022.107366. URL: https://www.sciencedirect.com/science/article/pii/S221128552200444X.

[108] Xingzhao Wang et al. “A flexible triboelectric-piezoelectric hybrid nanogenerator based on P(VDF-TrFE) nanofibers and PDMS/MWCNT for wearable devices”. In: *Scientific Reports* 6 (Nov. 2016), p. 36409. DOI: 10.1038/srep36409.

[109] Syed Nasimul Alam et al. “An introduction to triboelectric nanogenerators”. In: *Nano-Structures Nano-Objects* 34 (2023), p. 100980. ISSN: 2352-507X. DOI: https://doi.org/10.1016/j.nanoso.2023.100980. URL: https://www.sciencedirect.com/science/article/pii/S2352507X23000434.

[110] “Potentials of magnetic shape memory alloys for energy harvesting”. In: *Journal of Magnetism and Magnetic Materials* 537 (2021), p. 168112. ISSN: 0304-8853. DOI: https://doi.org/10.1016/j.jmmm.2021.168112.

[111] Heung Soo Kim, Joo-Hyong Kim, and Jaehwan Kim. “A Review of Piezoelectric Energy Harvesting Based on Vibration”. In: *International Journal of Precision Engineering and Manufacturing* 12 (Dec. 2011). DOI: 10.1007/s12541-011-0151-3.

[112] Huidong Li, Chuan Tian, and Z. Daniel Deng. “Energy harvesting from low frequency applications using piezoelectric materials”. In: *Applied Physics Reviews* 1.4 (2014). DOI: 10.1063/1.4900845. URL: https://www.scopus.com/inward/record.uri?eid=2-s2.0-84920282289&doi=10.1063%5C%2f1.4900845&partnerID=40&md5=e0ab60bac4b1bc262dbb5d72fa3299ea.

[113] G.W. Taylor et al. “The Energy Harvesting Eel: a small subsurface ocean/river power generator”. In: *IEEE Journal of Oceanic Engineering* 26.4 (2001), pp. 539–547. DOI: 10.1109/48.972090.

[114] Xiaotong Gao, Wei-Heng Shih, and Wan Y. Shih. “Flow Energy Harvesting Using Piezoelectric Cantilevers With Cylindrical Extension”. In: *IEEE Transactions on Industrial Electronics* 60.3 (2013), pp. 1116–1118. DOI: 10.1109/TIE.2012.2187413.

[115] Huicong Liu et al. “A new S-shaped MEMS PZT cantilever for energy harvesting from low frequency vibrations below 30 Hz”. In: *Microsystem Technologies* 18.4 (Apr. 2012), pp. 497–506. DOI: 10.1007/s00542-012-1424-1.

[116] Yonggang Jiang et al. “Low-Frequency Energy Harvesting Using a Laminated PVDF Cantilever with a Magnetic Mas”. In: *Power MEMS* 2010 (Nov. 2009).

[117] Shanshan Li et al. “Bi-resonant structure with piezoelectric PVDF films for energy harvesting from random vibration sources at low frequency”. In: *Sensors and Actuators A: Physical* 247 (2016), pp. 547–554. ISSN: 0924-4247. DOI: https://doi.org/10.1016/j.sna.2016.06.033. URL: https://www.sciencedirect.com/science/article/pii/S0924424716303211.

[118] Delft University of Technology. *Delft Design Guide*. PDF. Accessed: 2025-11-15. 2019. URL: https://arl.human.cornell.edu/PAGES_Delft/Delft_Design_Guide.pdf.

[119] Rik van der Wardt. *Double Diamond Model (nieuwe versie): uitleg bij de 4 fases*. URL: https://designthinkingworkshop.nl/double-diamond/ (visited on 11/12/2025).

[120] Jan Herrington et al. “Design-based research and doctoral students: Guidelines for preparing a dissertation proposal”. English. In: *Proceedings of World Conference on Educational Multimedia, Hypermedia and Telecommunications 2007*. Ed. by C. Montgomerie and J. Seale. World Conference on Educational Multimedia, Hypermedia & Telecommunications 2007, ED-MEDIA 2007 ; Conference date: 25-06-2007 Through 27-06-2007. June 2007, pp. 4089–4097.

[121] B. Gaurier et al. “Tidal Energy ”Round Robin” Tests Comparisons between towing tank and circulating tank results”. In: *International Journal of Marine Energy* 12 (June 2015). DOI: 10.1016/j.ijome.2015.05.005.

[122] PolyK. *Piezoelectric PVDF Flexible Elongation Sensor With Leads 10 mm x 50 mm*. 2025. URL: https://piezopvdf.com/piezoelectric-pvdf-flexible-elongation-sensor-with-leads-10-mm-x-50-mm/ (visited on 10/17/2025).

[123] Piezodrive. *Actuators*. 2025. URL: https://www.piezodrive.com/actuators/ (visited on 10/22/2025).

[124] Piezo Direct. *Custom piezo components*. 2025. URL: https://piezodirect.com/?utm_source=google&utm_medium=cpc&utm_campaign=1599272779&utm_content=85751291205&utm_term=piezo%20components&gad_source=1&gad_campaignid=1599272779&gbraid=0AAAAAC-U_5tNTXY9eUMY2m39owpgz24RB&gclid=CjwKCAjwx-zHBhBhEiwA7Kjq6-Dh9dzartJvacGpcrZvsM7f3vejKmLzRidID3GhRkqWs4PXhop3ABoC7NgQAvD_BwE (visited on 10/22/2025).

[125] testo. *testo 410i - Bluetooth vleugelrad anemometer met App*. 2025. URL: https://www.testo.com/nl-NL/testo-410i/p/0560-1410 (visited on 10/14/2025).

[126] Technical University Delft faculty ME. *TU Delft opent wereldwijd unieke windtunnel*. 2025. URL: https://www.tudelft.nl/2022/3me/nieuws/tu-delft-opent-wereldwijd-unieke-windtunnel (visited on 10/14/2025).

[127] Ali Bakhshandeh Rostami, Mohammad Mobasher Amini, and Antonio Fernandes. “Strouhal number of flat and flapped plates at moderate Reynolds number and different angles of attack: experimental data”. In: *Acta Mechanica* (Jan. 2019). DOI: 10.1007/s00707-018-2292-2.

[128] Jerry M. Chen and Yuan-Cheng Fang. “Strouhal numbers of inclined flat plates”. In: *Journal of Wind Engineering and Industrial Aerodynamics* 61.2 (1996), pp. 99–112. ISSN: 0167-6105. DOI: https://doi.org/10.1016/0167-6105(96)00044-X. URL: https://www.sciencedirect.com/science/article/pii/016761059600044X.

[129] Teledyne Valeport. *Model 001 Flowmeter*. 2025. URL: https://www.valeport.co.uk/products/model-001-flowmeter/ (visited on 10/18/2025).

[130] Ansys Optics. *Using Parseval’s theorem to check for energy conservation between the time and frequency domain*. Accessed: 2025-11-15. n.d. URL: https://optics.ansys.com/hc/en-us/articles/360034394274-Using-Parseval-s-theorem-to-check-for-energy-conservation-between-the-time-and-frequency-domain.

[131] *Understanding FFTs and Windowing*. Tech. rep. Accessed: 2025-11-21. National Instruments, 2011. URL: https://download.ni.com/evaluation/pxi/Understanding%20FFTs%20and%20Windowing.pdf.

[132] Stephanie Burrell. *Understanding the Hanning Window: A Practical Guide for Beginners*. Accessed: 2025□11□20. 2024. URL: https://wraycastle.com/blogs/knowledge-base/hanning-window?srsltid=AfmBOoqpDEqIt7SOZRYEb_weFgIm8uniRMd5Q5jdMMl2Uw8BWyiE38sZ.

[133] NumPy Developers. *numpy.hanning — NumPy v1.x Manual*. https://numpy.org/devdocs/reference/generated/numpy.hanning.html. Accessed: 2025□11□20.

[134] Siemens Digital Industries Software Community. *Window Correction Factors*. Accessed: 2025□11□20. n.d. URL: https://community.sw.siemens.com/s/article/window-correction-factors.

[135] University of Pennsylvania Department of Neurobiology. *Capacitor Current and Membrane Currents – Membrane Properties*. Accessed: 2025□11□20. n.d. URL: https://www.sas.upenn.edu/LabManuals/BBB251/NIA/NEUROLAB/APPENDIX/MEMBRANE/capcurr.htm.

[136] KERN. *Schoolweegschaal EMB 2200-0*. 2025. URL: `https://www.kern-sohn.com/shop/nl/producten/laboratoriumweegschalen/schoolweegschaal/EMB-2200-0/` (visited on 10/22/2025).

[137] PiezoDrive. *BD300 300 V Dual Channel Amplifier*. Accessed: 2025-11-20. n.d. URL: `https://www.piezodrive.com/product/bd300-300v-dual-channel-amplifier/?srsltid=AfmBOoqAp8zrJJURpyhe8jE4J762Xos7bbf1FPYT_QgmYRJSdxfl49Pb`.

[138] Engineering Infinity. *Beam Deflection – Slope Formulas*. URL: `https://engineeringinfinity.com/beam-deflection-slope-formulas/` (visited on 11/12/2025).

[139] Brüning онлайн. *Schakelingen 1 – Applets voor E‑techniek*. Accessed: 2025‑11‑20. n.d. URL: `https://bruningonline.nl/applets/schakelingen1/schakelingen1.htm`.

[140] Omni Calculator. *Battery charge time calculator – Everyday life*. Accessed: 2025‑11‑20. n.d. URL: `https://www.omnicalculator.com/everyday-life/battery-charge-time`.

A

Test setup

Figure A.1 gives the specific dimensions of the base of the test setup. The angles are necessary to determine the flapping amplitude of the tail. The small slit fits the strut (Figure A.2

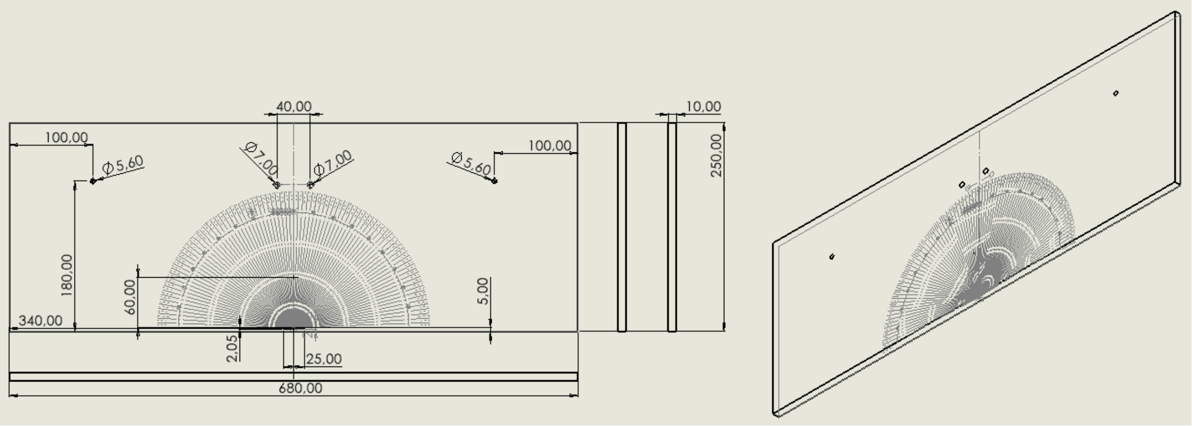

Figure A.1: Test setup base with angles. *Wood/PMMA*

Figure A.2 shows the specific dimensions of the strut used in all test cases. The holes correspond to the holes in the base (Figure 3.8). The holes on the T ends correspond to the holes in the support brackets (Figure A.3).

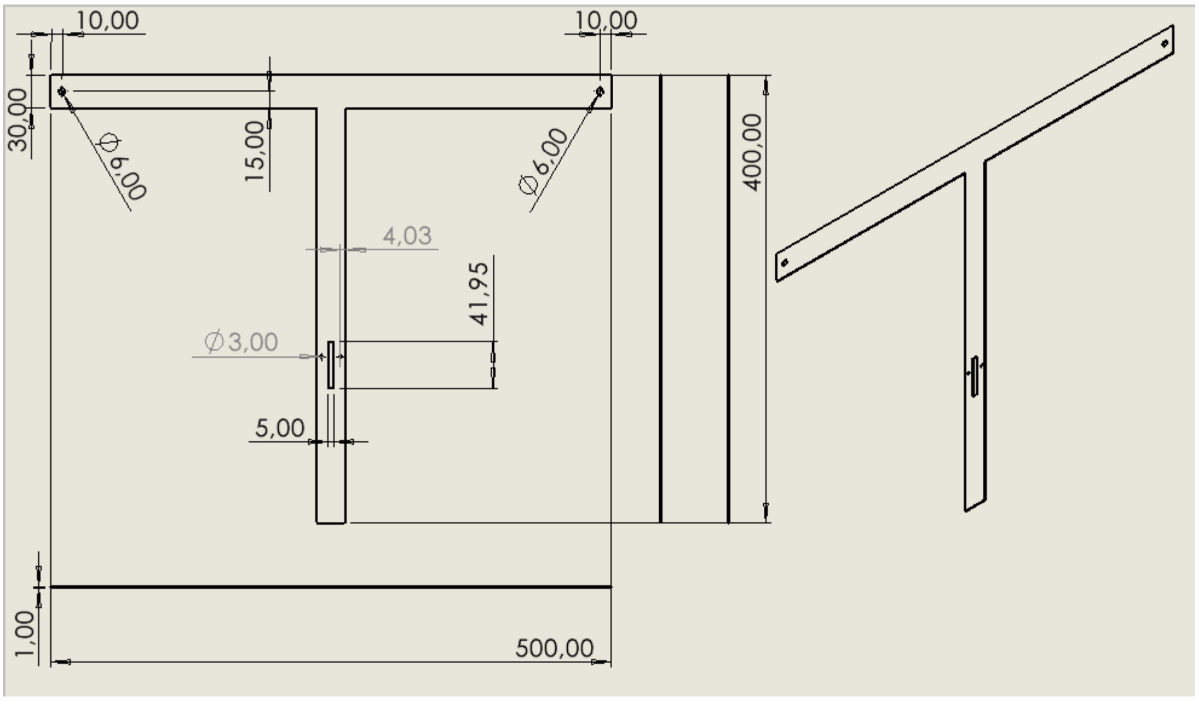

Figure A.2: Test setup strut. *Steel*

Figure A.3 shows the specific dimensions of the support brackets of the test setup. The function of the support brackets is to keep the strut and the base in place and to support the strut when subjected to flow.

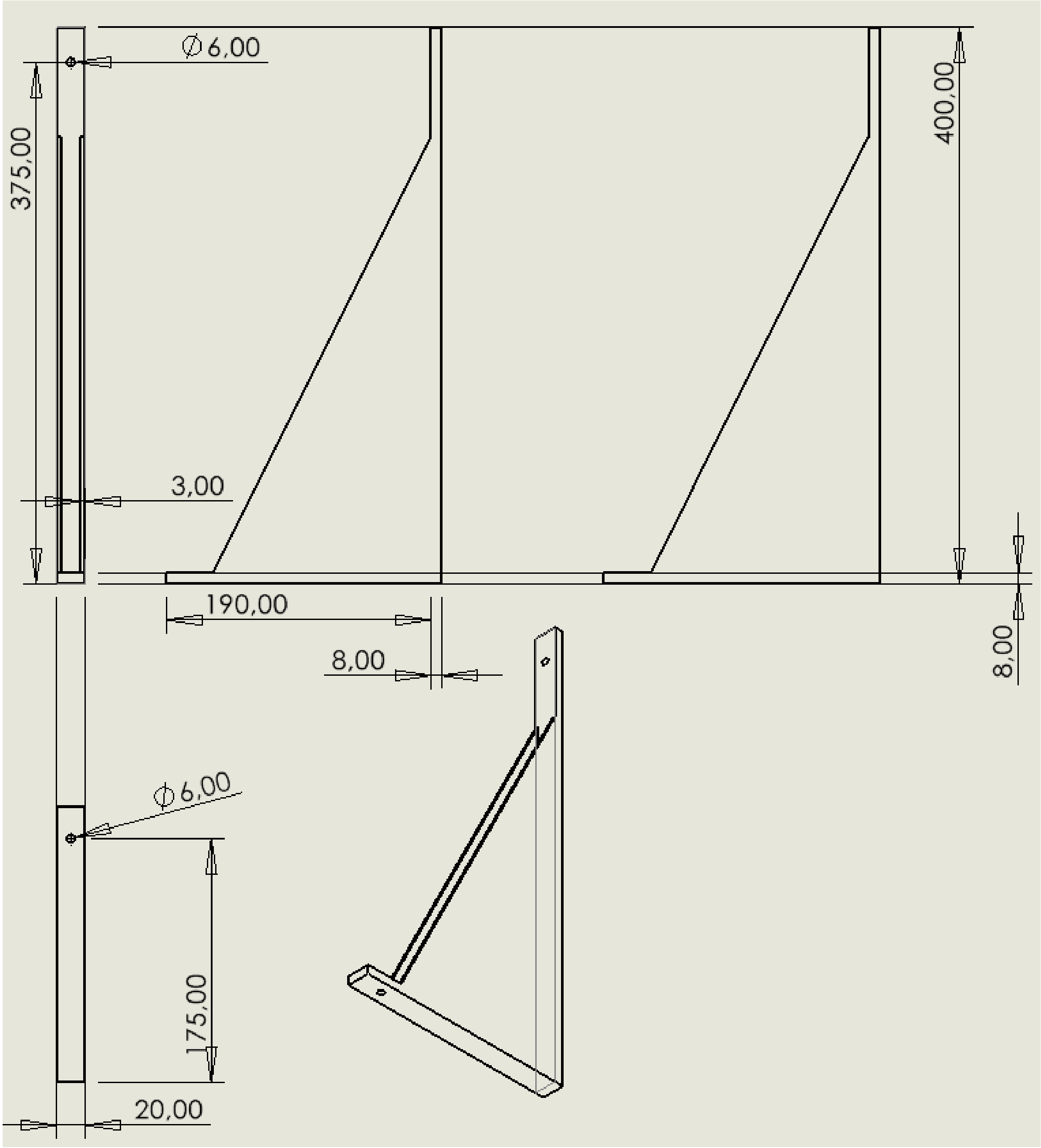

Figure A.3: Test setup brackets. *Steel*